



저작자표시-비영리-변경금지 2.0 대한민국

이용자는 아래의 조건을 따르는 경우에 한하여 자유롭게

- 이 저작물을 복제, 배포, 전송, 전시, 공연 및 방송할 수 있습니다.

다음과 같은 조건을 따라야 합니다:



저작자표시. 귀하는 원저작자를 표시하여야 합니다.



비영리. 귀하는 이 저작물을 영리 목적으로 이용할 수 없습니다.



변경금지. 귀하는 이 저작물을 개작, 변형 또는 가공할 수 없습니다.

- 귀하는, 이 저작물의 재이용이나 배포의 경우, 이 저작물에 적용된 이용허락조건을 명확하게 나타내어야 합니다.
- 저작권자로부터 별도의 허가를 받으면 이러한 조건들은 적용되지 않습니다.

저작권법에 따른 이용자의 권리는 위의 내용에 의하여 영향을 받지 않습니다.

이것은 [이용허락규약\(Legal Code\)](#)을 이해하기 쉽게 요약한 것입니다.

[Disclaimer](#)

이학박사 학위논문

**Dielectric properties on alloy of
BaHfO₃ and BaTiO₃**

BaHfO₃와 BaTiO₃ 혼합산화물의 유전특성에 대한
연구

2023 년 8 월

서울대학교 대학원

물리천문학부

송도원

Dielectric properties on alloy of BaHfO_3 and BaTiO_3

지도 교수 차 국 린

이 논문을 이학박사 학위논문으로 제출함

2023 년 7 월

서울대학교 대학원

물리천문학부

송 도 원

송도원의 이학박사 학위논문을 인준함

2023 년 7 월

위 원 장 _____ 홍승훈 (인)

부위원장 _____ 차국린 (인)

위 원 _____ 유재준 (인)

위 원 _____ 김기훈 (인)

위 원 _____ 이기영 (인)

Abstract

Dielectric properties on alloy of BaHfO_3 and BaTiO_3

Dowon Song

Department of Physics and Astronomy
The Graduate School
Seoul National University

Si-based device technology has undergone significant reduction in size over the past few decades, with the aim of lowering thermal heating and power consumption. In order to decrease power consumption and thermal heating, it is necessary to reduce the operating voltage, which can be achieved by increasing capacitance. However, this leads to a thinner gate oxide as the device size shrinks, resulting in increased leakage current via direct tunneling, thus limiting device performance. To address these limitations, researchers have explored high-k materials that can provide the required capacitance with a thicker gate oxide. High-k dielectrics must possess high dielectric constant and high dielectric strength under high electric field to be considered suitable for use as gate dielectric materials in Si-based devices.

This dissertation focuses on the study of an alloy system of BaHfO_3 and BaTiO_3 (Epitaxial $\text{BaHf}_{1-x}\text{Ti}_x\text{O}_3$ (BHTO) system) to investigate the dielectric characteristics of the system as a high-k gate oxide. Varying the Ti ratio x from 0.2 to 0.8, we measured their dielectric constants, breakdown fields and the leakage currents by using the $\text{Ba}_{0.96}\text{La}_{0.04}\text{SnO}_3$ as the epitaxial electrodes. As the ratio of Ti

increases, the dielectric constant undergoes a corresponding rise. The breakdown field stayed larger than 5 MV/cm as long as x does not exceed 0.4 and the leakage current remained low in the range of $10^{-7}\sim 10^{-3}$ A/cm² below the breakdown field. The results suggest that a maximum 2-dimensional carrier density of $n_{2D} = 2\times 10^{14}$ cm⁻² could be modulated by the BaHf_{0.6}Ti_{0.4}O₃ dielectric. An all-perovskite transparent field effect transistor operating in an n-type accumulation mode was fabricated, using epitaxial BaHf_{0.6}Ti_{0.4}O₃ as the gate insulator. The device exhibited I_{on}/I_{off} ratio higher than 10^7 , V_{GS} smaller than 6 V for maximum mobility, and a subthreshold swing value of 0.2 V dec⁻¹.

For the BaHf_{0.6}Ti_{0.4}O₃(BHTO) case, changed fabrication process resulted enhanced dielectric properties. It was discovered that the dielectric constant, breakdown field, and leakage current have values of 150, 5.0 MV/cm, and 10^{-4} A/cm² at 2 MV/cm, respectively. These results suggest that the BHTO gate oxide could modulate a 2D carrier density greater than $n_{2D} = 10^{14}$ cm⁻². Typically, there exists a trade-off between the dielectric constant and breakdown field, making it difficult to modulate the two-dimensional carrier concentration of $n_{2D} = 10^{14}$ cm⁻² using traditional solid-state dielectrics. An n-type accumulation mode FET and n-type depletion-mode FET were demonstrated, which directly suppressed more than $n_{2D} = 10^{14}$ cm⁻². The large dielectric constant, high breakdown field and low leakage current of BHTO are attributed to the nanometer scale stoichiometric modulation of hafnium and titanium. Based on this model, the presence of hafnium as a background material inhibits the formation of percolation paths, resulting in a decrease in the leakage current.

However, the dielectric constant of BHTO decreases as the thickness decreases, which is well known problem in high-k dielectric as “size effect”. This problem

manifests itself as the unwanted small interfacial capacitance. Although the origin of the size effect remains quite controversial, strong epitaxial bonding is thought to be the crucial factor determining the size effect. Strong interfacial bonding between high-k dielectric and the electrode promotes propagation of the soft phonons responsible for the high-k to the electrode, resulting in suppression of the soft phonons and the high-k at the interface. In order to create a boundary for such propagation, intentionally mismatched lattice between the dielectric and the electrode was employed, using SrRuO₃ as the bottom electrode and ITO as top electrode to weaken the interfacial epitaxial bonding. We find the interfacial capacitance value to increase by a factor of 3~5.

To further develop a high-k material, SrHfO₃ was investigated. The leakage current of SrHfO₃ (SHO) is extremely low ($<10^{-8}$ A/cm² at 2 MV/cm). The origin of exceptionally low leakage current of SHO is attributed to the large bandgap (~6 eV) and large conduction band offset (~3.3 eV) between 4% BLSO and SHO. This large conduction band offset is comparable to that of between Si and SiO₂. Hence, the electron affinity of SHO is sufficiently low (~1.2 eV) to establish a significant conduction band offset (>1 eV) with most electrode materials. Nevertheless, the dielectric constant of SHO is relatively modest (~30). Consequently, there is potential for further advancements by integrating SHO with other materials such as SrTiO₃ and BaTiO₃, employing a similar approach as in the case of BHTO.

Keywords: BaHfO₃, BaTiO₃, Perovskite oxide, High-k, stoichiometric modulation, size effect, interfacial phonon engineering. SrHfO₃

Student Number: 2017-23010

List of Contents

Abstract	i
List of Contents	iv
List of Figures and Tables	vi
1. Introduction	1
1.1. Needs for high-k	1
1.2. History of high-k	1
1.3. Comparison of high-k dielectrics	3
References	5
2. Properties of BaHf_{1-x}Ti_xO₃ (BHTO)	7
2.1. Research background	7
2.2. Dielectric properties of BaHf _{1-x} Ti _x O ₃ (BHTO) system	7
2.3. Structural properties of BaHf _{1-x} Ti _x O ₃ (BHTO) system	12
2.4. Optical properties of BaHf _{1-x} Ti _x O ₃ (BHTO) system	13
2.5. Field effect transistors using BaHf _{0.6} Ti _{0.4} O ₃	14
2.6. Conclusion	16
References	17
3. Properties of BaHf_{0.6}Ti_{0.4}O₃	18
3.1. Research background	18
3.2. Dielectric properties of BaHf _{0.6} Ti _{0.4} O ₃	18
3.3. Field effect transistors using BaHf _{0.6} Ti _{0.4} O ₃ for modulation beyond 10 ¹⁴ cm ⁻²	27
3.4. Structural properties of BaHf _{0.6} Ti _{0.4} O ₃	35
3.4.1 Scanning Transmission Electron Microscope (STEM) of BaHf _{0.6} Ti _{0.4} O ₃	35
3.4.2 High-resolution X-ray diffraction (HRXRD) of BaHf _{0.6} Ti _{0.4} O ₃	38
3.5. Optical bandgap of BaHf _{0.6} Ti _{0.4} O ₃	40
3.6. Percolation path formation model	41

3.7. Conclusion	42
References	44
4. Size effect of BaHf_{0.6}Ti_{0.4}O₃	45
4.1. Research background	45
4.2. Origins of size effect	46
4.3. Soft phonon propagation	48
4.4. Thickness dependence of dielectric constant of BHTO	50
4.5. Effect of top ITO electrode on interfacial capacitance	53
4.6. Effect of bottom SrRuO ₃ electrode on interfacial capacitance	55
4.7. Conclusion	58
References	59
5. Properties of SrHfO₃	61
5.1. Research background	61
5.2. Dielectric properties of SrHfO ₃	63
5.3. Field-effect transistor using SrHfO ₃ dielectric	70
5.4. Structural properties of SrHfO ₃	73
5.5. Future work	84
5.6. Conclusion	85
References	86
List of publications and presentations	90
Abstract in Korean	91

List of Figures

Chapter 2.

Figure 2.1 Dielectric constants of $\text{BaHf}_{1-x}\text{Ti}_x\text{O}_3$ system (a) $\text{BaHf}_{0.8}\text{Ti}_{0.2}\text{O}_3$ (b) $\text{BaHf}_{0.6}\text{Ti}_{0.4}\text{O}_3$ (c) $\text{BaHf}_{0.4}\text{Ti}_{0.6}\text{O}_3$ (d) $\text{BaHf}_{0.2}\text{Ti}_{0.8}\text{O}_3$.

Figure 2.2 Breakdown field of $\text{BaHf}_{1-x}\text{Ti}_x\text{O}_3$ system (a) $\text{BaHf}_{0.8}\text{Ti}_{0.2}\text{O}_3$ (b) $\text{BaHf}_{0.6}\text{Ti}_{0.4}\text{O}_3$ (c) $\text{BaHf}_{0.4}\text{Ti}_{0.6}\text{O}_3$ (d) $\text{BaHf}_{0.2}\text{Ti}_{0.8}\text{O}_3$.

Figure 2.3 Dielectric constants and breakdown fields of BHTO, 2-dimensional carrier density which BHTO can modulate with various alloying ratios.

Figure 2.4 Calculation of dielectric constants of BHTO as a function of the alloying ratio calculated by effective medium theory.

Figure 2.5 Statistical measurement data of (a) dielectric constant and (b) breakdown field of $\text{BaHf}_{0.6}\text{Ti}_{0.4}\text{O}_3$.

Figure 2.6 RSM of BHTO with various alloying ratios on BLSO (a) $\text{BaHf}_{0.8}\text{Ti}_{0.2}\text{O}_3$ (b) $\text{BaHf}_{0.6}\text{Ti}_{0.4}\text{O}_3$ (c) $\text{BaHf}_{0.4}\text{Ti}_{0.6}\text{O}_3$ (d) $\text{BaHf}_{0.2}\text{Ti}_{0.8}\text{O}_3$.

Figure 2.7 Lattice constant derived from RSM of BHTO with various alloying ratios on BLSO.

Figure 2.8 The optical bandgap of BHTO. (a) $\text{BaHf}_{0.8}\text{Ti}_{0.2}\text{O}_3$ (b) $\text{BaHf}_{0.6}\text{Ti}_{0.4}\text{O}_3$ (c) $\text{BaHf}_{0.4}\text{Ti}_{0.6}\text{O}_3$ (d) $\text{BaHf}_{0.2}\text{Ti}_{0.8}\text{O}_3$.

Figure 2.9 FET made with 0.3% BLSO channel layer and $\text{BaHf}_{0.6}\text{Ti}_{0.4}\text{O}_3$ gate oxide. (a) schematic of the device. (b) The top view of the device pictured by an optical microscope. (c) The output characteristic of the device. (d) Transfer characteristics of the device.

Chapter 3.

Figure 3.1 X-ray diffraction measurement of BHTO capacitor and Kiessig fringes of BHTO peak. (a), (b), (c) X-ray diffraction data of BHTO MIM capacitor and Kiessig fringes of BHTO peak. (d) Linear scale plot of Kiessig fringes of BHTO peak. (e) Baseline of the curve. (f) Subtraction of baseline, smoothing function for finding Kiessig fringe peaks.

Figure 3.2 Dielectric properties of BHTO. (a) Frequency-dependent capacitance curve of a $\text{BaHf}_{0.6}\text{Ti}_{0.4}\text{O}_3$ metal-insulator-metal device. The inset shows the layer structure of the device. STO, SrTiO_3 . (b) Leakage current density as a function of electric field of the $\text{BaHf}_{0.6}\text{Ti}_{0.4}\text{O}_3$ device in (a). (c) Electric field dependence of dielectric constant measured at 1 kHz with an AC bias of 30 mV.

Figure 3.3 Fowler-Nordheim analysis and comparison of band diagrams. (a) J-E characteristic of BHTO capacitor. (b) $\ln(J E^{-2})$ vs E^{-1} curve for Fowler-Nordheim analysis of leakage current using the following relation, $J \propto E^2 \exp\left(-\frac{4\sqrt{2m_{\text{BHTO}}^*}\Phi^{\frac{3}{2}}}{3ehE}\right)$. The uncertainty in the effective mass of BHTO generates the range of the barrier height from 1.0 eV ($m^* \sim 0.6 m_e$) to 0.5 eV ($m^* \sim 6.0 m_e$). Adding the Fermi level of 0.4 eV above the conduction band minimum, the band offset between the BSO and BHTO is in the range of 0.9~1.4 eV. (c) Comparison of band diagram for Si, BSO, BHTO.

Figure 3.4 Statistical measurement data of 21 MIM devices. (a) Dielectric constant. (b) Breakdown field of $\text{BaHf}_{0.6}\text{Ti}_{0.4}\text{O}_3$. The symbol \pm denotes standard deviations.

Figure 3.5 I-V characteristics of several $\text{BaHf}_{0.6}\text{Ti}_{0.4}\text{O}_3$ capacitors. The current measurement in (b) is limited by the compliance current, and the E_{BD} is located between 5.11 MV cm^{-1} and 6 MV cm^{-1} . Every measurement is performed for voltage sweep mode.

Figure 3.6 Comparison of dielectric constant, breakdown field of dielectric materials including well-known high-k materials. Each colored lines denotes maximum field-induced charge densities. Black dashed lines and gray dashed-dotted lines are theoretical and experimental McPherson dielectric constant–breakdown field relations, respectively.

Figure 3.7 FET in an n-type accumulation mode made with 0.1% BLSO channel layer and $\text{BaHf}_{0.6}\text{Ti}_{0.4}\text{O}_3$ gate oxide. (a) Schematic of the device. (b) The top view of the device pictured by an optical microscope. Gray dotted lines are plotted to illustrate each deposited layer. The channel width (W_{ch}) of 0.1% La-doped BaSnO_3 is $140 \mu\text{m}$, and the channel length (L_{ch}) is $60 \mu\text{m}$. (c) The output characteristic of the device. (d) Transfer characteristics of the device. Source-drain current is plotted in a full green line, leakage current is plotted in a dashed green line. Calculated field-effect mobility is shown in blue circle scatter plot. Black dashed line shows

maximum subthreshold swing (SS) of the device.

Figure 3.8 Detailed geometry for the channel length and width and the gate length for the accumulation mode FET.

Figure 3.9 $\sqrt{I_D}$ vs V_{GS} plot in linear scale for determining threshold voltage (V_T) of device.

Figure 3.10 Thickness profile of 0.4% BLSO channel by AFM measurement.

Figure 3.11 Hall measurement of a 20 nm thick 0.4% La-doped BSO film. (A) Schematic of the film. (B) Geometry of 4-probe Hall measurement. (C) Hall resistance of both diagonals. Hall resistance and voltage was determined by averaging both diagonals with magnetic field of ± 5.34 kG. 2-dimensional carrier concentration was calculated by following equation.

$n_{2D} = \frac{IB}{eV_H} = \frac{B}{eR_H}$ (I: current, B: magnetic field, e: charge of electron, V_H : Hall voltage, R_H : Hall resistance)

$$R_H = \frac{R_{24+} - R_{24-} + R_{31+} - R_{31-}}{4} = 4.74 \Omega,$$

$$n_{2D} = \frac{0.534 T}{1.6 \times 10^{-19} C \times 4.74 \Omega} = 7.03 \times 10^{17} m^{-2} = 7.03 \times 10^{13} cm^{-2}.$$

Growth rate of 0.4% BLSO was determined by measuring the thickness of 7000 laser shots deposited film as 156 nm. The 20 nm thick film used for Hall measurement was deposited by 897 laser shots.

The corresponding mobility value calculated from the sheet resistance 3,036 of the film is 29.23 $cm^2/V \cdot s$.

Figure 3.12 FET in an n-type depletion mode made with 0.4 % La-doped BSO channel layer and $Hf_{0.6}Ti_{0.4}O_3$ gate oxide. (a) Schematic of the device. (b) The top view of the device pictured by an optical microscope. Gray dotted lines are plotted to illustrate each deposited layer. The channel width (W_{ch}) of 0.4% La-doped $BaSnO_3$ is 140 μm , and the average channel length (L_{ch}) is 130 μm . (c) The output characteristic of the device. (d) Transfer characteristics of the device. Source-drain current is plotted in a full green line, leakage current is plotted in a dashed green line. Calculated field-effect mobility is shown in blue circle scatter plot.

Figure 3.13 Detailed geometry for the channel width and length and the gate length of the depletion mode FET.

Figure 3.14 Capacitance of a BHTO depletion mode FET with 0.4% BLSO channel (A) Capacitance-frequency curve of depletion mode FET with zero dc bias and 30 mV ac bias. (B) C-V curve of depletion mode FET. Using the average capacitance of 51 pF over the gate bias range (-38 to 0 V), the calculated 2D density is $1.07 \times 10^{14} \text{ cm}^{-2}$, taking into account the area of $140 \text{ } \mu\text{m} \times 80 \text{ } \mu\text{m}$. The DC bias during the C-V measurement was stopped at -30 V due to the limit by the measurement equipment (Keithley 4200).

Figure 3.15 STEM image of $\text{BaHf}_{0.6}\text{Ti}_{0.4}\text{O}_3$. (a) HAADF-STEM of various magnification scales. (b) LAADF-STEM of various magnification scales.

Figure 3.16 EELS of BHTO. (a) EELS element mapping image of $\text{BaHf}_{0.6}\text{Ti}_{0.4}\text{O}_3$. (b) Region of EELS line scan. Red arrows denote scan directions. (c) Line profile of Ti and Hf elements.

Figure 3.17 RSM of BHTO. (a) Reciprocal space mapping (RSM) of $\text{BaHf}_{0.6}\text{Ti}_{0.4}\text{O}_3$ (103) peak. (b) (002) peaks and corresponding rocking curves. Black dotted lines are rocking curve scan regions. Detailed rocking curves and full width half maximums (FWHM) are presented in Figure 3.18.

Figure 3.18 Rocking curves of $\text{BaHf}_{0.6}\text{Ti}_{0.4}\text{O}_3$ capacitor from XRD measurements.

Figure 3.19 Optical band gap of $\text{BaHf}_{0.6}\text{Ti}_{0.4}\text{O}_3$. Bandgap fitting is performed assuming direct bandgap.

Figure 3.20 Percolation path formation model in heterogeneous $\text{BaHf}_{0.6}\text{Ti}_{0.4}\text{O}_3$ system. In Ti-rich regions, defects are more easily generated compared to Hf-rich regions when electric field is applied, forming the conductive regions. Continuous overlap of conductive region results in formation of a percolating path, finally leading to a large leakage current and the dielectric breakdown which involves irreversible damage to the dielectric layer.

Chapter 4.

Figure 4.1 Interfacial low-k capacitance model between dielectric and electrodes.

Figure 4.2 Soft phonon density propagation model depending on interfacial

bonding.

Figure 4.3 Thickness dependent dielectric constant of BHTO.

Figure 4.4 Inverse capacitance per area of BHTO depending on the dielectric thickness.

Figure 4.5 (a) Thickness dependent dielectric constant of BSHO (b) Inverse capacitance per area of BSHO depending on the dielectric thickness.

Figure 4.6 Schematic of BHTO MIM capacitors. Top electrode is replaced to ITO.

Figure 4.7 Comparison of BHTO MIM capacitors with top 4% BLSO electrodes and ITO electrodes. (a) Dielectric constants (b) Interfacial capacitance.

Figure 4.8 Comparison of BHTO MIM capacitors with top SRO electrodes and ITO electrodes. (a) Average dielectric constants (b) Interfacial capacitance when using average dielectric constants.

Figure 4.9 Comparison of BHTO MIM capacitors with top SRO electrodes and ITO electrodes. (a) Average dielectric constants (b) Interfacial capacitance when using greatest dielectric constants.

Figure 4.10 RSM of SRO/BHTO/ITO capacitors and derived lattice parameters.

Chapter 5.

Figure 5.1 Dielectric properties of SrHfO_3 . (a) Frequency-dependent capacitance curve of SHO capacitors deposited in 30 mTorr. The inset shows the structure of SrHfO_3 metal-insulator-metal (MIM) capacitors. 4% BLSO are used as bottom and top electrodes. (b) Leakage current density (J) – Electric field (E) characteristic of SHO capacitors deposited in 30 mTorr. Black dotted line represents the breakdown field.

Figure 5.2 DC electric field dependence of dielectric constant for SHO dielectric deposited in various oxygen partial pressures. Significant dependence of dielectric

constant on DC electric field was not observed, implying SHO is linear dielectric material.

Figure 5.3 Leakage current density vs. electric field measured in two different modes. In a slow and quiet mode, the tens of pA current level dropped to a few pA.

Figure 5.4 Comparison of leakage current density of SrHfO₃ capacitors. (a–c) Leakage current density vs. electric field for SrHfO₃ capacitors deposited in 1, 10, and 100 mTorr, respectively. The thicknesses of SHO are between 50 and 60 nm. Black dotted line represents the breakdown field.

Figure 5.5 Dielectric properties of SrHfO₃ capacitors deposited at various oxygen partial pressures. The leakage current densities are measured at 2 MV cm⁻¹.

Figure 5.6 Analysis of Fowler-Nordheim tunneling and comparison of band levels. (a) $\ln(J E^{-2})$ vs. E^{-1} plot for Fowler-Nordheim analysis of BHO, LSO, LIO and SHO capacitors deposited in 30 mTorr using the following relation, $J \propto E^2 \exp\left(\frac{-4\sqrt{2m_{SHO}^*}\phi^2}{3ehE}\right)$. (b) Comparison of the band levels of high-k perovskite oxides, BHO, LSO, LIO and SHO, with respect to BSO and Si.

Figure 5.7 Optical band gap of SHO thin films grown on MgO (001) substrate. Tauc's plot for (a) direct band gap and (b) indirect band gap for SHO thin films grown in 1, 10, 30, and 100 mTorr. The inset in (a) and (b) show a magnified view of the photon energy from (a) 6.0 to 6.5 eV and (b) 5.0 to 6.5 eV, respectively. The colored dotted lines in the inset show extrapolation of the linear part. In the case of SHO thin films deposited in 30 mTorr, direct band gap and indirect band gap are estimated to be 6.25 eV and 5.85 eV, respectively.

Figure 5.8 Comparison of leakage current density for binary and ternary gate oxides. High-k SrHfO₃ perovskite dielectric has ultra-low leakage current density ($< 10^{-8}$ A cm⁻² at 2 MV cm⁻¹) compared to other oxides.

Figure 5.9 FET in an n-type accumulation mode made with 0.3% La-doped BaSnO₃ channel layer and SrHfO₃ gate oxide. (a) A schematic of the device. (b) The top view of the device pictured by an optical microscope. White dotted lines are plotted to illustrate each deposited layer. The channel length (L) of 0.3% La-doped BaSnO₃ is 60 μm, and the average channel width (W) is 140 μm. The gate

length (L) is 70 μm . (c, d) The output and transfer characteristic of the device, respectively.

Figure 5.10 X-ray diffraction (XRD) of SHO FET. (a) θ -2 θ scan and (b) rocking curves for FET with SHO gate oxide deposited in 30 mTorr.

Figure 5.11 Threshold voltage (V_{th}) of the device in the saturation region. V_{th} extracted by the linear extrapolation of $\sqrt{I_D}$ vs V_{GS} plot is estimated to be 6 V.

Figure 5.12 Reciprocal space mapping (RSM) measurement. (a) RSM (013) images for SHO capacitors deposited in 1, 10, 30, and 100 mTorr. The red, green, and black dotted lines represent the peak position for SHO, 4% BLSO, and STO, respectively. (b) The in-plane (a_{ip}), out-of-plane lattice constant (a_{op}), and unit cell volume ($V_{\text{unit cell}}$) for SHO calculated from the RSMs.

Figure 5.13 RSM (013) measurement for SHO capacitors deposited in 30 mTorr. (a) The RSM (013) images measured by rotating the devices 0° , 90° , 180° , and 270° from the left. (b) The in-plane, out-of-plane and unit cell volume of SHO calculated from the RSM (013) images.

Figure 5.14 X-ray reflectivity (XRR) measurement for SHO thin films. The experimental data of SHO thin films grown at 1, 10, 20, 30, 50, and 100 mTorr. The thickness of the films is calculated from the critical angle and fringes. All films have a thickness in the range of 45–55 nm.

Figure 5.15 Reciprocal space mapping (RSM) measurement. (a) RSM (013) images for SHO thin films deposited in 1, 10, 30, and 100 mTorr on STO substrates. (b) The in-plane (a_{ip}), out-of-plane lattice constant (a_{op}), and unit cell volume ($V_{\text{unit cell}}$) for SHO calculated from the RSMs.

Figure 5.16 X-ray diffraction measurement. (a) θ -2 θ scan and rocking curves for SrHfO_3 thin films grown in various oxygen partial pressures. The energy fluence and growth temperature are fixed at 1.3 J cm^{-2} and 750°C , respectively. Black dotted line represents the 2 θ peak position of STO. (b) The out-of-plane lattice constant of SHO thin films vs. oxygen partial pressures. (c) The intensity ratio of the narrow component to the broad component in the rocking curves.

Figure 5.17 (a, b) The XPS spectra of Sr 3d and Hf 4f region for SHO thin films deposited in various oxygen partial pressures. (c) Cation stoichiometric ratio in SHO thin films grown in different oxygen partial pressures is calculated from the XPS spectra. The compositional ratios are obtained by integrating the area of Sr 3d and Hf 4f core levels and dividing the area into relative sensitivity factors (RSF) to scale the peak areas. (d) Cation stoichiometric ratio in SHO thin films grown on MgO (001) substrate is obtained through ICP-AES measurements.

Figure 5.18 X-ray diffraction (XRD) measurement for SHO thin films. (a) θ -2 θ scan and rocking curves for SrHfO₃ thin films on SrTiO₃ (001) substrate grown at various energy fluence and growth temperature. The oxygen partial pressure is fixed at 30 mTorr. Black dotted line represents the 2 θ peak position of STO. Red and black lines represent the result of fitting rocking curves by using Voigt functions with narrow and broad linewidth, respectively. (b) The out-of-plane lattice constant of SHO thin films vs. energy fluence. (c) The value of full width at half maximum (FWHM) calculated from the rocking curves.

Figure 5.19 Deconvolution of rocking curves for SHO (002). (a–f) The rocking curves for SHO thin films on STO substrate grown in 1, 10, 20, 30, 50 and 100 mTorr, respectively. Black and yellow lines show the results of deconvolution of rocking curves for SHO (002) by using Voigt functions with broad and narrow linewidth, respectively.

Figure 5.20 The results of deconvolution of the 2 θ peak for SHO by using the Voigt functions (black and red line). Symmetric 2 θ peak for SHO deposited in 30 and 100 mTorr is fitted by only one Voigt function, whereas asymmetric one is deconvoluted into two Voigt functions.

Figure 5.21 (a) Cross-sectional STEM images of the SHO capacitors grown in 30 mTorr. Magnified HAADF-STEM image of the SHO-BLSO interface (yellow box) is presented at the bottom. The interface is indicated with the dashed line. (b) EDX elemental maps (in atomic percentage) of the SHO film. Color codes: Sr-blue, Ba-green, Hf-red, and Sn-magenta. Sr-deficient regions are marked with yellow arrows. (c) HAADF- and BF-STEM images of the SHO film showing misoriented grains (yellow arrows) and amorphous regions (green arrows).

List of Tables

Chapter 1.

Table 1.1 Comparison of high-k materials.

Chapter 3.

Table 3.1 Calculated thickness of BHTO with different set of angles from Kiessig fringes. From the Bragg's law, $2d\sin\theta = n\lambda$, thickness of film d is calculated for each θ , which corresponds to n^{th} , $n+1^{\text{th}}$, $n+2^{\text{th}}$ \cdots peak. Integer n is determined for the minimum standard deviation of the calculated thicknesses. From the smoothing function of subtracted intensity, the 2θ angles of Kiessig fringes are determined to $2\theta_1=43.4748^\circ$, $2\theta_2=43.5216^\circ$, $2\theta_3=43.5716^\circ$, $2\theta_4=43.6164^\circ$, $2\theta_5=43.6660^\circ$ respectively ($\lambda = 0.15406 \text{ nm}$).

Table 3.2 Calculated dielectric constant of BHTO from different kinds of approximations. $f_{\text{BHO}}=0.6$ and $f_{\text{BTO}}=0.4$ were used.

Chapter 4.

Table 4.1 Comparison of interfacial capacitance in various dielectric [1,3,21-23].

Chapter 1. Introduction

1.1. Needs for high-k

In recent decades, Si-based technology has been miniaturized to reduce thermal heating and power consumption. Capacitance of oxides is simply expressed as

$$C = \frac{k\epsilon_0 A}{t} \quad (1.1)$$

where ϵ_0 , k , A , t are the permittivity of free space, the relative dielectric constant, the area, the oxide thickness respectively. The area per a capacitor has been diminished continuously by the Moore's law of scaling [1]. This requires higher capacitance, which can be achieved by lowering the operating voltage. However, as the device size reduces, the gate oxide becomes thinner, resulting in increased leakage current through direct tunneling, especially for the physical thickness of SiO_2 below 1.2 nm [2]. This limits device performance and reliability. To overcome this issue, researchers have explored high-k materials that can provide the necessary capacitance with a thicker gate oxide. High-k dielectrics must have both high dielectric constant and high dielectric strength under high electric field to be suitable for use as gate dielectric materials in Si-based devices. Also, the leakage current of the device is crucial issue for high-k dielectrics.

1.2. History of high-k

From the first invention of semiconductor-based transistor with Ge in 1947, the advancement of electronic devices has been continued. However, the actual significant progress occurred when the manufacturing of transistors started using silicon (Si) and silicon-dioxide (SiO_2) [3]. The abundance of silicon on earth makes the price of silicon affordable and easy formation of SiO_2 , which has excellent

insulating properties, is the main reason of success of Si-based industry. However, as the scaling progresses, the issue of gate leakage through direct tunneling intensified. To address gate leakage issues and prolong the effectiveness of SiO₂-based dielectric, the addition of nitrogen to SiO₂ has been implemented in the 1990's [3,4]. The inclusion of nitrogen in SiO₂ enhances not only the dielectric constant (5-7) but also functions as a more effective obstruction against boron infiltration. This is 2nd generation gate-oxide. Although SiON has undergone significant advancements, oxynitrides still exhibit low k values, necessitating a relatively thick layer to impede direct tunneling current. Al₂O₃, Y₂O₃, La₂O₃, Sc₂O₃, which are oxides of group II, III, IV and certain lanthanides including Pr₂O₃, Gd₂O₃, and Lu₂O₃ have been suggested as possible alternatives [4]. Regrettably, these dielectrics had a short lifespan limited by factors such as low power applications, scalability, or severe reactions with the Si substrate. However, the issues mentioned above are significantly less problematic for oxides and silicates of Hf and Zr. Consequently, the selection of substitute gate dielectrics has been limited to HfO₂, ZrO₂, and their silicates, owing to their outstanding electrical characteristics and high thermal resilience when in contact with Si. Regarding SiHfON and its generation (3rd generation gate-oxide), these substances have been scaled to sub-1nm EOT values and was manufactured for the 45nm technology node, utilizing metal-gate materials instead of the standard polysilicon gate material [3]. However, further scaling requires high-k gate oxide with higher dielectric constants. Designing and creating 4th generation gate-oxide logic devices is of great interest to engineers and physicists. For the 4th generation gate-oxide, ternary perovskite oxides and its alloys such as SrTiO₃, (Ba,Sr)TiO₃ (BST) are considered as candidates for their large dielectric constants. Commensurate crystalline oxide

interface with silicon was reported between SrTiO_3 and silicon, totally avoiding the amorphous silica (SiO_x) phase, suggesting that the perovskite oxides can be integrated with Si [5].

1.3. Comparison of high-k dielectrics

Research has explored binary oxides with a significant bandgap (E_g), including Y_2O_3 [6] and Al_2O_3 [6,7], but their dielectric constants fall short. TiO_2 [6,8-11] and Ta_2O_5 [7,12,13] are high-k materials but are unstable on silicon [6,8,13]. On the other hand, binary oxides such as HfO_2 [11,14], ZrO_2 [11,15] and La_2O_3 [7,16] are ideal high-k materials on silicon, and commercial products employing these materials are already available in the semiconductor market for CPU, DRAM, and flash memory applications [2]. However, with the continued scaling down of semiconductor devices, future applications will require high-k materials with even greater dielectric constants and lower leakage currents.

The investigation of ternary (complex) oxide materials is another area of interest, as their dielectric constants tend to be higher than binary oxides. Hafnium-based materials (AHfO_3) and titanium-based materials (ATiO_3) have been extensively studied, including SrHfO_3 [17-19], SrTiO_3 [7,20,21], and BaTiO_3 [21-23]. While the dielectric properties of SrHfO_3 are no better than existing high-k dielectrics such as HfO_2 , SrTiO_3 and BaTiO_3 have remarkably high dielectric constants. However, their leakage current characteristics and dielectric strength are poor, making them impractical for use in devices. Hafnium-based materials, specifically BaHfO_3 [24-26], are considered promising candidates due to their thermal stability. Our group and others have already investigated BaHfO_3 , a perovskite high-k oxide material

with a dielectric constant of 23-38 and a breakdown field of about 3.6 MV/cm [24].

	Material	k	Bandgap (eV)	E _{BD} (MV/cm)	J (A/cm ²) @ E (MV/cm)
Binary Oxide	Y ₂ O ₃	15	5.6	4	10 ⁻¹⁰ @ 1.9
	Al ₂ O ₃	9	8.7	7.2	10 ⁻¹ @ 7.2
	TiO ₂	24- 110	3.5	1.4-2.5	10 ⁻¹ @ 1
	Ta ₂ O ₅	25	4.4	2.5-4.2	10 ⁻⁴ @ 1
	HfO ₂	25	5.7	3.9-6.7	10 ⁻⁴ @ 5
	ZrO ₂	20	5-7	3.3-5.7	10 ⁻⁴ @ 5
	La ₂ O ₃	27	5.5	4.2	10 ⁻³ @ 4
Ternary Oxide	SrHfO ₃	20- 35	6	3.3	10 ⁻⁴ @ 3
	SrTiO ₃	100- 300	3.3	1-3	10 ⁻⁵ @ 1
	BaTiO ₃	400	3.3	0.7	10 ⁻³ @ 0.5
	BaHfO ₃	37.8	6.1	3.6	10 ⁻² @ 3

Table 1.1 Comparison of high-k materials.

References

- [1] G. E. Moore, *Electron Devices Meeting, 1975 International*. (1975).
- [2] J. Robertson, R. M. Wallace, *Mater. Sci. Eng.* **88**, 1-41 (2015).
- [3] U. Sharma, G. Kumar, S. Mishra, R. Thomas, *J. Phys. Conf. Ser.* **2267**, 012142 (2022).
- [4] A. P. Huang, Z. C. Yang, P. K. Chu, in *Advances in Solid State Circuits Technologies* (IntechOpen, 2010), pp. 333-350.
- [5] R. A. McKee, F. J. Walker, M. F. Chisholm, *Phys. Rev. Lett.* **81**, 3014–3017 (1998).
- [6] G. D. Wilk, R. M. Wallace, J. M. Anthony, *J. Appl. Phys.* **89**, 5243–5275 (2001).
- [7] J. McPherson, J. Kim, A. Shanware, H. Mogul, J. Rodriguez, *IEEE Dig. Int. Electron Devices Meet.*, 633–636 (2002).
- [8] M. Kadoshima, M. Hiratani, Y. Shimamoto, K. Torii, H. Miki, S. Kimura, T. Nabatame, *Thin Solid Films* **424**, 224-228 (2003).
- [9] M. Shin, M. R. D. Guire, A. H. Heuer, *J. Appl. Phys.* **83**, 3311–3317 (1998).
- [10] M.-K. Lee, C.-F. Yen, *Act. Passiv. Electron. Compon.* **2012**, 148705 (2012).
- [11] J. H. Choi, Y. Mao, J. P. Chang, *Mater. Sci. Eng. R Rep.* **72**, 97–136 (2011).
- [12] J.-L. Autran, R. Devine, C. Chaneliere, B. Bernard, *IEEE Electron Device Lett.* **18**, 447–449 (1997).
- [13] V. A. Shvets, V. S. Aliev, D. V. Gritsenko, S. S. Shaimeev, E. V. Fedosenko, S. V. Rykhlitski, V. V. Atuchin, V. A. Gritsenko, V. M. Tapilin, H. Wong, *J. Non Cryst. Solids* **354**, 3025–3033 (2008).
- [14] B. H. Lee, L. Kang, W.-J. Qi, R. Nieh, Y. Jeon, K. Onishi, J. C. Lee, in *Proceedings of the IEEE Technical Digest. International Electron Devices Meeting* (IEEE, 1999), pp. 133–136.
- [15] C. M. Perkins, B. B. Triplett, P. C. McIntyre, K. C. Saraswat, S. Haukka, M. Tuominen, *Appl. Phys. Lett.* **78**, 2357–2359 (2001).
- [16] J. Chen, T. Kawanago, H. Wakabayashi, K. Tsutsui, H. Iwai, D. Nohata, H. Nohira, K. Kakushima, *Microelectron. Reliab.* **60**, 16–19 (2016).
- [17] M. D. McDaniel, C. Hu, S. Lu, T. Q. Ngo, A. Posadas, A. Jiang, D. J. Smith, E. T. Yu, A. A. Demkov, J. G. Ekerdt, *J. Appl. Phys.* **117**, 054101 (2015).
- [18] G. Lupina, G. Kozlowski, J. Dabrowski, P. Dudek, G. Lippert, H.-J. Mussig, *Appl. Phys. Lett.* **93**, 252907 (2008).
- [19] A. Feteira, D. C. Sinclair, K. Z. Rajab, M. T. Lanagan, *J. Am. Ceram. Soc.* **91**, 893–901 (2008).

- [20] K. Abe, S. Komatsu, *Jpn. J. Appl. Phys.* **32**, 4186–4189 (1993).
- [21] J. H. Shim, H. J. Choi, Y. Kim, J. Torgersen, J. An, M. H. Lee, F. B. Prinz, *J. Mater. Chem. C* **5**, 8000–8013 (2017).
- [22] J. Cheng, C. Wang, C. Freeze, O. Shoron, N. Combs, H. Yang, N. K. Kalarickal, Z. Xia, S. Stemmer, S. Rajan, W. Lu, *IEEE Electron Device Lett.* **41**, 621–624 (2020).
- [23] S. Cho, C. Yun, Y. S. Kim, H. Wang, J. Jian, W. Zhang, J. Huang, X. Wang, H. Wang, J. L. M-Driscoll, *Nano Energy* **45**, 398–406 (2018).
- [24] Y. M. Kim, C. Park, T. Ha, U. Kim, N. Kim, J. Shin, Y. Kim, J. Yu, J. H. Kim, K. Char, *APL Mater.* **5**, 016104 (2017).
- [25] G. Lupina, G. Kozlowski, J. Dabrowski, Ch. Wenger, P. Dudek, P. Zaumseil, G. Lippert, Ch. Walczyk, H.-J. Mussig, *Appl. Phys. Lett.* **92**, 062906 (2008).
- [26] T. Maekawa, K. Kurosaki, S. Yamanaka, *J. Alloys Compd.* **407**, 44–48 (2006).

Chapter 2. Properties of $\text{BaHf}_{1-x}\text{Ti}_x\text{O}_3$ (BHTO)

2.1. Research background

As I mentioned in chapter 1, BaHfO_3 (BHO) is a material with high dielectric constant (~ 30) and large bandgap (~ 6.1 eV) [1,2], which is related to high breakdown field and low leakage current. On the other hand, BaTiO_3 (BTO) is well known ferroelectric perovskite oxide. The reason for the ferroelectric behavior of BaTiO_3 is the displacement of titanium atoms within TiO_6 octahedra [3]. Additionally, ferroelectric materials are easily influenced by external fields due to their high polarizability, which is related to the presence of high leakage current. The dielectric constant of BTO single crystal is 4500 at room temperature [4], which is extremely high. However, the dielectric constant of BTO thin films reduces to about 400 [5,6]. This is well known problem of dielectric materials, called “size effect”. I will discuss this later. Even in BTO single crystal, the dielectric breakdown field is $0.3\sim 0.5$ MV/cm [7], which is very low. If we combine the two materials, BHO and BTO, there may exist an optimum ratio that maintains a high dielectric constant, large breakdown field, and low leakage current. As the titanium ratio increases, the dielectric constant will also increase, but the breakdown field will decrease.

2.2. Dielectric properties of $\text{BaHf}_{1-x}\text{Ti}_x\text{O}_3$ (BHTO) system

The growth of all the samples took place on SrTiO_3 or MgO substrates, at a temperature of 750°C , and under an oxygen partial pressure of 100 mTorr. The process involved using a KrF excimer laser with a wavelength of 248 nm, which

was operated at an energy fluence of approximately 1.2-1.5 J/cm². The material targets for the samples were provided by Toshima Manufacturing Co. in Japan. To create a lateral pattern, a stencil mask made of Si or stainless steel was utilized. The electrical properties of the samples were analyzed using the Keithley 4200 semiconductor characterization system. To measure electrical properties of BaHf_{1-x}Ti_xO₃ dielectric, epitaxially grown 4 % La-doped BaSnO₃ on SrTiO₃ substrate was used both as the top and the bottom electrodes in a metal-insulator-metal (MIM) capacitor structure. BaHf_{1-x}Ti_xO₃ (~150 nm) dielectric layer was grown between the two electrodes by sequential ablation of the two targets (BaHfO₃, BaTiO₃), making sure the growth rate per a cycle does not exceed a unit cell so that Hf and Ti atoms can be uniformly mixed in a unit cell. The area of the top 4 % La-doped BaSnO₃ electrode is about 53,100 μm². By applying an AC voltage with a root-mean-square amplitude of 30 mV, we were able to derive the parallel capacitance (C_p) and dissipation factor (tan δ) from admittance. The dielectric constants (k) of BaHf_{1-x}Ti_xO₃ were then calculated using the obtained C_p values. To evaluate the breakdown field (E_{BD}), we measured the leakage current that flowed through the capacitors. The dielectric constants of BaHf_{1-x}Ti_xO₃ system are shown in Figure 2.1.

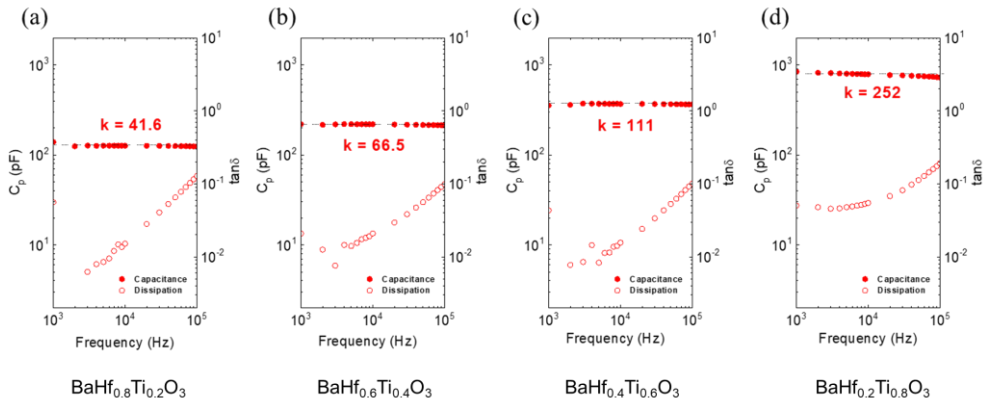


Figure 2.1 Dielectric constants of BaHf_{1-x}Ti_xO₃ system (a) BaHf_{0.8}Ti_{0.2}O₃ (b) BaHf_{0.6}Ti_{0.4}O₃ (c) BaHf_{0.4}Ti_{0.6}O₃ (d) BaHf_{0.2}Ti_{0.8}O₃.

As expected, the dielectric constant increases as the titanium ratio increases. The breakdown field of $\text{BaHf}_{1-x}\text{Ti}_x\text{O}_3$ system are shown in Figure 2.2.

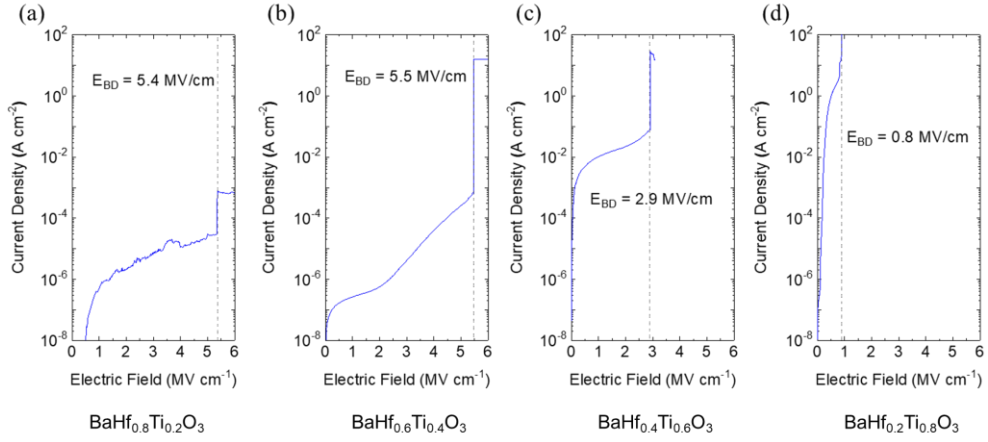


Figure 2.2 Breakdown field of $\text{BaHf}_{1-x}\text{Ti}_x\text{O}_3$ system (a) $\text{BaHf}_{0.8}\text{Ti}_{0.2}\text{O}_3$ (b) $\text{BaHf}_{0.6}\text{Ti}_{0.4}\text{O}_3$ (c) $\text{BaHf}_{0.4}\text{Ti}_{0.6}\text{O}_3$ (d) $\text{BaHf}_{0.2}\text{Ti}_{0.8}\text{O}_3$.

Figure 2.3 is the summary of the dielectric properties of $\text{BaHf}_{1-x}\text{Ti}_x\text{O}_3$ films which shows calculated dielectric constants, breakdown fields and corresponding maximum field-induced 2D charge densities calculated by following formula as

$$n_{2D} = \frac{\epsilon_0 k E_{BD}}{q} \quad (2.1)$$

where ϵ_0 , k , E_{BD} and q are the permittivity of free space, the relative dielectric constant, the breakdown field, elementary charge respectively. Dielectric constant increases as the Ti ratio increases, which can be predicted considering the dielectric constants of BaHfO_3 and BaTiO_3 . However, the breakdown field of the $\text{BaHf}_{1-x}\text{Ti}_x\text{O}_3$ dielectric does not decrease significantly until the titanium ratio reaches 50%, after which it experiences a steep decline. This rapid decrease in the breakdown field may be attributed to the formation of conducting pathways resulting from the networks of TiO_6 octahedra as the Ti ratio increases. Electrical measurements indicate that the dielectric constant of $\text{BaHf}_{0.6}\text{Ti}_{0.4}\text{O}_3$ is

approximately 65 to 70, while its corresponding breakdown field is about 5 MV/cm, resulting in a potential field-induced charge density of $2 \times 10^{14} \text{ cm}^{-2}$.

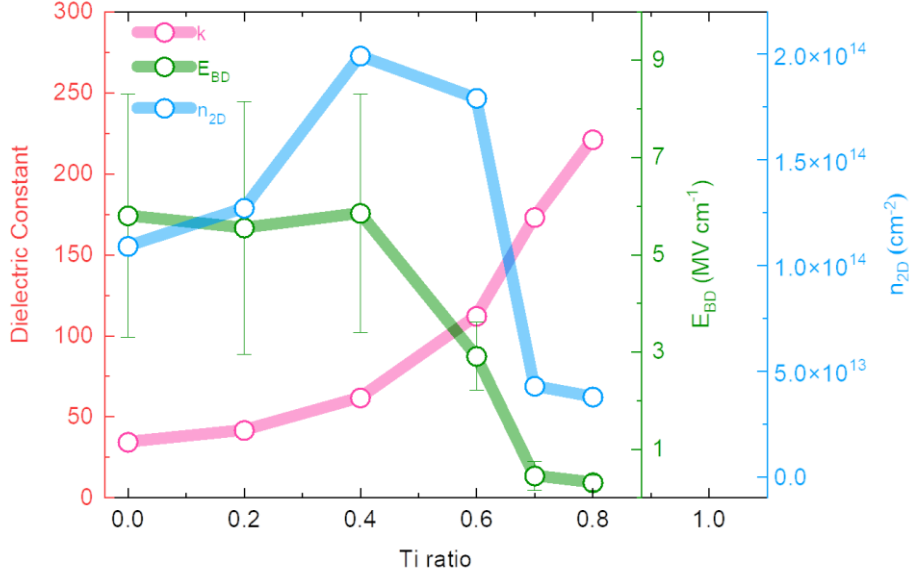


Figure 2.3 Dielectric constants and breakdown fields of BHTO, 2-dimensional carrier density which BHTO can modulate with various alloying ratios.

Comparison between theoretical and experimental dielectric constant are shown in Figure 2.4. Theoretical dielectric constants were calculated by an effective medium theory as follows.

$$\frac{\varepsilon_{BHTO}-1}{\varepsilon_{BHTO}+2} = f_{BHO} \frac{\varepsilon_{BHO}-1}{\varepsilon_{BHO}+2} + f_{BTO} \frac{\varepsilon_{BTO}-1}{\varepsilon_{BTO}+2}, \quad (2.2)$$

where ε_{BHTO} , ε_{BHO} , and ε_{BTO} are dielectric constants of $\text{BaHf}_{1-x}\text{Ti}_x\text{O}_3$, BaHfO_3 , and BaTiO_3 , respectively, and f_{BHO} , and f_{BTO} are volume fractions of BaHfO_3 , and BaTiO_3 , respectively. The dielectric constant of BaHfO_3 , $\varepsilon_{BHO} = 37.8$ [1] and that of BaTiO_3 $\varepsilon_{BTO} = 400$ and 4000 [5,8] were used to calculate ε_{BHTO} . The dielectric constants obtained from both theory and experimentation match well for titanium ratios below 50%. However, as the proportion of titanium increases beyond this

point, the experimental values surpass the theoretical ones. This inconsistency is attributed to limitations in the predictive model used. Later, I will discuss this using various model.

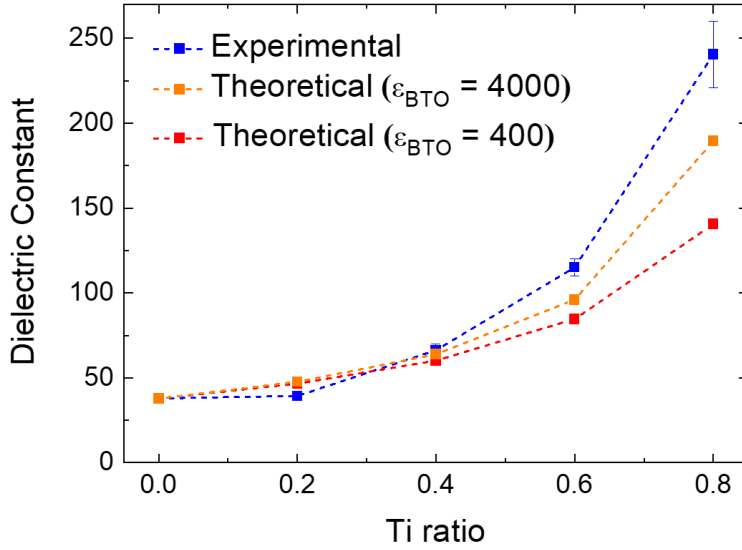


Figure 2.4 Calculation of dielectric constants of BHTO as a function of the alloying ratio calculated by effective medium theory.

To obtain the statistics for the dielectric constant and breakdown field of $\text{BaHf}_{0.6}\text{Ti}_{0.4}\text{O}_3$, we created 18 capacitors and analyzed their electrical properties as shown in Figure 2.5. These capacitors were all produced under identical conditions on a single chip. The statistically averaged dielectric constant for $\text{BaHf}_{0.6}\text{Ti}_{0.4}\text{O}_3$ was found to be 63.30, with most values falling between 60 and 65. The statistically averaged breakdown field was 5.42 MV/cm, with a larger deviation compared to the dielectric constant. This difference may be attributed to the fact that dielectric breakdown is more dependent on local defects in each capacitor.

Therefore, the maximum measured breakdown field, rather than the average, represents the intrinsic dielectric strength.

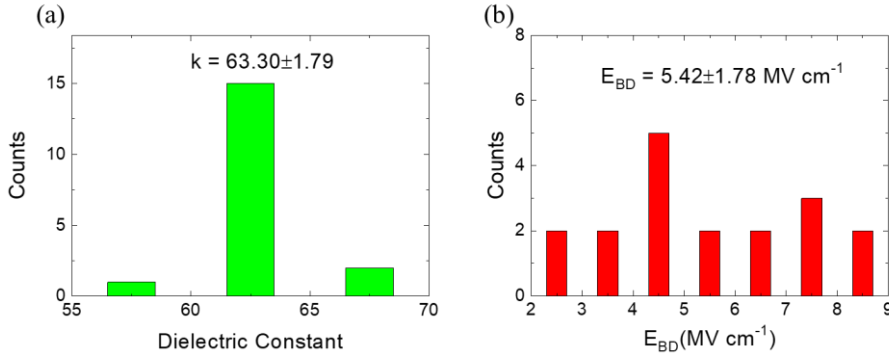


Figure 2.5 Statistical measurement data of (a) dielectric constant and (b) breakdown field of BaHf_{0.6}Ti_{0.4}O₃.

2.3. Structural properties of BaHf_{1-x}Ti_xO₃ (BHTO) system

The structural properties of BaHf_{1-x}Ti_xO₃ were assessed using x-ray diffraction. To begin with, a 150 nm layer of 4% La-doped BaSnO₃ was grown as the bottom electrode on SrTiO₃ substrates, followed by epitaxial growth of a 150 nm layer of BaHf_{1-x}Ti_xO₃ on top of it. Reciprocal space mapping was carried out on the BaHf_{1-x}Ti_xO₃ (103) peaks, as displayed in Figure 2.6. It was observed that as the titanium ratio increased, the Q_z and Q_x peak values also increased. Figure 2.7 indicated the corresponding in-plane and out-of-plane lattice parameters, a and c . As the titanium ratio increased, the lattice parameters predictably decreased, given that the cubic BaHfO₃ bulk lattice parameter is $a = 4.171 \text{ \AA}$ [1] and the tetragonal BaTiO₃ bulk lattice parameters are $a = 4.000 \text{ \AA}$, $c = 4.027 \text{ \AA}$ [3]. Figure 2.6 (b) and Figure 2.7 indicated that the lattice parameters of BaHf_{0.6}Ti_{0.4}O₃ matched well with the lattice parameters of 4% La-doped BaSnO₃ ($a = 4.107 \text{ \AA}$, $c = 4.127 \text{ \AA}$), preventing the formation of new dislocations at their interface.

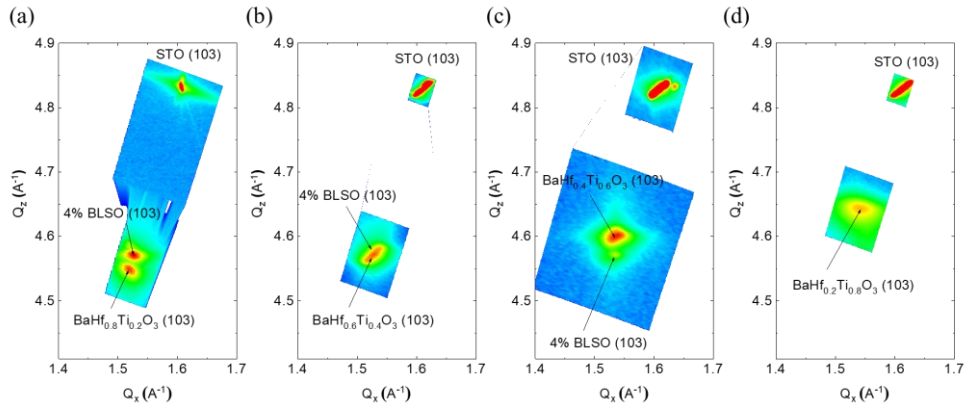


Figure 2.6 RSM of BHTO with various alloying ratios on BLSO (a) $\text{BaHf}_{0.8}\text{Ti}_{0.2}\text{O}_3$ (b) $\text{BaHf}_{0.6}\text{Ti}_{0.4}\text{O}_3$ (c) $\text{BaHf}_{0.4}\text{Ti}_{0.6}\text{O}_3$ (d) $\text{BaHf}_{0.2}\text{Ti}_{0.8}\text{O}_3$.

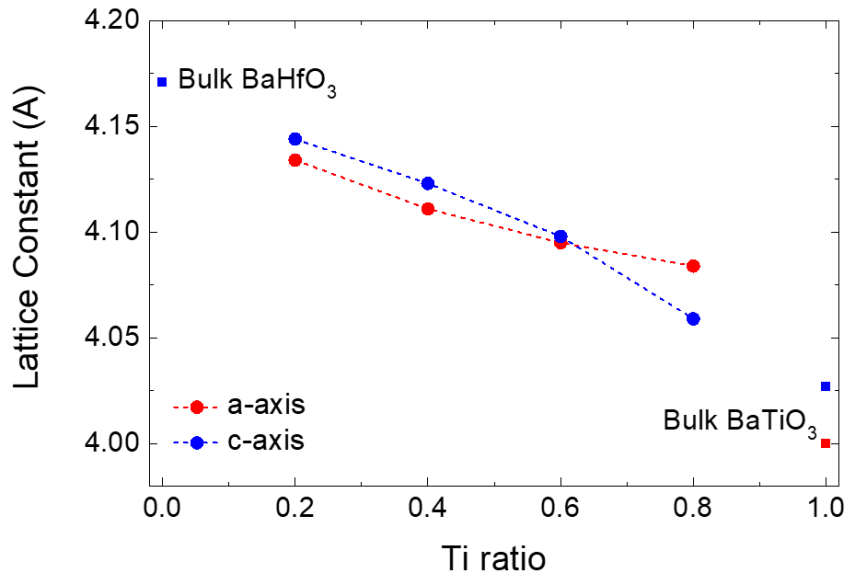


Figure 2.7 Lattice constant derived from RSM of BHTO with various alloying ratios on BLSO.

2.4. Optical properties of $\text{BaHf}_{1-x}\text{Ti}_x\text{O}_3$ (BHTO) system

The optical bandgap of $\text{BaHf}_{1-x}\text{Ti}_x\text{O}_3$ was determined using optical absorption measurement in Jae Hoon Kim's lab in Yonsei university, as shown in Figure 2.8. To avoid substrate absorption, an MgO substrate with a BaHfO_3 buffer layer was used for the growth of the $\text{BaHf}_{1-x}\text{Ti}_x\text{O}_3$ layer. The bandgap of $\text{BaHf}_{0.8}\text{Ti}_{0.2}\text{O}_3$ was measured to be 4.32 eV, which is a significant decrease in comparison to the bandgap of BaHfO_3 (6.1 eV) [1] and BaTiO_3 (3.1 eV) [9]. Normally, the dielectric strength of a material increases with the increase in its bandgap [10,11]. For example, GaN has a bandgap of 3.4 eV with a breakdown field of 3.3 MV/cm, while $\beta\text{-Ga}_2\text{O}_3$ with a bandgap of 4.7 eV has a breakdown field of up to 8 MV/cm [11]. The bandgap of $\text{BaHf}_{0.6}\text{Ti}_{0.4}\text{O}_3$ was measured to be 4.21 eV, and its breakdown field was found to be similar to that of $\beta\text{-Ga}_2\text{O}_3$. Therefore, considering the correlation between bandgap and dielectric strength, $\text{BaHf}_{0.6}\text{Ti}_{0.4}\text{O}_3$ exhibits superior dielectric strength compared to other materials with a similar bandgap.

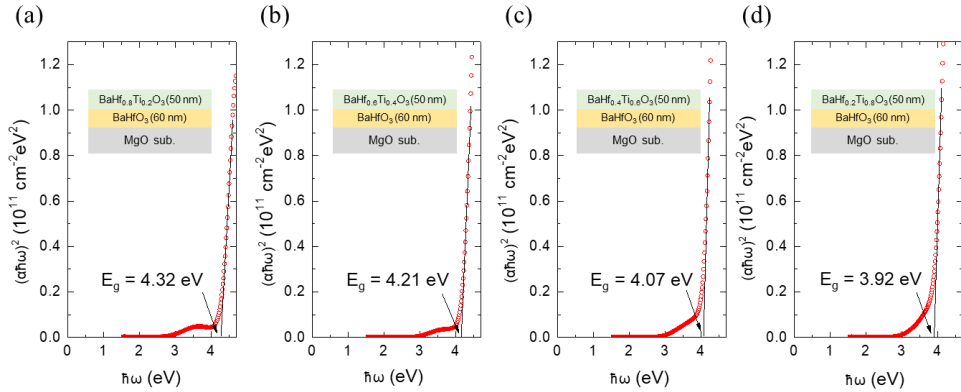


Figure 2.8 The optical bandgap of BHTO. (a) $\text{BaHf}_{0.8}\text{Ti}_{0.2}\text{O}_3$ (b) $\text{BaHf}_{0.6}\text{Ti}_{0.4}\text{O}_3$ (c) $\text{BaHf}_{0.4}\text{Ti}_{0.6}\text{O}_3$ (d) $\text{BaHf}_{0.2}\text{Ti}_{0.8}\text{O}_3$.

2.5. Field effect transistors using $\text{BaHf}_{0.6}\text{Ti}_{0.4}\text{O}_3$

Figure 2.9 shows an n-type accumulation mode field effect transistor (FET) using $\text{BaHf}_{0.6}\text{Ti}_{0.4}\text{O}_3$ as the gate oxide. Cross-sectional schematic diagram of the

device is shown in Figure 2.9(a). To reduce the threading dislocation density, 150 nm thick BaSnO₃ buffer layer was grown on a SrTiO₃ substrate. On top of it, 11 nm thick 0.3 % La-doped BaSnO₃ channel layer was grown using a silicon stencil mask patterned as a line. 4 % La-doped BaSnO₃ was grown on it through a stainless-steel mask as the source and the drain contacts, which defines the channel length. Finally, using other Si masks, 163 nm thick BaHf_{0.6}Ti_{0.4}O₃ gate oxide layer and 4 % La-doped BaSnO₃ gate electrode was grown. Figure 2.9(b) is the microscope image of the device. The channel width (W_{ch}) of 0.3 % La-doped BaSnO₃ is 230 μm , and the channel length (L_{ch}) is 60 μm . The output characteristics of the device are shown in Figure 2.9(c). The source-drain voltage (V_{DS}) was applied up to 5 V while the gate voltage (V_{GS}) varied from 7 to 0 V with the interval of 1 V. At low V_{DS} the source-drain current (I_D) is proportional to the V_{DS} and, as V_{DS} increases, I_D becomes saturated. The transfer characteristics of the device are shown in Figure 2.9(d). Gate leakage current (I_G) and I_D was measured at $V_{DS} = 1$ V while V_{GS} was swept from 0 to 7 V. I_{on}/I_{off} ratio is about 10^7 . The maximum of subthreshold swing was evaluated from the relation $S = [\partial \log(I_D)/\partial V_{GS}]^{-1}$ as 0.20 V/dec. Field effect mobility (μ_{FE}) of the device was calculated using the relation

$$\mu_{FE} = \left(\frac{Lt}{W\kappa\epsilon_0 V_{DS}} \right) \frac{\partial I_D}{\partial V_{GS}}, \quad (2.3)$$

where L , t , W and ϵ_0 are the channel length, the thickness of the BaHf_{0.6}Ti_{0.4}O₃ layer, the channel width, and the permittivity of the vacuum. The maximum of μ_{FE} is about 23 $\text{cm}^2\text{V}^{-1}\text{s}^{-1}$. Compared to the FET with BaHfO₃ gate oxide [1], although the La doping concentration is different, the V_{GS} required to modulate the current amplification of 10^7 (+1 to +7 V vs. -7 to +18 V in case of BaHfO₃) is smaller,

which is attributed to the higher dielectric constant of $\text{BaHf}_{0.6}\text{Ti}_{0.4}\text{O}_3$ than BaHfO_3 . The subthreshold swing is also smaller than that of BaHfO_3 device (0.8 V/dec) [1].

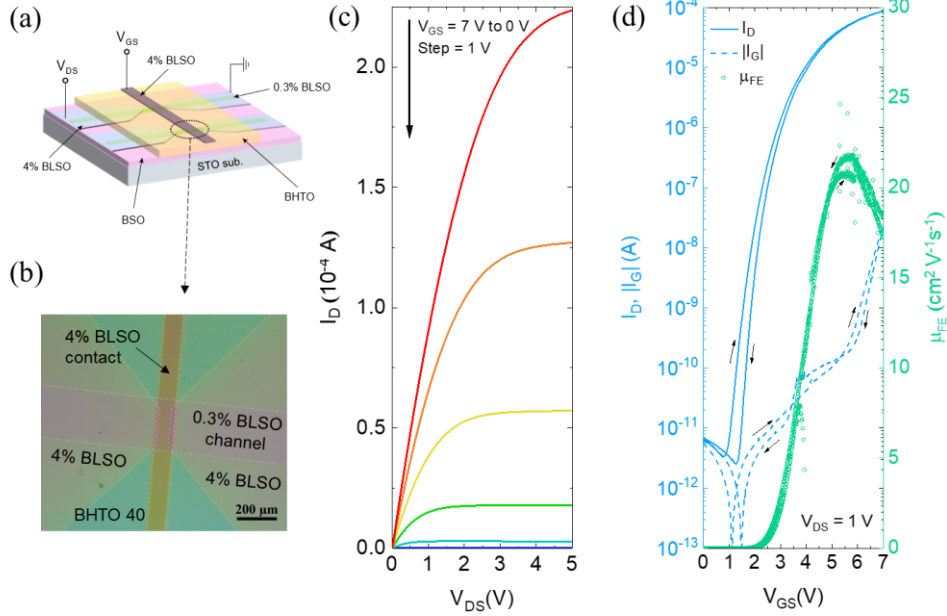


Figure 2.9 FET made with 0.3% BLSO channel layer and $\text{BaHf}_{0.6}\text{Ti}_{0.4}\text{O}_3$ gate oxide. (a) schematic of the device. (b) The top view of the device pictured by an optical microscope. (c) The output characteristic of the device. (d) Transfer characteristics of the device.

2.6. Conclusions

To summarize, we examined how the dielectric properties of the $\text{BaHf}_{1-x}\text{Ti}_x\text{O}_3$ system vary, with the goal of combining materials with high dielectric strength and high dielectric constant. $\text{BaHf}_{0.6}\text{Ti}_{0.4}\text{O}_3$ had the largest field-induced charge density, making it a potential candidate for a high-k dielectric with excellent dielectric strength. We discovered that the $\text{BaHf}_{0.6}\text{Ti}_{0.4}\text{O}_3$ dielectric can modulate carrier density greater than 10^{14} cm^{-2} . We successfully demonstrated the use of

BaHf_{0.6}Ti_{0.4}O₃ as a gate oxide in n-type accumulation mode with excellent characteristics.

References

- [1] Y. M. Kim, C. Park, T. Ha, U. Kim, N. Kim, J. Shin, Y. Kim, J. Yu, J. H. Kim, K. Char, *APL Mater.* **5**, 016104 (2017).
- [2] G. Lupina, G. Kozlowski, J. Dabrowski, Ch. Wenger, P. Dudek, P. Zaumseil, G. Lippert, Ch. Walczyk, H.-J. Mussig, *Appl. Phys. Lett.* **92**, 062906 (2008).
- [3] M.B. Smith, K. Page, T. Siegrist, P. L. Redmond, E. C. Walter, R. Seshadri, L. E. Brus, M. L. Steigerwald, *J. Am. Chem. Soc.* **130**, 6955-6963 (2008).
- [4] M. M. Vijatovic, J. D. Bobic, B. D. Stojanovic, *Sci. Sinter.* **40**, 235-244 (2008).
- [5] J. Cheng, C. Wang, C. Freeze, O. Shoron, N. Combs, H. Yang, N. K. Kalarickal, Z. Xia, S. Stemmer, S. Rajan, W. Lu, *IEEE Electron Device Lett.* **41**, 621–624 (2020).
- [6] S. Cho, C. Yun, Y. S. Kim, H. Wang, J. Jian, W. Zhang, J. Huang, X. Wang, H. Wang, J. L. M-Driscoll, *Nano Energy* **45**, 398–406 (2018).
- [7] Y. Inuishi, S. Uematsu, *J. Phys. Soc. Japan* **13**, 761~762 (1958).
- [8] J. H. Shim, H. J. Choi, Y. Kim, J. Torgersen, J. An, M. H. Lee, F. B. Prinz, *J. Mater. Chem. C* **5**, 8000–8013 (2017).
- [9] H. Matsuda, M. Kuwabara, *J. Am. Ceram. Soc.* **81**, 3010-3012 (1998).
- [10] L.-M. Wang, *IEEE 25th International Conference on Microelectronics*, 576-579, (2006).
- [11] M. Higashiwaki, K. Sasaki, A. Kuramata, T. Masui, S. Yamakoshi, *Appl. Phys. Lett.* **100**, 013504 (2012).

Chapter 3. Properties of $\text{BaHf}_{0.6}\text{Ti}_{0.4}\text{O}_3$

3.1. Research background

In chapter 2, we found that the optimum ratio of $\text{BaHf}_{1-x}\text{Ti}_x\text{O}_3$ as a high-k dielectric is at $x=0.4$ in terms of potential field-induced 2-dimensional charge density and lattice matching to 4% BLSO. In different film deposition condition, the dielectric properties of BHTO enhanced. Sequential ablation of the two targets (BaHfO_3 , BaTiO_3) was changed to single ablation of a target ($\text{BaHf}_{0.6}\text{Ti}_{0.4}\text{O}_3$) and the level of oxygen partial pressure during the deposition was altered from 100 mTorr to 10 mTorr, which could expect a structural difference.

3.2. Dielectric properties of $\text{BaHf}_{0.6}\text{Ti}_{0.4}\text{O}_3$

All material targets of BaSnO_3 , La-doped BaSnO_3 , and $\text{BaHf}_{0.6}\text{Ti}_{0.4}\text{O}_3$ (BHTO) were provided by Toshima Manufacturing Co. in Japan, which have a purity over 99.9%. The BHTO samples were grown on SrTiO_3 or MgO single-crystal substrates at a temperature of 750°C and an oxygen partial pressure of 10 mTorr, using a pulsed laser deposition system. A KrF excimer laser with a wavelength of 248 nm and an energy fluence of about 1.2 to 1.5 J cm^{-2} was employed at a repetition rate of 10 Hz. The distance between the target and substrate for BHTO was 63 mm. La-doped BaSnO_3 layers were used as the electrode and channel layer, respectively, and were deposited in an oxygen partial pressure of 100 mTorr at 750°C . Si or stainless-steel stencil masks were utilized to create lateral patterns. The thickness of the films was measured using a stylus profiler (DektakXT-E,

Bruker) or an AFM (LensAFM, Nanosurf).

The Keithley 4200 semiconductor characterization system was used to measure the electrical properties. The admittance measurement was used to obtain the parallel capacitance (C_p) and dissipation factor ($\tan \delta$) with an AC voltage of 30 mV and root mean square amplitude. To measure the breakdown field (E_{BD}), the voltage was swept while measuring the leakage current through the capacitors. In order to assess the electrical characteristics of the $\text{BaHf}_{0.6}\text{Ti}_{0.4}\text{O}_3$ dielectric, a 150 nm thick layer of 4% La-doped BaSnO_3 (referred to as 4% BLSO) was grown on top of the dielectric. This layer had a resistivity of $150 \mu\Omega \cdot \text{cm}$ and was degenerately doped [1]. The structure was created in the form of a mesa-like capacitor, with a 4% BLSO layer acting as the bottom electrode and the $\text{BaHf}_{0.6}\text{Ti}_{0.4}\text{O}_3$ layer being 200 nm thick. The thickness of BHTO was verified using Kiessig fringes obtained from x-ray diffraction, as depicted in Figure 3.1 and table 3.1. The top electrode made of 4% La-doped BaSnO_3 has a area of approximately $53,100 \mu\text{m}^2$, with a diameter of approximately $260 \mu\text{m}$. The dielectric constants of $\text{BaHf}_{0.6}\text{Ti}_{0.4}\text{O}_3$ were calculated using the measured parallel capacitance (C_p), which is presented in Figure 3.2(a) and 3.2(b) along with the capacitance-frequency and current-voltage characteristics. Figure 3.2(c) depicts the DC field dependence of the capacitance, which shows a similarity to those observed in BTO or SrTiO_3 [2,3]. The hardening of the soft phonons is the main cause of the DC field dependence of the dielectric constant in titanates [4,5]. Due to the significant bias dependence of the dielectric constant, the "effective" dielectric constant in a device is reduced, with an average dielectric constant ranging from zero to a finite bias. Figure 3.3 presents the band offset estimation

and corresponding band diagrams through Fowler-Nordheim tunneling analysis of the leakage current at high bias. The band offset between the BaSnO_3 and BHTO is in the range of 0.9~1.4 eV due to uncertainty in the effective mass of BHTO.

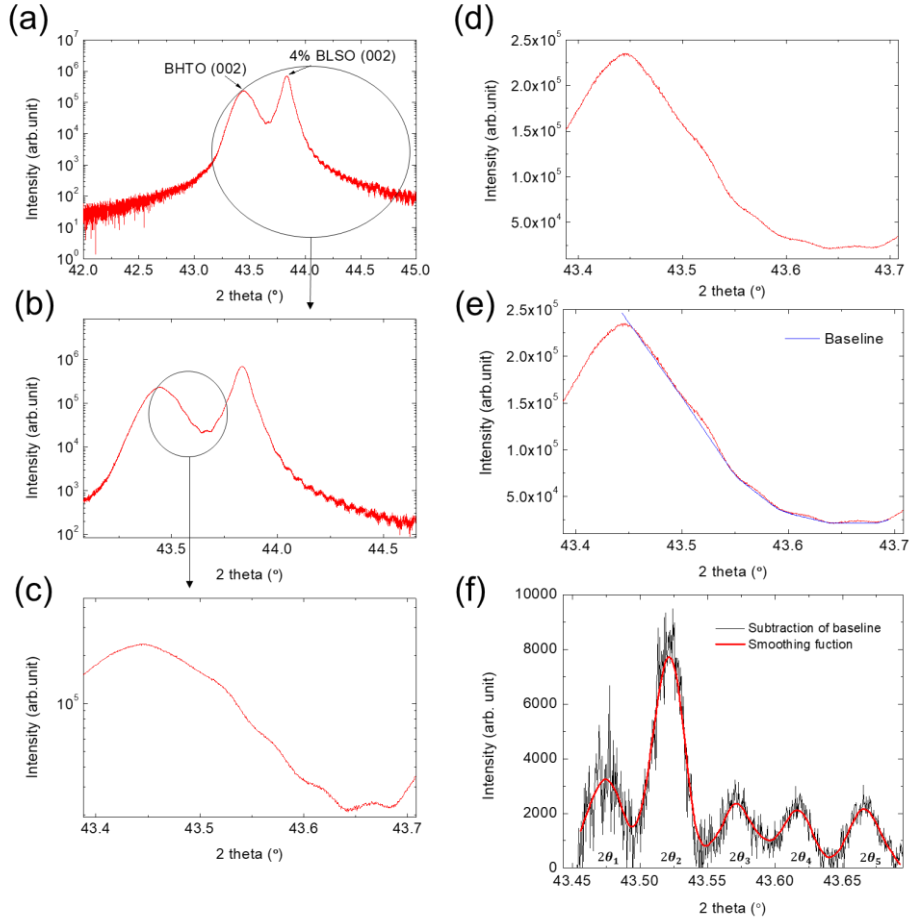


Figure 3.1 X-ray diffraction measurement of BHTO capacitor and Kiessig fringes of BHTO peak. (a), (b), (c) X-ray diffraction data of BHTO MIM capacitor and Kiessig fringes of BHTO peak. (d) Linear scale plot of Kiessig fringes of BHTO peak. (e) Baseline of the curve. (f) Subtraction of baseline, smoothing function for finding Kiessig fringe peaks.

Choice of angles	n	d (nm)
$\theta_1, \theta_2, \theta_3$	944	196.3
$\theta_2, \theta_3, \theta_4$	964	200.3
$\theta_3, \theta_4, \theta_5$	970	201.3
$\theta_1, \theta_2, \theta_3, \theta_4$	962	200.1
$\theta_2, \theta_3, \theta_4, \theta_5$	957	198.8
$\theta_1, \theta_2, \theta_3, \theta_4, \theta_5$	958	199.3

Table 3.1 Calculated thickness of BHTO with different set of angles from Kiessig fringes. From the Bragg's law, $2d\sin\theta = n\lambda$, thickness of film d is calculated for each θ , which corresponds to n^{th} , $n+1^{\text{th}}$, $n+2^{\text{th}}$... peak. Integer n is determined for the minimum standard deviation of the calculated thicknesses. From the smoothing function of subtracted intensity, the 2θ angles of Kiessig fringes are determined to $2\theta_1=43.4748^\circ$, $2\theta_2=43.5216^\circ$, $2\theta_3=43.5716^\circ$, $2\theta_4=43.6164^\circ$, $2\theta_5=43.6660^\circ$ respectively ($\lambda = 0.15406 \text{ nm}$).

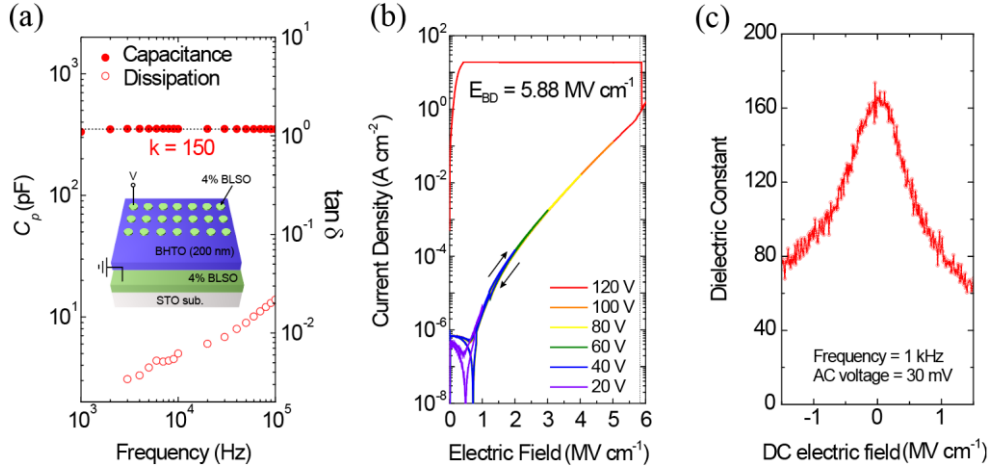


Figure 3.2 Dielectric properties of BHTO. (a) Frequency-dependent capacitance curve of a $\text{BaHf}_{0.6}\text{Ti}_{0.4}\text{O}_3$ metal-insulator-metal device. The inset shows the layer structure of the device. STO, SrTiO_3 . (b) Leakage current density as a function of electric field of the $\text{BaHf}_{0.6}\text{Ti}_{0.4}\text{O}_3$ device in (a). (c) Electric field dependence of dielectric constant measured at 1 kHz with an AC bias of 30 mV.

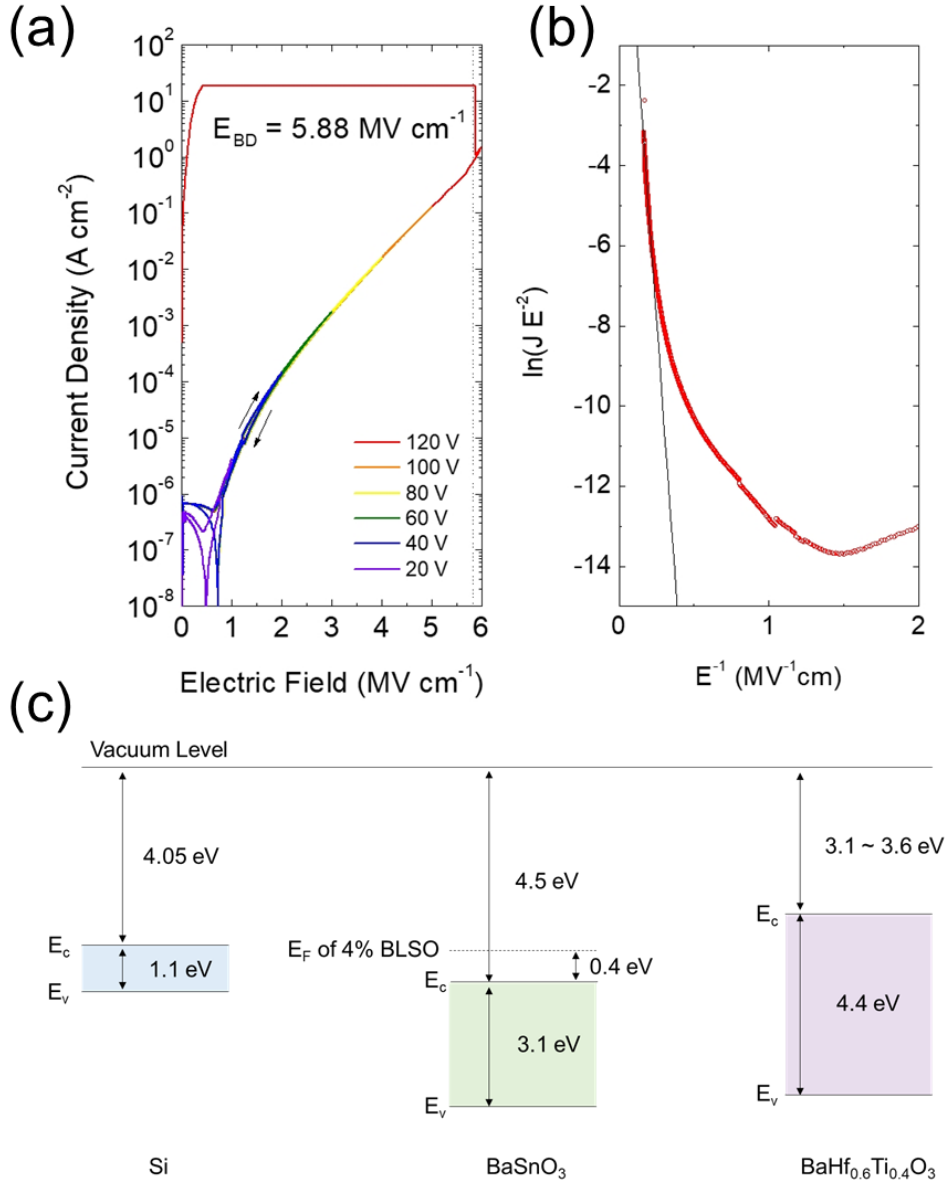


Figure 3.3 Fowler-Nordheim analysis and comparison of band diagrams. (a) J-E characteristic of BHTO capacitor. (b) $\ln(J E^{-2})$ vs E^{-1} curve for Fowler-Nordheim analysis of leakage current using the following relation, $J \propto E^2 \exp\left(\frac{-4\sqrt{2m_{BHTO}^*}\Phi^2}{3ehE}\right)$. The uncertainty in the effective mass of BHTO generates the range of the barrier height from 1.0 eV ($m^* \sim 0.6 m_e$) to 0.5 eV ($m^* \sim 6.0 m_e$). Adding the Fermi level of 0.4 eV above the conduction band minimum, the band offset between the BSO and BHTO is in the range of 0.9~1.4 eV. (c) Comparison of band diagram for Si, BSO, BHTO.

In order to gather statistics of the dielectric properties of $\text{BaHf}_{0.6}\text{Ti}_{0.4}\text{O}_3$, we created 21 capacitors arranged in a 3×7 grid on a single chip. The results of these tests are presented in Figure 3.4. The average dielectric constant of $\text{BaHf}_{0.6}\text{Ti}_{0.4}\text{O}_3$ was calculated to be around 150, based on statistical analysis of the capacitor properties. Most of the dielectric constants measured fell within the range of 145 to 155, which is more than twice the reported value of 65 [6].

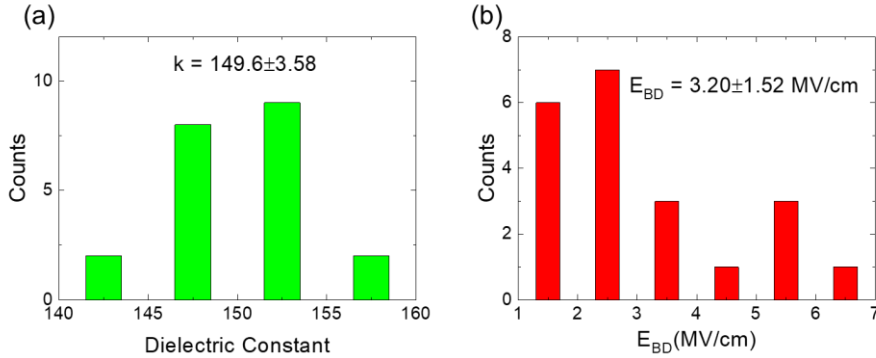


Figure 3.4 Statistical measurement data of 21 MIM devices. (a) Dielectric constant. (b) Breakdown field of $\text{BaHf}_{0.6}\text{Ti}_{0.4}\text{O}_3$. The symbol \pm denotes standard deviations.

Effective medium theories can be used to calculate theoretical dielectric constants [7]. Table 3.2 presents a few exemplary calculations, where the dielectric constants of $\text{BaHf}_{1-x}\text{Ti}_x\text{O}_3$, BHO, and BTO are represented by ϵ_{BHfO} , ϵ_{BHO} , and ϵ_{BTO} , respectively. The volume fractions of BHO and BTO, denoted by f_{BHO} and f_{BTO} , respectively, are set to 0.6 and 0.4. Using classical effective medium theory and the reported dielectric constants of BHO and BTO, which range from 37.8 to 200-600, the effective medium theory produces a range of 56.6 to 61.5 for the dielectric

constants of $\text{BaHf}_{0.6}\text{Ti}_{0.4}\text{O}_3$. These values are significantly lower than our experimental results. Even if we utilize the high dielectric constant of single-crystal BTO, which is approximately 4000, the resulting calculated value of 63.9 is not significantly different. In the Maxwell-Garnett approximation, which proposes the presence of solid nanospheres within a host material, the calculated dielectric constant of BHTO is consistently lower than the experimental values, regardless of the dielectric constant of BTO. This is likely due to the model's limitation, which is only valid when the volume fraction of nanospheres is relatively low (<0.1).

Calculation Model	Formula	ϵ_{BHO}	ϵ_{BTO}	Calculated ϵ_{BHTO}
Effective medium approximation	$\frac{\epsilon_{BHTO} - 1}{\epsilon_{BHTO} + 2} = f_{BHO} \frac{\epsilon_{BHO} - 1}{\epsilon_{BHO} + 2} + f_{BTO} \frac{\epsilon_{BTO} - 1}{\epsilon_{BTO} + 2}$	37.8	200	56.6
			400	60.2
			600	61.5
			4000	63.9
Maxwell-Garnett approximation	$\frac{\epsilon_{BHTO} - \epsilon_{BHO}}{\epsilon_{BHTO} + 2\epsilon_{BHO}} = f_{BTO} \frac{\epsilon_{BTO} - \epsilon_{BHO}}{\epsilon_{BTO} + 2\epsilon_{BHO}}$		200	72.7
			400	87.5
			600	94.4
			4000	110.0
Bruggeman approximation	$f_{BHO} \frac{\epsilon_{BHO} - \epsilon_{BHTO}}{\epsilon_{BHO} + 2\epsilon_{BHTO}} + f_{BTO} \frac{\epsilon_{BTO} - \epsilon_{BHTO}}{\epsilon_{BTO} + 2\epsilon_{BHTO}} = 0$		200	81.5
			400	118.8
			600	150.5
			4000	552.1

Table 3.2 Calculated dielectric constant of BHTO from different kinds of approximations. $f_{BHO}=0.6$ and $f_{BTO}=0.4$ were used.

However, using the Bruggeman approximation, in which host and guest materials are indistinguishable and the system is completely random, the calculated dielectric

constant accurately predicts the experimental dielectric constant of 150 when the dielectric constant of BTO is assumed to be 600.

The breakdown field of $\text{BaHf}_{0.6}\text{Ti}_{0.4}\text{O}_3$ has a statistically averaged value of 3.2 MV cm^{-1} , and its deviation is significantly greater than that of the dielectric constant. This is likely because the dielectric breakdown is more dependent on the local defects in each capacitor. Therefore, in terms of the breakdown field, the maximum measured value, rather than the average, would be a more appropriate representation of the intrinsic dielectric strength. Some capacitors showed a breakdown field exceeding 5.0 MV cm^{-1} . Several representative current density–electric field characteristics are shown in the Figure 3.5. The dielectric properties of $\text{BaHf}_{0.6}\text{Ti}_{0.4}\text{O}_3$ indicate that a maximum field-induced charge density exceeding 10^{14} cm^{-2} can be achieved at 2 MV cm^{-1} , with a corresponding leakage current density of $10^{-4} \text{ A cm}^{-2}$. This means that in a $1\text{-}\mu\text{m}^2$ sized device, the leakage current would be around 10^{-12} A . Despite the DC field dependence of the dielectric, the field-induced charge density still exceeds 10^{14} cm^{-2} .

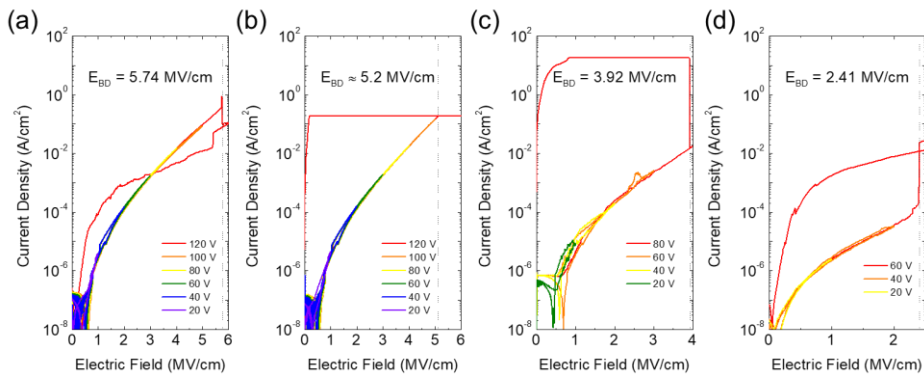


Figure 3.5 I-V characteristics of several $\text{BaHf}_{0.6}\text{Ti}_{0.4}\text{O}_3$ capacitors. The current measurement in (b) is limited by the compliance current, and the E_{BD} is located between 5.11 MV cm^{-1} and 6 MV cm^{-1} . Every measurement is performed for voltage sweep mode.

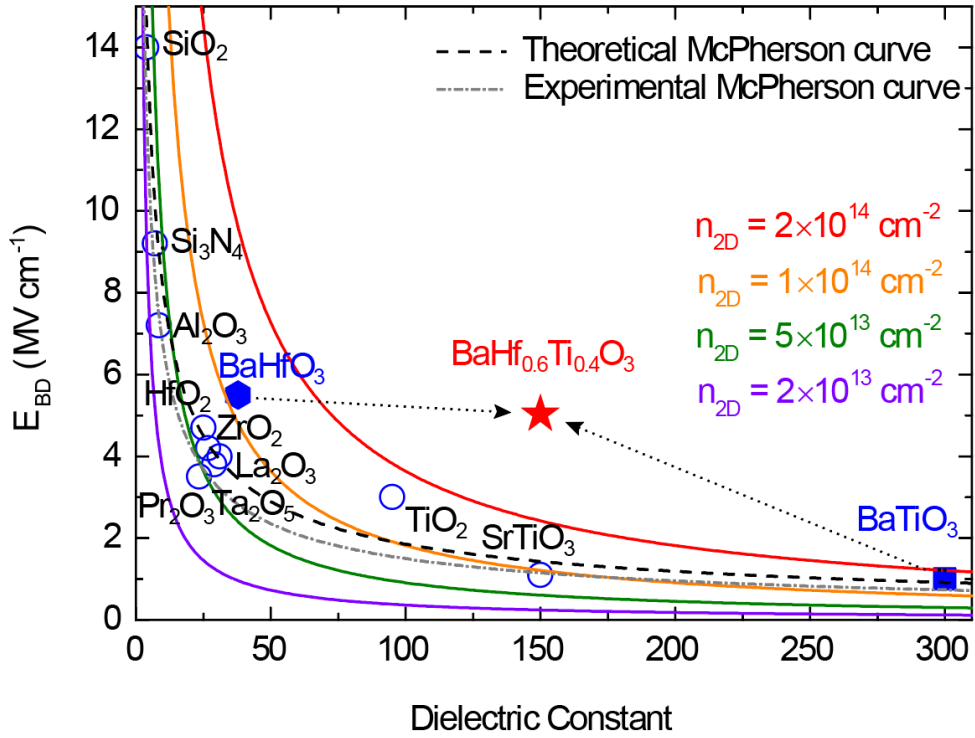


Figure 3.6 Comparison of dielectric constant, breakdown field of dielectric materials including well-known high-k materials. Each colored lines denotes maximum field-induced charge densities. Black dashed lines and gray dashed-dotted lines are theoretical and experimental McPherson dielectric constant–breakdown field relations, respectively.

Figure 3.6 displays a comparison of dielectric materials, their dielectric constants, and breakdown fields, while additional data on various binary and ternary dielectrics can be found in Table 1.1. The figure includes the maximum two-dimensional charge density curve that can be modulated by dielectrics, which is directly proportional to the product of the breakdown field and dielectric constant. Theoretical and experimental curves generated by the McPherson model [8] are also presented, with the equations $E_{BD} = 35.3 (k)^{-0.64}$ and $E_{BD} = 29.9 (k)^{-0.65}$ (for theoretical and experimental, respectively). $\text{BaHf}_{0.6}\text{Ti}_{0.4}\text{O}_3$ dielectric has a dielectric constant of around 150, and its breakdown field is approximately 5 MV cm^{-1} ,

resulting in a maximum field-induced charge density of about $4 \times 10^{14} \text{ cm}^{-2}$. It's important to note that the maximum electric field in devices is typically limited by the leakage current constraint, depending on device geometry. Nevertheless, the values of $\text{BaHf}_{0.6}\text{Ti}_{0.4}\text{O}_3$ are far superior to those of known dielectrics on the McPherson curve, and no other dielectrics have characteristics comparable to $\text{BaHf}_{0.6}\text{Ti}_{0.4}\text{O}_3$.

3.3. Field effect transistors using $\text{BaHf}_{0.6}\text{Ti}_{0.4}\text{O}_3$ for modulation beyond 10^{14} cm^{-2}

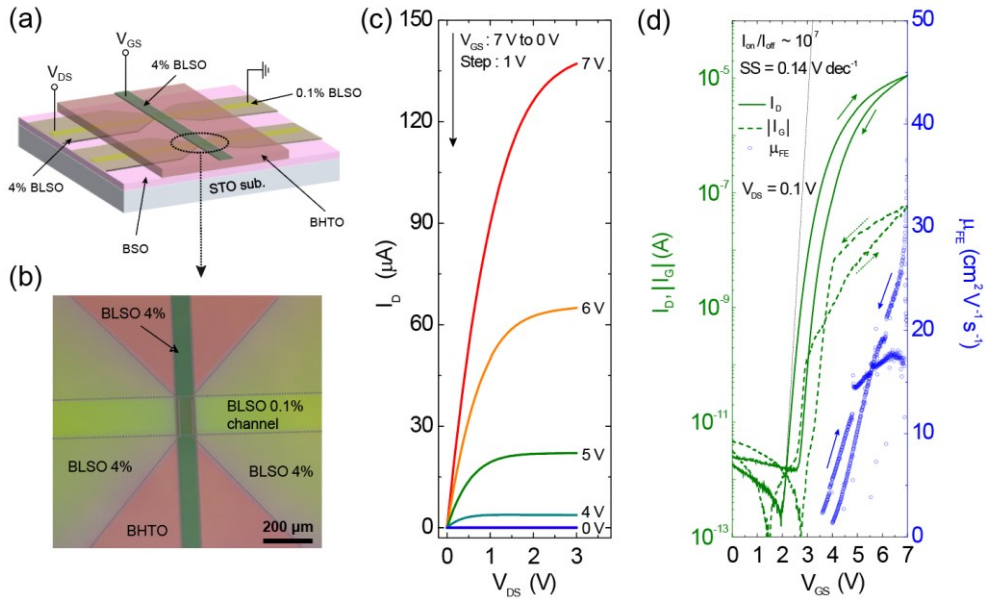


Figure 3.7 FET in an n-type accumulation mode made with 0.1% BLSO channel layer and $\text{BaHf}_{0.6}\text{Ti}_{0.4}\text{O}_3$ gate oxide. (a) Schematic of the device. (b) The top view of the device pictured by an optical microscope. Gray dotted lines are plotted to illustrate each deposited layer. The channel width (W_{ch}) of 0.1% La-doped BaSnO_3 is $140 \mu\text{m}$, and the channel length (L_{ch}) is $60 \mu\text{m}$. (c) The output characteristic of the device. (d) Transfer characteristics of the device. Source-drain current is plotted in a full green line, leakage current is plotted in a dashed green line. Calculated field-effect mobility is shown in blue circle scatter plot. Black dashed line shows maximum subthreshold swing (SS) of the device.

Figure 3.7 displays an n-type accumulation mode FET utilizing BaHf_{0.6}Ti_{0.4}O₃ as the gate oxide. The device's cross-sectional schematic diagram is illustrated in Figure 3.7(a). To decrease the threading dislocation density, a 150-nm-thick BaSnO₃ buffer layer was grown on a SrTiO₃ substrate. Subsequently, a 26-nm-thick 0.1% La-doped BaSnO₃ channel layer was grown on top of it using a micromachined silicon stencil mask patterned as a line. A 4% La-doped BaSnO₃ was grown on it via a stainless-steel mask as the source and the drain contacts, which defines the channel length. Lastly, using other Si masks, a 100-nm-thick BaHf_{0.6}Ti_{0.4}O₃ gate oxide layer and 4% La-doped BaSnO₃ gate electrode were grown. The device's microscope image is shown in Figure 3.7(b). The channel width (W_{ch}) of 0.1% La-doped BaSnO₃ is 140 μm , and the channel length (L_{ch}) is 60 μm . Figure 3.8 displays more detailed geometry of the device. The output characteristics of the device are presented in Figure 3.7(c). The device was operated at a source-drain voltage (V_{DS}) of up to 3 V, while the gate voltage (V_{GS}) was varied from 7 to 0 V with the interval of 1 V. The drain current (I_D) is proportional to the V_{DS} at low V_{DS} , and as V_{DS} increases, I_D becomes saturated. The transfer characteristics of the device are shown in Figure 3.7(d), where the gate leakage current (I_G) and I_D were measured at $V_{DS} = 0.1$ V, while V_{GS} was swept from 0 to 7 V. The I_{on}/I_{off} ratio is approximately 10^7 . The subthreshold swing value was calculated using the relation $S = [\partial \log(I_D) / \partial V_{GS}]^{-1}$ as 0.14 V decade⁻¹. The device's field-effect mobility (μ_{FE}) was calculated using the relation for the linear region

$$\mu_{FE,lin} = \frac{L}{WC_{ox}V_{DS}} \left(\frac{\partial I_D}{\partial V_{GS}} \right) = \frac{Lt}{W\kappa\epsilon_0V_{DS}} \left(\frac{\partial I_D}{\partial V_{GS}} \right) \quad (3.1)$$

where L , W , C_{ox} , t , and ϵ_0 are the channel length, the channel width, the

capacitance per unit area of the $\text{BaHf}_{0.6}\text{Ti}_{0.4}\text{O}_3$ layer, the thickness of the $\text{BaHf}_{0.6}\text{Ti}_{0.4}\text{O}_3$ layer, and the permittivity of the vacuum, respectively. The saturation region ($V_{\text{DS}} = 5 \text{ V}$) linear plot of $\sqrt{I_{\text{D}}}$ versus V_{GS} in Figure 3.9 is used to determine the threshold voltage (V_{T}) of the device, which is found to be 3.6 and 4.0 V for the increasing and decreasing V_{GS} , respectively. The maximum field-effect mobility (μ_{FE}) is calculated to be about $30 \text{ cm}^2 \text{ V}^{-1} \text{ s}^{-1}$, using the average C_{ox} at low bias ($k \sim 120$ near 0.5 MV cm^{-1}). Compared to the FET with BHO gate oxide, which has a different La doping concentration, the V_{GS} required to modulate the current amplification of 10^7 (+3 to +7 V) is smaller (-7 to +18 V in the case of BHO [9]), which is attributed to the higher dielectric constant of $\text{BaHf}_{0.6}\text{Ti}_{0.4}\text{O}_3$ than BHO. Additionally, the subthreshold swing value is smaller than that of the BHO device, which is $0.8 \text{ V decade}^{-1}$.

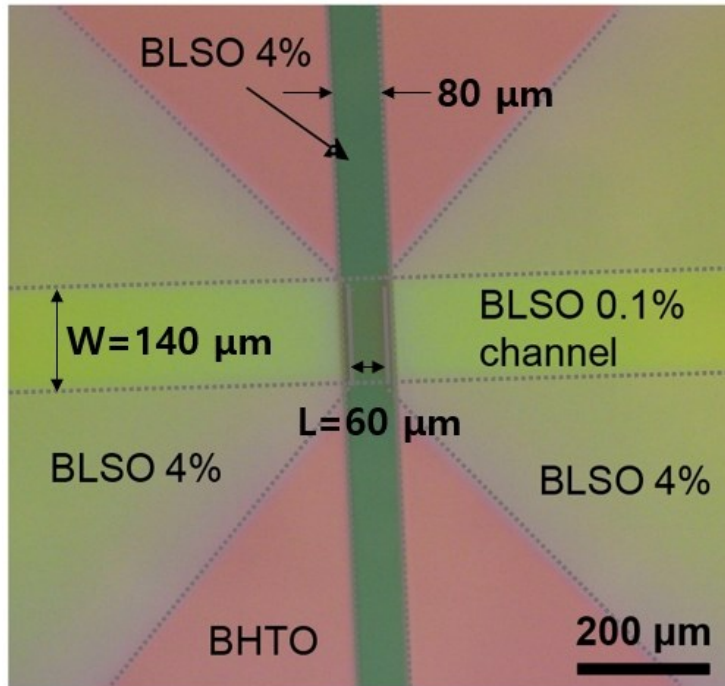


Figure 3.8 Detailed geometry for the channel length and width and the gate length for the accumulation mode FET.

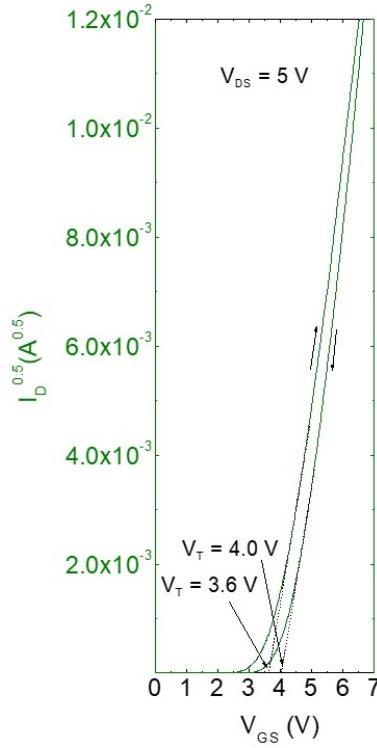


Figure 3.9 $\sqrt{I_D}$ vs V_{GS} plot in linear scale for determining threshold voltage (V_T) of device.

Efforts have been made to modulate the carrier density beyond 10^{14} cm^{-2} using solid-state oxides with high dielectric constant, such as BaTiO_3 and SrTiO_3 [10-12]. A recent report described depletion mode field effect transistors using BaTiO_3 as the gate dielectric [10], but the device's capacity to modulate charge density was limited to only $5.7 \times 10^{13} \text{ cm}^{-2}$. At $V_{GS} = -6 \text{ V}$, the off-state gate leakage current was 11.0 mA mm^{-1} , equivalent to $1.72 \times 10^3 \text{ A cm}^{-2}$ at -3 MV cm^{-1} , which is too high for practical applications. Devices based on SrTiO_3 were able to modulate carrier density above $1 \times 10^{14} \text{ cm}^{-2}$ [11,12]. One type of device, $\text{SrTiO}_3/\text{GdTiO}_3$ heterostructure field effect transistors, could modulate the interfacial two-dimensional electron gas (2DEG) by $1.1 \times 10^{14} \text{ cm}^{-2}$ [11]. However, this device was

not able to fully pinch off the channel. Another device, the SrTiO₃-based MESFET, could modulate the charge density to $1.62 \times 10^{14} \text{ cm}^{-2}$ [12]. Nevertheless, this device also exhibited high off-state leakage current of about 0.1 mA mm^{-1} at 1.875 MV cm^{-1} , which is also too high and probably responsible for the low on/off ratio of only 10^3 , although the exact dimensions of the device are not disclosed.

To provide a direct demonstration of charge modulation exceeding 10^{14} cm^{-2} , we produced depletion mode field effect transistors (FETs) using a 33 nm thick channel layer composed of 0.4% La-doped BaSnO₃. The thickness of the 0.4% BLSO layer was verified using an AFM thickness profile, shown in Figure 3.10.

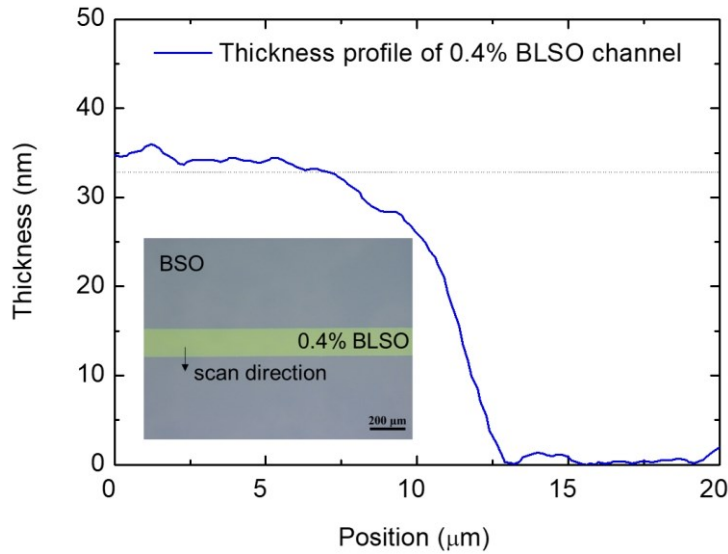


Figure 3.10 Thickness profile of 0.4% BLSO channel by AFM measurement.

A separate Hall measurement presented in Figure 3.11 revealed that 20 nm thick films composed of 0.4% La-doped BaSnO₃ had a 2D carrier density of $7.03 \times 10^{13} \text{ cm}^{-2}$. Therefore, we can estimate that the 33 nm thick channel used in the FETs had

a 2D carrier density of approximately $1.16 \times 10^{14} \text{ cm}^{-2}$.

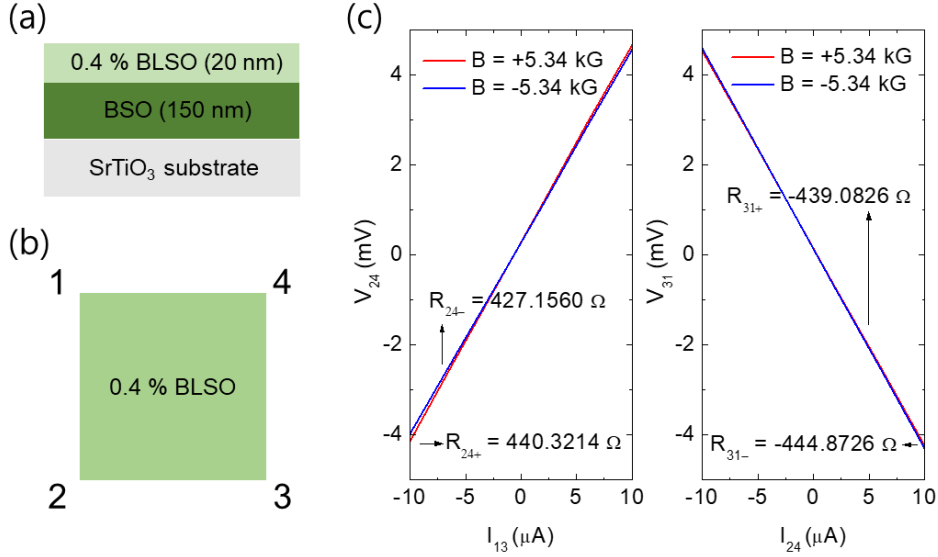


Figure 3.11 Hall measurement of a 20 nm thick 0.4% La-doped BSO film. (A) Schematic of the film. (B) Geometry of 4-probe Hall measurement. (C) Hall resistance of both diagonals. Hall resistance and voltage was determined by averaging both diagonals with magnetic field of $\pm 5.34 \text{ kG}$. 2-dimensional carrier concentration was calculated by following equation.

$n_{2D} = \frac{IB}{eV_H} = \frac{B}{eR_H}$ (I: current, B: magnetic field, e: charge of electron, V_H : Hall voltage, R_H : Hall resistance)

$$R_H = \frac{R_{24+} - R_{24-} + R_{31+} - R_{31-}}{4} = 4.74 \Omega,$$

$$n_{2D} = \frac{0.534 \text{ T}}{1.6 \times 10^{-19} \text{ C} \times 4.74 \Omega} = 7.03 \times 10^{17} \text{ m}^{-2} = 7.03 \times 10^{13} \text{ cm}^{-2}.$$

Growth rate of 0.4% BLSO was determined by measuring the thickness of 7000 laser shots deposited film as 156 nm. The 20 nm thick film used for Hall measurement was deposited by 897 laser shots.

The corresponding mobility value calculated from the sheet resistance $3,036 \Omega$ of the film is $29.23 \text{ cm}^2/\text{V}\cdot\text{s}$.

Figure 3.12(a) displays a schematic of the device's cross-section. To establish the channel width, a $140 \mu\text{m}$ silicon stencil mask was employed. Following the deposition of the buffer and channel layers, a 4% La-doped BaSnO_3 channel contact layer was added using a stainless-steel mask to establish the average 130

μm channel length. Next, a 200 nm thick $\text{BaHf}_{0.6}\text{Ti}_{0.4}\text{O}_3$ gate oxide was deposited using a silicon stencil mask. To create the gate length of 80 μm , a 4% La-doped BaSnO_3 gate electrode layer was deposited using a silicon stencil mask. The detailed geometry of the device is shown in Figure 3.13. Figure 3.12(b) displays a microscope image of the device, while its output characteristic is shown in Figure 3.12(c). The device's source-drain voltage (V_{DS}) was applied up to 25 V, and the gate voltage (V_{GS}) varied from 0 to -40 V with a 5 V interval. At low V_{DS} , the drain current (I_{D}) is linearly proportional to the V_{DS} , and as V_{DS} increases, I_{D} becomes saturated, which is a typical characteristic of an n-type FET. The transfer characteristics of the device are shown in Figure 3.12(d). Gate leakage current (I_{G})

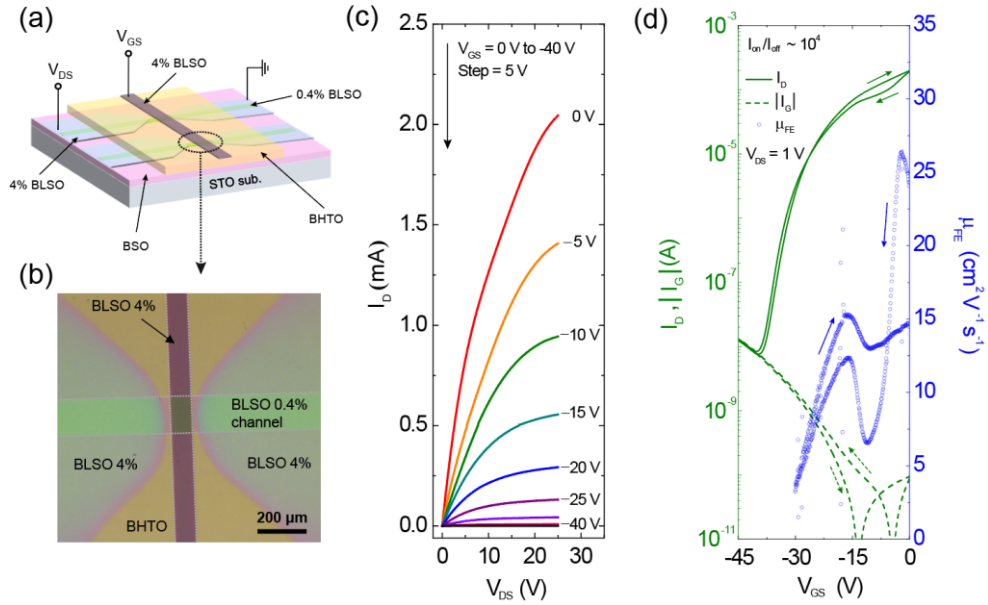


Figure 3.12 FET in an n-type depletion mode made with 0.4 % La-doped BSO channel layer and $\text{Hf}_{0.6}\text{Ti}_{0.4}\text{O}_3$ gate oxide. (a) Schematic of the device. (b) The top view of the device pictured by an optical microscope. Gray dotted lines are plotted to illustrate each deposited layer. The channel width (W_{ch}) of 0.4% La-doped BaSnO_3 is 140 μm , and the average channel length (L_{ch}) is 130 μm . (c) The output characteristic of the device. (d) Transfer characteristics of the device. Source-drain current is plotted in a full green line, leakage current is plotted in a dashed green line. Calculated field-effect mobility is shown in blue circle scatter plot.

and I_D was measured at $V_{DS} = 1$ V while V_{GS} was swept from 0 to -45 V. I_{on}/I_{off} ratio is about 10^4 , limited by relatively high off-state I_D due to the high I_G . Field effect mobility (μ_{FE}) of the device was calculated using relation (3.1). The C_{ox} value in the device was determined by measurement, as depicted in Figure 3.14, and was utilized in the calculation. The highest value of field effect mobility (μ_{FE}) was found to be approximately $15\text{-}25 \text{ cm}^2 \text{ V}^{-1} \text{ s}^{-1}$. The channel of 0.4% La-doped BaSnO₃ was depleted to the point where the drain current (I_D) was limited by the gate leakage current (I_G). Based on the leakage current density of $10^{-4} \text{ A cm}^{-2}$ at 2 MV cm^{-1} in Fig. 3.2, it can be predicted that if the device is scaled down to a $0.1 \text{ }\mu\text{m}$ length and $10 \text{ }\mu\text{m}$ width channel, the leakage current will decrease to 10^{-12} A at 2 MV cm^{-1} . This would fulfill the requirements of field effect devices that need an on-current of greater than $1 \text{ mA }\mu\text{m}^{-1}$ and off-current of 10^{-12} A . Direct modulation of carrier density over 10^{14} cm^{-2} was realized using solid-state gate oxide, which has not been realized to date. The C-V measurement of the device in Fig. 3.14 confirms the modulation of $1.07 \times 10^{14} \text{ cm}^{-2}$.

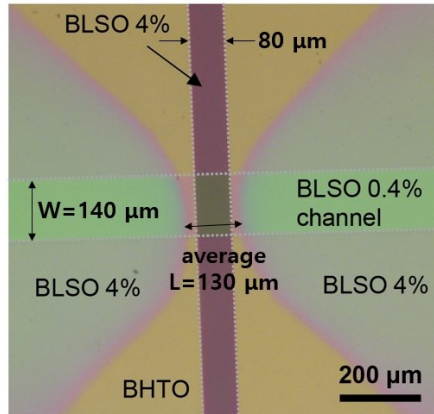


Figure 3.13 Detailed geometry for the channel width and length and the gate length of the depletion mode FET.

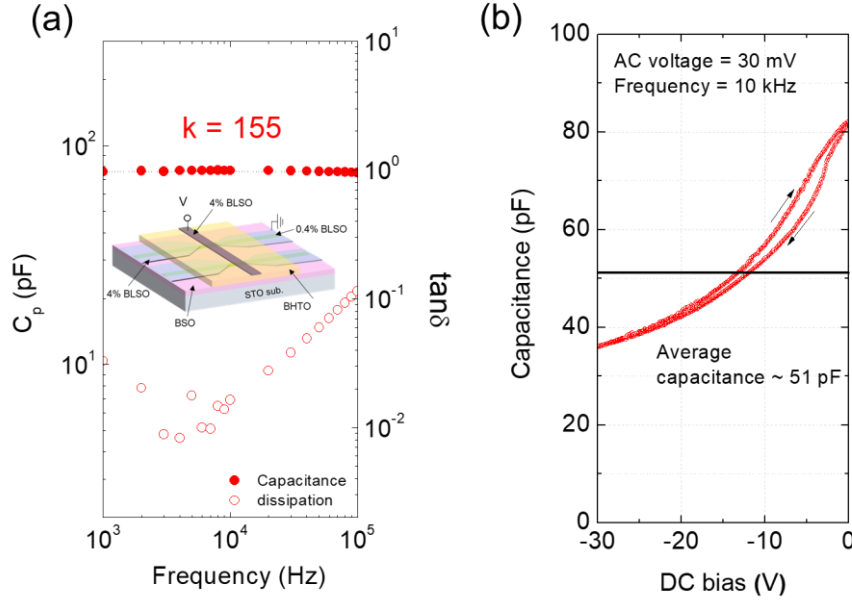


Figure 3.14 Capacitance of a BHTO depletion mode FET with 0.4% BLSO channel (A) Capacitance-frequency curve of depletion mode FET with zero dc bias and 30 mV ac bias. (B) C-V curve of depletion mode FET. Using the average capacitance of 51 pF over the gate bias range (–38 to 0 V), the calculated 2D density is $1.07 \times 10^{14} \text{ cm}^{-2}$, taking into account the area of $140 \text{ } \mu\text{m} \times 80 \text{ } \mu\text{m}$. The DC bias during the C-V measurement was stopped at -30 V due to the limit by the measurement equipment (Keithley 4200).

3.4. Structural properties of $\text{BaHf}_{0.6}\text{Ti}_{0.4}\text{O}_3$

3.4.1 Scanning Transmission Electron Microscope (STEM) of $\text{BaHf}_{0.6}\text{Ti}_{0.4}\text{O}_3$

To explore the structural properties, measurements were conducted using a Scanning Transmission Electron Microscope (STEM) by Dr. Myoungho Jeong in Samsung Advanced Institute of Technology (SAIT). The sample of the BHTO films, oriented in the [100] direction, for cross-sectional imaging were prepared by the Ga ion beam milling using focused ion beam (FIB, Thermofisher Scientific,

Helios5 HX) at an acceleration voltage of 15kV. A further 1kV Ga ion beam milling was conducted to eliminate the surface damages of the sample. Scanning Transmission Electron Microscope (STEM) and Electron Energy Loss Spectroscopy (EELS) analysis were performed on an aberration-corrected STEM (ThermoFisher Scientific, Titan_Cubed 60-300) equipped with EELS (Gatan, Quantum ERS 966), operating at 300kV with a semi-convergence angle of 26.5mrad. The High Angle and Low Angle Annular Dark Field (HAADF/LAADF) STEM images were acquired with detector angle ranges 40-200 and 25-47 mrad, respectively. EELS-SI (spectrum imaging) were recorded with the energy range of 200-2248 eV to detect the Ti L_{2,3}, O-K, Ba M_{4,5}, and Hf M_{4,5} with an energy resolution of ~0.9 eV. The dwell time per pixel and dispersion were 0.02 sec and 1eV/ch, respectively.

Figure 3.15(a) displays a high-angle annular dark field-scanning transmission electron microscope (HAADF-STEM) image of BaHf_{0.6}Ti_{0.4}O₃ at different magnifications, while Figure 3.15(b) shows a low-angle annular dark field-scanning transmission electron microscope (LAADF-STEM) image of the same area of the film. In the LAADF-STEM image, which is known to be more sensitive to local strain [13], atomic contrast is clearly visible, unlike the HAADF-STEM image of BaHf_{0.6}Ti_{0.4}O₃. The bright regions in the LAADF-STEM image are thought to correspond to areas rich in titanium. To verify the stoichiometric modulation, we conducted electron energy loss spectroscopy (EELS) on the film to distinguish the atomic arrangement of BaHf_{0.6}Ti_{0.4}O₃, as demonstrated in Figure 3.16(a). By mapping Ti atom, we found that the arrangement of Ti atoms is comparable to the LAADF-STEM image, indicating clustering of Ti-rich regions at

a scale of 2 nm. The distribution of Hf in the film complements that of Ti because when the mapping images of Ti and Hf are superimposed, the resulting image is very similar to that of Ba, which is evenly distributed throughout. EELS line scan profiles, shown in Figure 3.16(b) and (c), confirm the chemical heterogeneity of Hf and Ti atoms. As anticipated in a chemically modulated system, the intensities of the two atoms in the line scan profiles are complementary to each other.

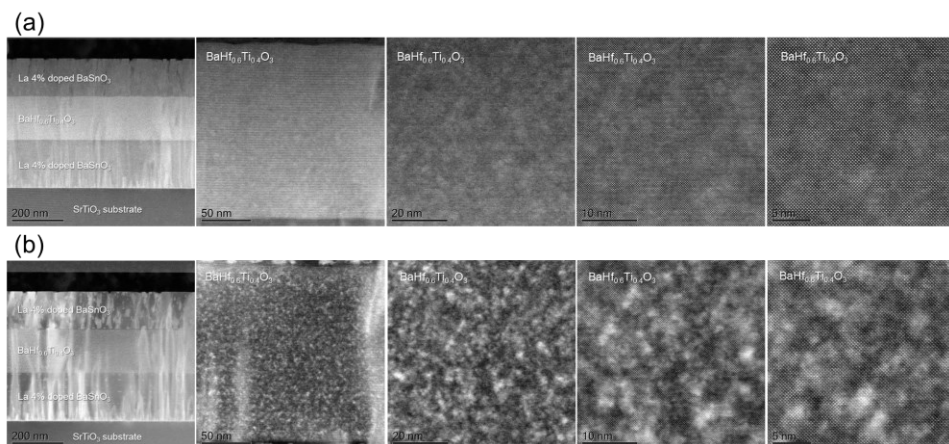


Figure 3.15 STEM image of $\text{BaHf}_{0.6}\text{Ti}_{0.4}\text{O}_3$. (a) HAADF-STEM of various magnification scales. (b) LAADF-STEM of various magnification scales.

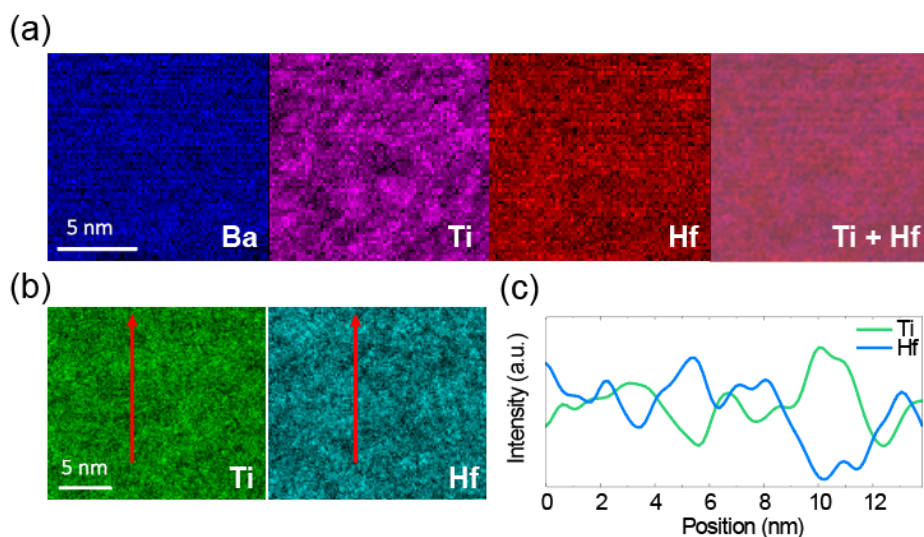


Figure 3.16 EELS of BHTO. (a) EELS element mapping image of $\text{BaHf}_{0.6}\text{Ti}_{0.4}\text{O}_3$. (b) Region of EELS line scan. Red arrows denote scan directions. (c) Line profile of Ti and Hf elements.

3.4.2 High-resolution X-ray diffraction (HRXRD) of BaHf_{0.6}Ti_{0.4}O₃

To further confirm the chemical heterogeneity of Hf and Ti atoms, we measured structural property of BaHf_{0.6}Ti_{0.4}O₃ by x-ray diffraction measurement. The high quality of the films was confirmed by D8 Discover high-resolution diffractometer (Bruker), operated at 40 kV and 60 mA with Cu K α ($\lambda = 1.5406$ Å) radiation. The first step in the process involved growing a degenerately doped layer of 4% La-doped BaSnO₃ as the bottom electrode on SrTiO₃ substrates. A layer of BaHf_{0.6}Ti_{0.4}O₃, approximately 200 nm thick, was then epitaxially grown on top of it.

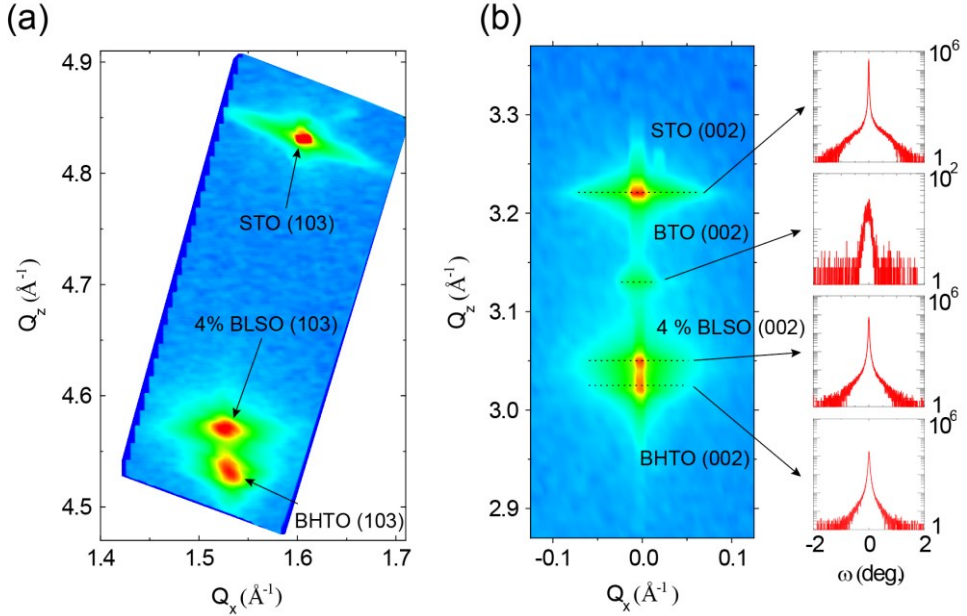


Figure 3.17 RSM of BHTO. (a) Reciprocal space mapping (RSM) of BaHf_{0.6}Ti_{0.4}O₃ (103) peak. (b) (002) peaks and corresponding rocking curves. Black dotted lines are rocking curve scan regions. Detailed rocking curves and full width half maximums (FWHM) are presented in Figure 3.18.

Reciprocal space mapping (RSM) measurements were conducted on the (103) and (002) peaks of the BaHf_{0.6}Ti_{0.4}O₃ layer, as illustrated in Figure 3.17. The (103) peak of BaHf_{0.6}Ti_{0.4}O₃, depicted in Figure 3.17(a), has in-plane and out-of-plane lattice

parameters of 4.096 Å and 4.158 Å, respectively. Although the in-plane lattice value is close to the expected value based on the cubic BaHfO₃ bulk lattice parameter of $a = 4.171$ Å and the tetragonal BaTiO₃ bulk lattice parameters of $a = 4.000$ Å and $c = 4.027$ Å, it does not appear to be pinned with that of the underlying La-doped BaSnO₃. The in-plane and out-of-plane lattice parameters indicate that the BaHf_{0.6}Ti_{0.4}O₃ film is grown as tetragonal structure, which can contribute to the large dielectric constant. The (002) peaks RSM, illustrated in Figure 3.17(b), revealed a small, isolated peak of BaTiO₃ with a corresponding out-of-plane lattice parameter of $c = 4.013$ Å. This provides direct evidence of clustering in the Ti-rich region. However, no peaks of BaHfO₃ were detected. Figure 3.18 displays detailed rocking curves of the film. The full width half maximums (FWHMs) for the 4% BLSO layer and the BaHf_{0.6}Ti_{0.4}O₃ layer are 0.028 and 0.036, respectively, which is close to that of the SrTiO₃ single crystal substrate (0.023). However, the FWHM of the BTO peak is 0.286. Thus, only the

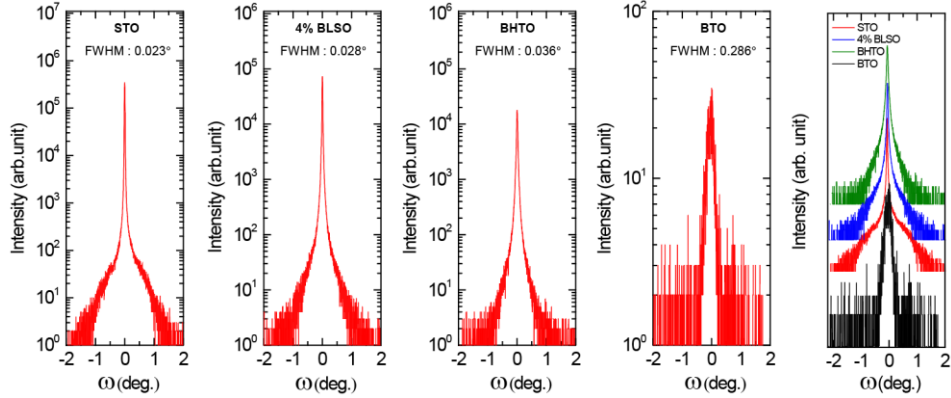


Figure 3.18 Rocking curves of BaHf_{0.6}Ti_{0.4}O₃ capacitor from XRD measurements.

BTO peak has much broader FWHM, not coherent with other peaks, which indicates nano-scale clustering of the material. This can explain why the in-plane lattice constant is not pinned, despite the average lattice constants of La-doped

BaSnO₃ and BaHf_{0.6}Ti_{0.4}O₃ having a mismatch of less than 0.5%.

3.5 Optical bandgap of BaHf_{0.6}Ti_{0.4}O₃

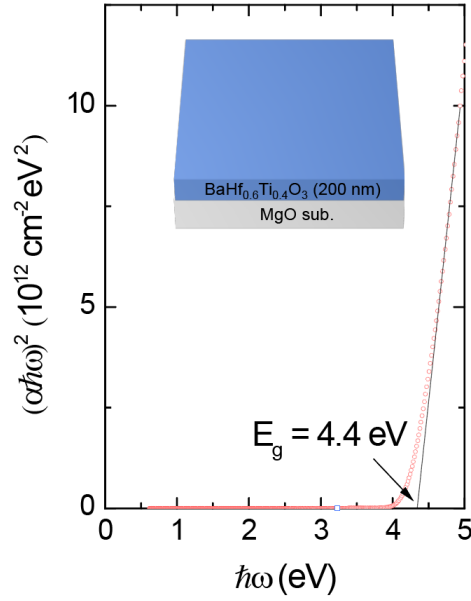


Figure 3.19 Optical band gap of BaHf_{0.6}Ti_{0.4}O₃. Bandgap fitting is performed assuming direct bandgap.

We measured the optical absorption of samples by using a grating spectrometer (Cary 5000, Bruker) over 200 - 2000 nm (0.6 - 6.2 eV) at Jae Hoon Kim's lab in Yonsei University. The spectrometer has a quartz iodine (QI) lamp light source for 2000 - 350 nm and a deuterium UV lamp light source for below 350 nm. Samples are mounted on a holder with a 3 mm diameter hole. Absorbance is calculated as the minus logarithm of the transmittance and absorption coefficient α is calculated by accounting for the sample thickness. About 200 nm thick BaHf_{0.6}Ti_{0.4}O₃ layer was grown on MgO substrate ($E_g \sim 8 \text{ eV}$) to prevent absorption by the substrate.

We removed the substrate absorption by measuring MgO substrate's optical absorption separately and subtracting absorbance of the two samples. From the optical absorption measurement, we plotted the Tauc's plot of $(\alpha\hbar\omega)^2$ vs $(\hbar\omega)$, where α denotes absorption coefficient, assuming a direct bandgap. The optical bandgap of BaHf_{0.6}Ti_{0.4}O₃, which is the minimum energy required for an electron to transition from the valence band to the conduction band, was determined to be 4.4 eV through optical absorption measurement as shown in Figure 3.19. This value suggests that the material could sustain a dielectric breakdown field of 5.0 MV cm⁻¹ if the breakdown field is indeed limited by the bandgap, as stated in [14]. However, defect states that function as leakage current paths usually exist within the bandgap in practical cases, and they decrease the breakdown field.

3.6. Percolation path formation model

The reason behind the BaHf_{0.6}Ti_{0.4}O₃ dielectric possessing a high dielectric constant, high breakdown field, and a moderately high bandgap can be explained as follows. The combination of a high dielectric strength background material rich in Hf, and the inclusion of high dielectric constant material rich in Ti, results in a material with a large average polarization when an external electric field is applied, which leads to a high dielectric constant. Additionally, the high dielectric strength background prevents the formation of a conductive percolation path, which in turn reduces the leakage current and increases the breakdown field. Therefore, by properly combining materials with high dielectric strength and high dielectric constant, both electrical properties can be optimized as illustrated in Figure 3.20.

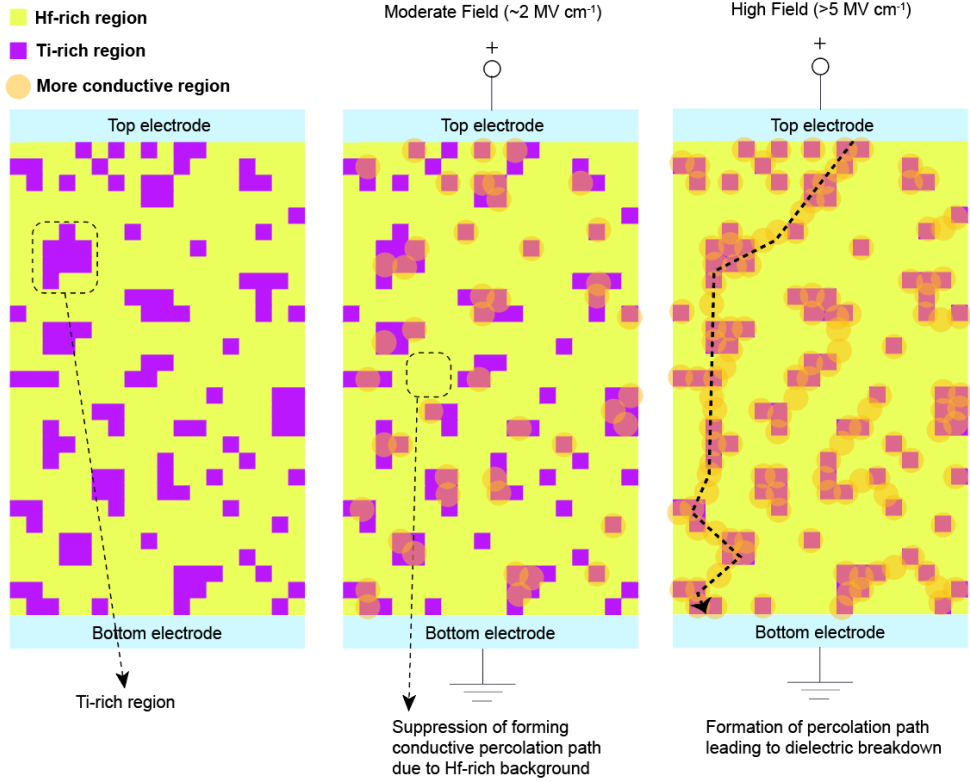


Figure 3.20 Percolation path formation model in heterogeneous $\text{BaHf}_{0.6}\text{Ti}_{0.4}\text{O}_3$ system. In Ti-rich regions, defects are more easily generated compared to Hf-rich regions when electric field is applied, forming the conductive regions. Continuous overlap of conductive region results in formation of a percolating path, finally leading to a large leakage current and the dielectric breakdown which involves irreversible damage to the dielectric layer.

3.7. Conclusion

We conducted research on $\text{BaHf}_{0.6}\text{Ti}_{0.4}\text{O}_3$, which is a combination of a high dielectric strength material and a material with a high dielectric constant, to investigate its dielectric properties. Our findings showed that carrier density exceeding 10^{14} cm^{-2} can be controlled using $\text{BaHf}_{0.6}\text{Ti}_{0.4}\text{O}_3$ dielectric. The key factor in achieving excellent dielectric properties lies in the nanometer-scale stoichiometric modulation of the high dielectric strength background material and

the high dielectric constant material inclusion. We demonstrate the n-type accumulation mode and n-type depletion mode FETs using $\text{BaHf}_{0.6}\text{Ti}_{0.4}\text{O}_3$ gate oxide with excellent FET characteristics, which has been unattainable via other conventional dielectrics.

References

- [1] H. J. Kim, U. Kim, H. M. Kim, T. H. Kim, H. S. Mun, B. G. Jeon, K. T. Hong, W. J. Lee, C. Ju, K. H. Kim, K. Char, *Appl. Phys. Express* **5**, 061102 (2012).
- [2] S. Halder, T. Schneller, R. Waser, S. B. Majumder, *Thin Solid Films* **516**, 4970–4976 (2008).
- [3] K. Abe, S. Komatsu, *Jpn. J. Appl. Phys.* **32**, 4186–4189 (1993).
- [4] P. A. Fleury, J. M. Worlock, *Phys. Rev.* **174**, 613–623 (1968).
- [5] I. A. Akimov, A. A. Sirenko, A. M. Clark, J.-H. Hao, X. X. Xi, *Phys. Rev. Lett.* **84**, 4625–4628 (2000).
- [6] G. Lupina, O. Seifarth, G. Kozlowski, P. Dudek, J. Dabrowski, G. Lippert, H.-J. Mussig, *Microelectron. Eng.* **86**, 1842–1844 (2009).
- [7] V. Lucarini, J. J. Saarinen, K.-E. Peiponen, E. M. Vartianinen, in *Kramer-Kronig Relations in Optical Materials Research* (Springer, 2005), pp. 11–26.
- [8] J. McPherson, J. Kim, A. Shanware, H. Mogul, J. Rodriguez, *IEEE Dig. Int. Electron Devices Meet.*, 633–636 (2002).
- [9] Y. M. Kim, C. Park, T. Ha, U. Kim, N. Kim, J. Shin, Y. Kim, J. Yu, J. H. Kim, K. Char, *APL Mater.* **5**, 016104 (2017).
- [10] J. Cheng, C. Wang, C. Freeze, O. Shoron, N. Combs, H. Yang, N. K. Kalarickal, Z. Xia, S. Stemmer, S. Rajan, W. Lu, *IEEE Electron Device Lett.* **41**, 621–624 (2020).
- [11] M. Boucherit, O. Shoron, C. A. Jackson, T. A. Cain, M. L. C. Buffon, C. Polchinski, S. Stemmer, S. Rajan, *Appl. Phys. Lett.* **104**, 102904 (2014).
- [12] A. Verma, S. Raghavan, S. Stemmer, D. Jena, *Appl. Phys. Lett.* **105**, 113512 (2014).
- [13] D. A. Muller, N. Nakagawa, A. Ohtomo, J. L. Grazul, H. Y. Hwang, *Nature* **430**, 657–661 (2004).
- [14] M. Higashiwaki, K. Sasaki, A. Kuramata, T. Masui, S. Yamakoshi, *Appl. Phys. Lett.* **100**, 013504 (2012).

Chapter 4. Size effect of BaHf_{0.6}Ti_{0.4}O₃ (BHTO)

4.1. Research background

The well-known issue with high-k dielectrics is their dielectric constant decreasing as the dielectric thickness reduces. This occurrence has been observed in various high-k dielectrics such as Pb(Zr,Ti)O₃ (PZT) [1,2] and (Ba,Sr)TiO₃ (BST) [3]. This is so-called “size effect of dielectric”. The cause of this phenomenon is related to the interfacial capacitance with low permittivity generated between the dielectric and electrodes as illustrated in Figure 4.1, although the origin of this will be addressed later. If the interfacial layer is formed between dielectric and electrodes, then the measured capacitance can be expressed as

$$\frac{1}{C_{measured}} = \frac{1}{C_{interfacial}} + \frac{1}{C_{bulk}}. \quad (4.1)$$

If we assume that the thickness and dielectric constant of interfacial layer are independent of dielectric thickness, that is $C_{interfacial}^{-1}$ is constant, the measured dielectric constant is decreased when the dielectric thickness decreases. From the $C_{measured}^{-1}$ vs dielectric thickness plot, the y-intercept is the $C_{interfacial}^{-1}$ and the slope is related to the bulk dielectric constant.

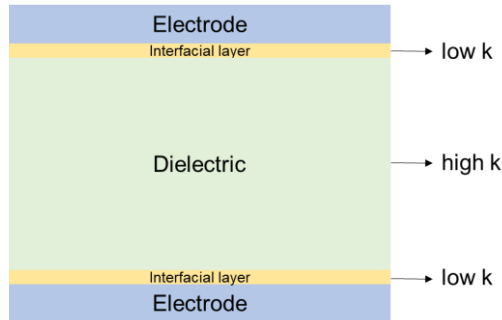


Figure 4.1 Interfacial low-k capacitance model between dielectric and electrodes.

4.2. Origins of size effect

The origin of size effect is investigated by many researchers for several decades. Nevertheless, there is still intense debate regarding the source or cause of this phenomenon. L. J. Sinnamon et al. argued that the size effect is due to growth induced defects, strains, and grain boundaries according to their experimental findings [4]. However, Li et al.'s experimental and theoretical results indicated that even in high-quality interfaces with extremely low defect density, there exist interfacial layers [5]. Their findings showed that there was no interdiffusion between BTO and Pt, nor oxidation of Pt. In C. Zhou and M. Newns' study on SrTiO₃ dielectric film, they discovered the existence of an inherent dead layer on the surface [6]. This layer greatly decreases the effective dielectric constant from their Thomas theory study. Through the application of ab initio calculations, Stengel and Spaldin verified the presence of a layer with low permittivity in nanoscale capacitors made of SrRuO₃/SrTiO₃/SrRuO₃ [7]. Based on their theoretical findings, it appears that the impact of the dead layer is a characteristic that is inherent and inevitable in the interface between dielectric and metal. They argued that the incomplete screening at the electrode is the origin of interfacial capacitance, which is intrinsic effect. However, in experiments, so called size-effect-free dielectric is reported. For instance, Kim et al. reported that there is no interfacial capacitance observed in ultrathin SrRuO₃/BaTiO₃/SrRuO₃ ferroelectric capacitors [8]. Also, in c-axis-oriented bismuth layer-structured dielectric, which can be expressed as (Bi₂O₂)²⁺(A_{m-1}B_mO_{3m+1})²⁻, the dielectric constants are independent of film thickness, indicating that there is no size effect [9,10]. L.-W. Chang et al. demonstrated that an inherent interfacial layer is present even in single

crystal lamellae of SrTiO_3 capacitors with Pt electrodes, while it does not exist in that of BaTiO_3 capacitors with Pt electrode even in films as thin as ~ 75 nm [11]. Thus, it appears that there is a contradiction between the results obtained from the theoretical and experimental investigations. Moreover, there are instances where the outcomes of experiments performed by various groups differ, even when utilizing the same combination of electrode and dielectric materials for the capacitor structure. Stengel. et al. found that the interfacial layer is intrinsic effect, but specific combination of electrode and dielectric materials can minimize the effect by local density approximation of density-functional theory [12]. Furthermore, as weaker as the bonding between electrode and dielectric materials, interfacial layer effect is diminished, because ionic displacement at the interface affects dielectric response. They also found that termination surface is related to the interfacial capacitance. Q. Yang et al. also showed that polarization behavior is strongly dependent on the termination layer of perovskite oxide at the interface [13]. Moreover, the insertion of a suitable buffer layer between the ferroelectric and electrodes would remove the effect of the interfacial layer, according to their calculations. Despite numerous investigations on the interfacial layer, there is still a deficiency in possessing a comprehensive and profound comprehension of this issue.

As stated previously, there are a few systems in which dielectrics that are free from the size effect have been reported. First, the layered perovskite with Aurivillius phase is one of the size-effect-free dielectrics such as $\text{SrBi}_4\text{Ti}_4\text{O}_{15}$, $\text{SrBi}_2\text{Ta}_2\text{O}_9$ [9,10]. In these kinds of material, the pseudo-perovskite block is incorporated between Bi_2O_2 layers, forming van der Waals bonding between the

Bi_2O_2 layers and pseudo-perovskite block. The other system is the perovskite nanosheets exfoliated from Dion-Jacobson layered perovskites such as $\text{Ca}_2\text{Nb}_3\text{O}_{10}$, $\text{Sr}_2\text{Nb}_3\text{O}_{10}$ [14-17]. In this case, the van der Waals bonding is also formed between the perovskite nanosheets and electrodes, which is thought to be relatively weak bonding. What is interesting is that in 700 °C annealed perovskite nanosheet system, interfacial layer was formed, suggesting that the bonding had become more robust as a result of being annealed at high temperature [15]. Therefore, at this stage, weak bonding between electrode and dielectric is thought to be the crucial factor determining size effect.

4.3. Soft phonon propagation

In perovskite, the frequency of soft phonon mode strongly contributes to the permittivity and cooperative dielectric interactions occur only through the continuous connectivity of -B-O-B- bonds in ABO_3 perovskite layer [18]. The meaning of “soft” phonon mode is the lowest-frequency optical mode. The lattice dynamical properties in the thin films should play a key role in reduction of the dielectric constant. A. A. Sirenko et al. found that the dramatic reduction of dielectric constant in SrTiO_3 thin films compared to that of single crystal is closely related to the hardening of soft phonon modes [19]. It was discovered that the eigenfrequency of the soft phonon mode experiences an increase in thin films of SrTiO_3 compared to that of a single crystal in bulk form. The Lyddane-Sachs-Teller (LST) relation for a crystal with N infrared-active optical modes is given as follow, which is relation between phonon frequencies and static dielectric constant.

$$\frac{\epsilon(0)}{\epsilon(\infty)} = \prod_j^N \frac{\omega_{LOj}^2}{\omega_{TOj}^2} \quad (4.2)$$

$\epsilon(0)$, $\epsilon(\infty)$, ω_{LO} , ω_{TO} are the static dielectric constant, high frequency dielectric constant, frequency of longitudinal optical phonon modes, transverse optical phonon modes respectively. From the LST relation, the ratio of dielectric constant between bulk and thin film is given as follow.

$$\frac{\omega_{TO1,film}^2}{\omega_{TO1,bulk}^2} = \frac{\epsilon_{bulk}(0)}{\epsilon_{film}(0)} \quad (4.3)$$

Therefore, the soft phonon mode is crucial factor determining the dielectric properties. The dielectric properties do not solely depend on the soft phonon frequency, but also on the soft phonon density. In particular, the behavior of phonons near the interface becomes a crucial factor in considering the size effect. When there is a strong bond between the dielectric and electrodes, with close contact, the soft phonons in the high-k dielectric can propagate through the electrodes. As a result, the soft phonon density near the interfaces reduces, similar

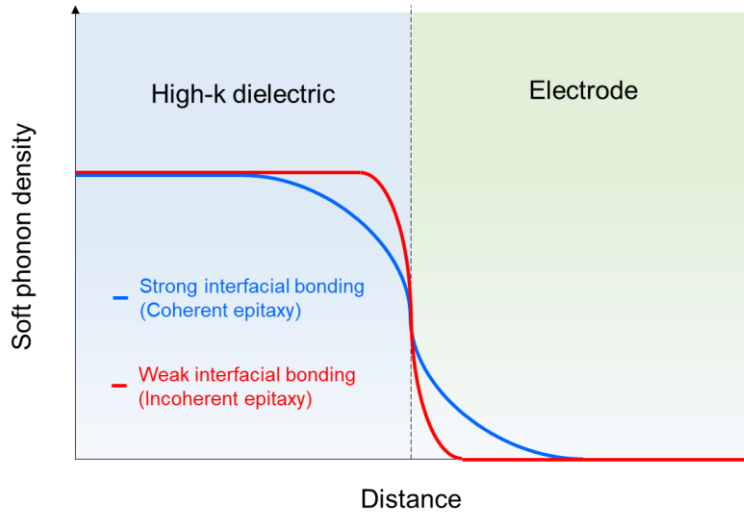


Figure 4.2 Soft phonon density propagation model depending on interfacial bonding.

to the thermal boundary resistance [20]. However, if the bonding between dielectric and electrodes is weak, there would be also weak phonon coupling near the interface, as illustrated in Figure 4.2.

4.4. Thickness dependence of dielectric constant of BHTO

Similar to other high-k dielectrics, reducing the thickness of the dielectric causes a decrease in the dielectric constant of BHTO as in Figure 4.3.

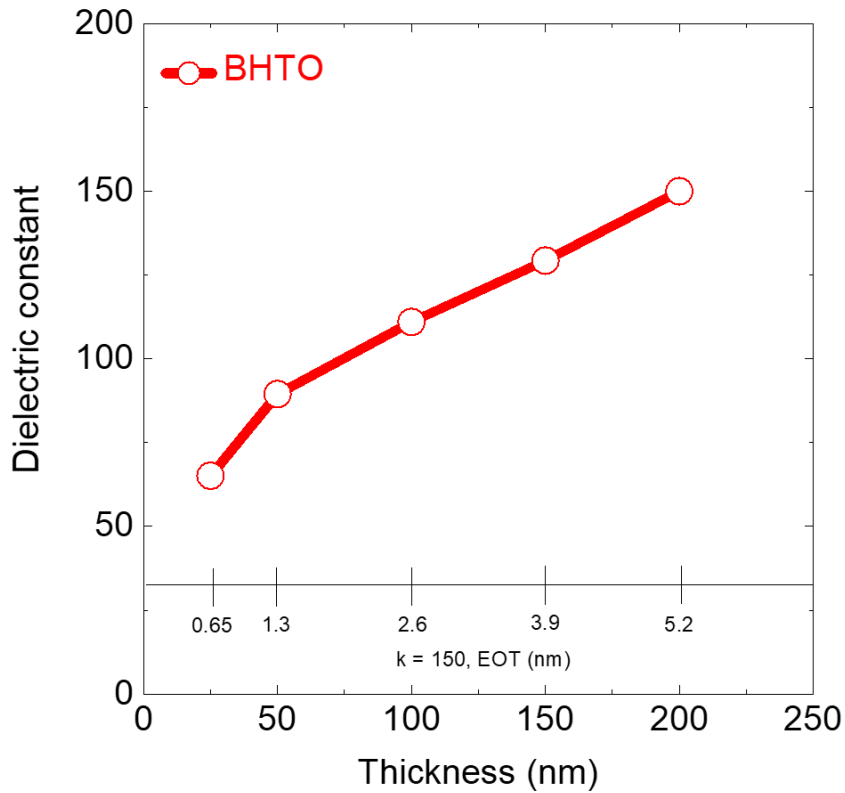


Figure 4.3 Thickness dependent dielectric constant of BHTO.

The additional x-axis in the Figure 4.3 describes the equivalent oxide thickness (EOT) of BHTO when assuming the dielectric constant of BHTO is 150 regardless

of dielectric thickness. In order to estimate the interfacial capacitance, inverse of capacitance per area vs thickness of BHTO plot is in Figure 4.4. It is worth mentioning that the plot is linearly fitted, indicating that a constant interfacial capacitance exists regardless of the thickness of the film.

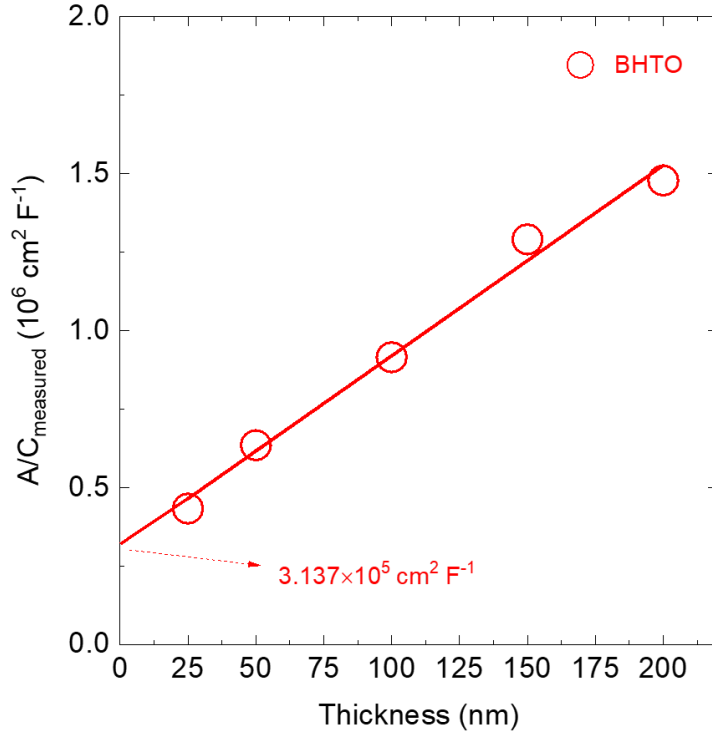


Figure 4.4 Inverse capacitance per area of BHTO depending on the dielectric thickness.

The interfacial capacitance of BHTO is equivalent to that of a 1 nm thin low-k layer with a dielectric constant of 3.6, which is measured to be $3.19 \times 10^{-6} \text{ F/cm}^2$. From the slope of the plot, bulk dielectric constant of BHTO is calculated as 186.

In order to confirm that the interfacial capacitance observed in BHTO capacitors with 4% BLSO electrodes is a characteristic inherent to BHTO, capacitors made of

$\text{Ba}_{0.15}\text{Sr}_{0.85}\text{HfO}_3$ (BSHO) with 4% BLSO electrodes were created for the purpose of comparison. Similar to BHTO, the lattice constant of BSHO is closely matched to the 4% BLSO electrodes, even though the dielectric constant of BSHO is small (~ 30) compared to BHTO. The thickness dependent dielectric constant and inverse capacitance per area depending on dielectric thickness of BSHO is in Figure 4.5.

Top elec./Dielectric/Bottom elec.	Interfacial C/A (F/cm^2)	Bulk dielectric constant (ϵ_b)
BLSO/ $\text{BaHf}_{0.6}\text{Ti}_{0.4}\text{O}_3$ /BLSO	3.19×10^{-6}	186
BLSO/ $\text{Ba}_{0.15}\text{Sr}_{0.85}\text{HfO}_3$ /BLSO	2.56×10^{-6}	38.4
Au/ $\text{PbZr}_{0.53}\text{Ti}_{0.47}\text{O}_3$ /Pt/Ti	1.53×10^{-5}	1066
Pt/(Ba,Sr) TiO_3 /Pt	2.80×10^{-5}	602
Pt/(Ba,Sr) TiO_3 /Pt	4.41×10^{-5}	668
Pt/(Ba,Sr) TiO_3 /Pt	5.41×10^{-5}	675
IrO_2 /(Ba,Sr) TiO_3 / IrO_2	6.67×10^{-4}	458
SrRuO_3 / $\text{Ba}_{0.7}\text{Sr}_{0.3}\text{TiO}_3$ / SrRuO_3	1×10^{-4}	6700
Pt/ $\text{Ba}_{0.7}\text{Sr}_{0.3}\text{TiO}_3$ / SrRuO_3	2×10^{-5}	5700
Au/ $\text{Ba}_{0.5}\text{Sr}_{0.5}\text{TiO}_3$ / SrRuO_3	2.01×10^{-6}	1000
Au/ $\text{Ba}_{0.5}\text{Sr}_{0.5}\text{TiO}_3$ /(La,Sr) CoO_3	1.70×10^{-6}	380
Au/ $\text{Ba}_{0.85}\text{Sr}_{0.15}\text{TiO}_3$ /Pt	2.21×10^{-6}	1141

Table 4.1 Comparison of interfacial capacitance in various dielectric [1,3,21-23].

The interfacial capacitance of BHSO with 4% BLSO electrodes is estimated to be $2.56 \times 10^{-6} \text{ F}/\text{cm}^2$, which is similar to that of BHTO with 4% BLSO electrodes. Therefore, it is believed that the interfacial capacitance is not an intrinsic property of the material. Comparison of the interfacial capacitance with other reported value

is in table 4.1. The interfacial capacitance between 4% BLSO electrodes and BHTO is either comparable or less than that of other systems, which means that the interfacial capacitance effect is large in epitaxially lattice matched system.

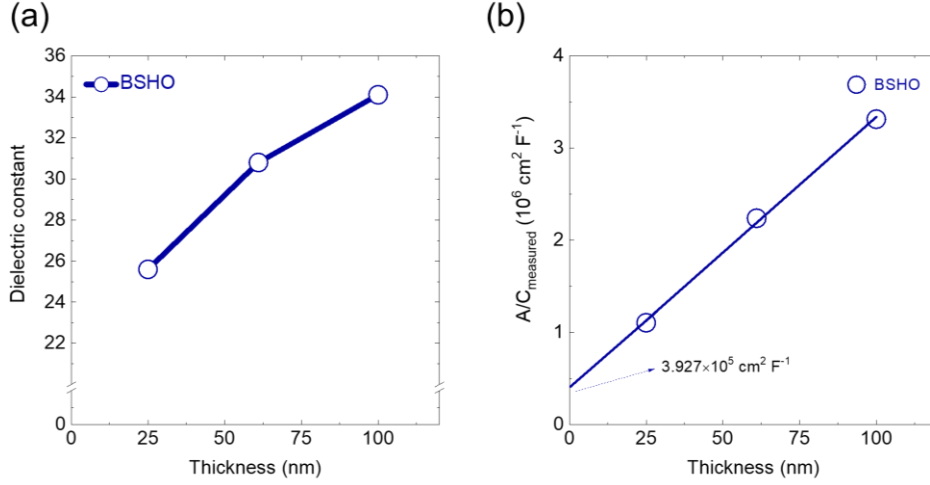


Figure 4.5 (a) Thickness dependent dielectric constant of BSHO (b) Inverse capacitance per area of BSHO depending on the dielectric thickness.

Note that the capacitance for area of 1 nm SiO_2 is $3.45 \times 10^{-6} \text{ F/cm}^2$. In a series configuration of capacitors, the total capacitance cannot surpass the value of the smallest individual capacitance. Therefore, interfacial capacitance higher than the value is required for EOT below 1 nm.

4.5. Effect of top ITO electrode on interfacial capacitance

In order to verify the impact of strong epitaxial bonding on interfacial

capacitance, the top electrode is substituted with amorphous indium tin oxide (ITO), which does not create epitaxial bonding as in Figure 4.6. The top electrode replacement does not affect the epitaxy of BHTO dielectrics. The comparison of dielectric constant depending on dielectric thickness with different top electrodes and interfacial capacitance is shown in Figure 4.7. The interfacial capacitance of BHTO capacitors with top ITO electrode is fitted to be $4.88 \times 10^{-6} \text{ F/cm}^2$, which is about 1.5 times enhancement compared to that of top 4% BLSO electrode. Therefore, the interfacial phonon is only weakly coupled due to the weak bonding between BHTO and ITO, which results in an increase in the interfacial capacitance.

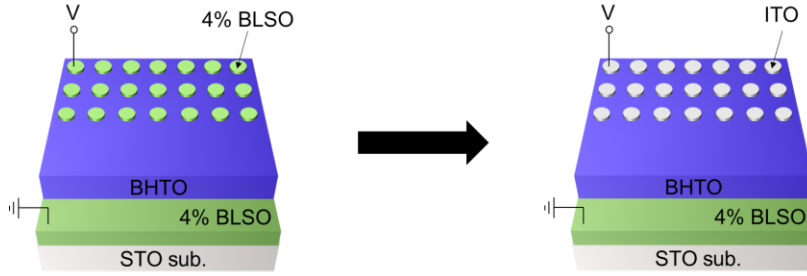


Figure 4.6 Schematic of BHTO MIM capacitors. Top electrode is replaced to ITO.

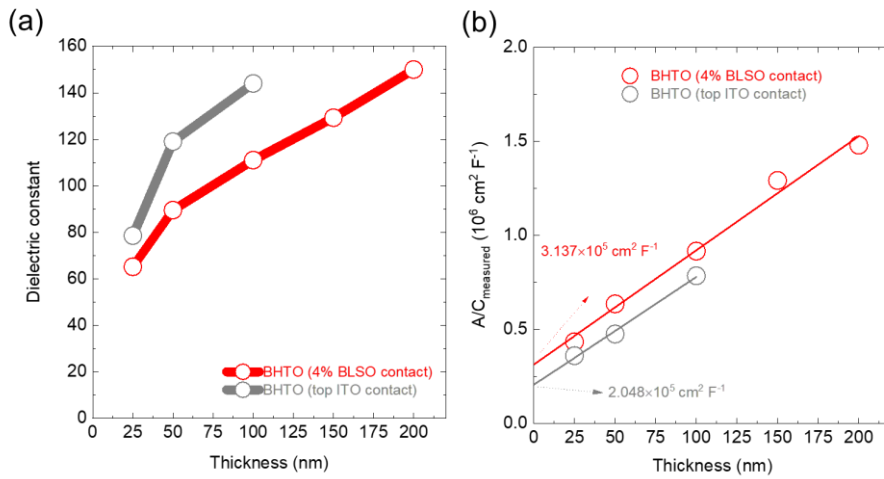


Figure 4.7 Comparison of BHTO MIM capacitors with top 4% BLSO electrodes and ITO electrodes. (a) Dielectric constants (b) Interfacial capacitance.

4.6. Effect of bottom SrRuO₃ electrode on interfacial capacitance

The interfacial capacitance of BHTO capacitors with top ITO electrode is enhanced about 1.5 times, however, this still requires improvement for BHTO of EOT below 1 nm. To enhance interfacial capacitance effect, both the top and bottom interfaces need to be designed and optimized. Using ITO as the bottom electrode would impede the epitaxy of BHTO dielectric since the amorphous nature of the ITO electrode prevents it. Thus, an epitaxial electrode is necessary to ensure that the epitaxy of BHTO dielectric is not obstructed. In order to avoid a strong bond between BHTO and the electrode, it is necessary to intentionally use conducting perovskite oxide with a lattice mismatch. The perovskite SrRuO₃ (SRO) can be a good candidate due to its high electric conductivity [24] and large lattice mismatch to BHTO [25]. The value of the pseudo-cubic lattice constant of SrRuO₃ is $a_{pc} = 3.93 \text{ \AA}$. This means that there is a mismatch of approximately 4% between the in-plane lattice of SrRuO₃ and that of BHTO. The SRO/BHTO/ITO capacitors show significant variations in their dielectric constant when compared to the 4% BLSO/BHTO/ITO capacitors. Therefore, the interfacial capacitance of SRO/BHTO/ITO capacitors depends on the data selections. Figure 4.8 displays the outcomes obtained by utilizing mean values of dielectric constants. The interfacial capacitance of SRO/BHTO/ITO is $8.48 \times 10^{-6} \text{ F/cm}^2$, which is about 3 times enhancement compared to 4% BLSO/BHTO/4% BLSO capacitors. Nevertheless, the inclination of the graph is altered, indicating a modification in the bulk dielectric constant. The calculated bulk dielectric constant for SRO/BHTO/ITO is determined to be 318.

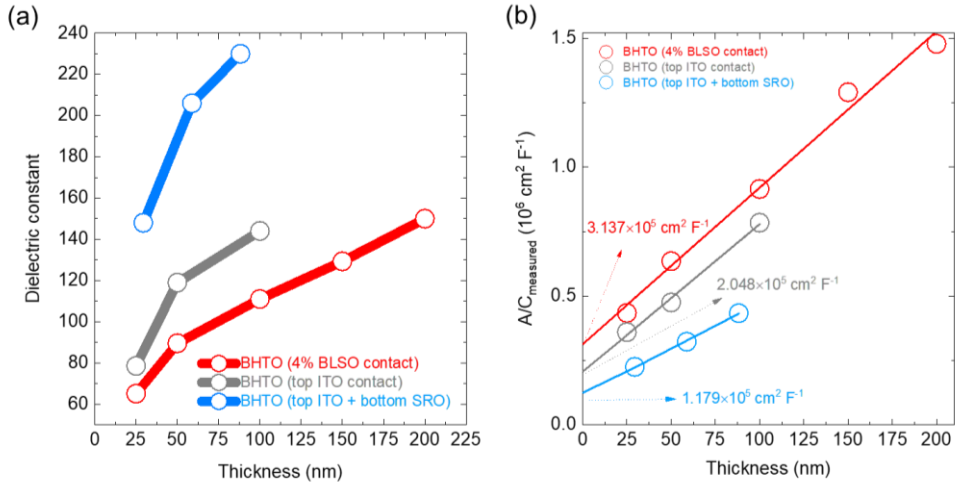


Figure 4.8 Comparison of BHTO MIM capacitors with top SRO electrodes and ITO electrodes. (a) Average dielectric constants (b) Interfacial capacitance when using average dielectric constants.

Figure 4.9 depicts a slightly distinct graph when employing the greatest values of dielectric constants. The interfacial capacitance of SRO/BHTO/ITO capacitors is $1.68 \times 10^{-5} \text{ F/cm}^2$, which is about 5 times enhancement compared to 4% BLSO/BHTO/4% BLSO capacitors. However, the calculated bulk dielectric constant from the slope is determined to be 320, which is similar value when employed average dielectric constants. The increase in bulk dielectric constants is thought to be due to the compressive strains between SRO and BHTO, resulting in increased tetragonality. To verify this, reciprocal space mapping (RSM) was conducted to measure the in-plane and out-of-plane lattice parameters in Figure 4.10. The tetragonality (c/a) of BHTO is 1.0295 on SRO electrode, which is slightly larger than that of BHTO (1.013) on 4% BLSO electrode. The heightened tetragonality has the potential to impact the dielectric constant in the c -axis direction.

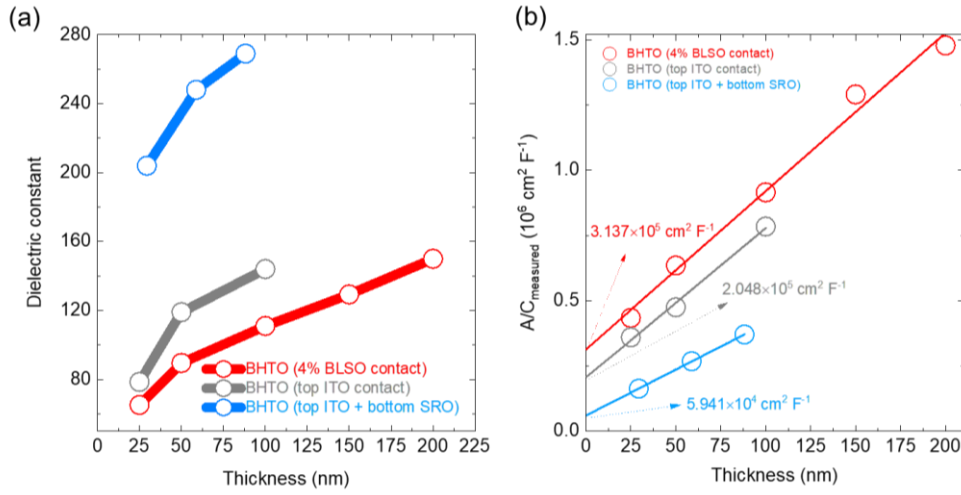


Figure 4.9 Comparison of BHTO MIM capacitors with top SRO electrodes and ITO electrodes. (a) Average dielectric constants (b) Interfacial capacitance when using greatest dielectric constants.

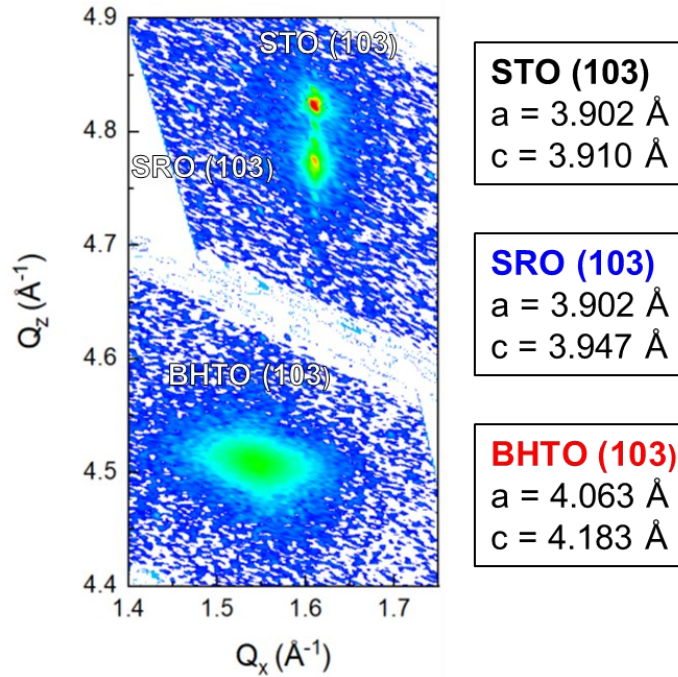


Figure 4.10 RSM of SRO/BHTO/ITO capacitors and derived lattice parameters.

4.7. Conclusion

The key to enhance interfacial capacitance is weaken the interfacial bonding so that the soft phonon does not propagate to the electrodes. This is confirmed by replacement of electrodes, top ITO electrodes and bottom SRO electrodes. When the top ITO electrodes are used, the interfacial capacitance is boosted by 1.5 times. If both the bottom SRO electrodes and the top ITO electrodes are utilized, the interfacial capacitance is enhanced by a factor ranging from 3 to 5. Consequently, the enhancement factor for SRO alone is approximately 2 to 3. However, the dielectric constant of BHTO in its bulk form is also heightened as a result of the increase in tetragonality, brought on by the compressive strain generated by SRO. Nevertheless, the interfacial capacitance is improved regardless of the bulk dielectric constant. It is worth noting that intentionally mismatched epitaxial growth results in undesired defects, which in turn deteriorate the properties of the leakage current. Therefore, additional measures are necessary to mitigate the issue of leakage current that stems from suboptimal epitaxy.

References

- [1] K. Amanuma, T. Mori, T. Hase, T. Sakuma, A. Ochi, Y. Miyasaka, *Jpn. J. Appl. Phys.* **32**, 4150-4153 (1993).
- [2] L. Pintilie, I. Vrejoiu, D. Hesse, G. LeRhun, M. Alexe, *Phys. Rev. B* **75**, 104103 (2007)
- [3] C. S. Hwang, *J. Appl. Phys.* **92**, 432 (2002).
- [4] L. J. Sinnamon, M. M. Saad, R. M. Bowman, J. M. Gregg, *Appl. Phys. Lett.* **81**, 703 (2002).
- [5] X. L. Li, B. Chen, H. Y. Jing, H. B. Lu, B. R. Zhao, Z. H. Mai Q. J. Jia, *Appl. Phys. Lett.* **87**, 222905 (2005).
- [6] C. Zhou, D. M. Newns, *J. Appl. Phys.* **82**, 3081 (1997).
- [7] M. Stengel, N. A. Spaldin, *Nature* **443**, 679-682 (2006).
- [8] Y. S. Kim, J. Y. Jo, D. J. Kim, Y. J. Chang, J. H. Lee, T. W. Noh, T. K. Song, J.-G. Yoon, J.-S. Chung, S. I. Baik, Y.-W. Kim, C. U. Jung, *Appl. Phys. Lett.* **88**, 072909 (2006).
- [9] T. Kojima, Y. Sakashita¹, T. Watanabe, K. Kato, H. Funakubo, *Mat. Res. Soc. Symp. Proc.* **748**, 152 (2002).
- [10] K. Takahashi, M. Suzuki, T. Kojima, Y. Sakashita, K. Kato, O. Sakata, K. Sumitani, H. Funakubo, *Appl. Phys. Lett.* **89**, 082901 (2006).
- [11] L.-W. Chang, M. Alexe, J. F. Scott, J. M. Gregg, *Adv. Mater.* **21**, 4911-4914 (2009).
- [12] M. Stengel, D. Vanderbilt, N. A. Spaldin, *Nature Mater.* **8**, 392-397 (2009).
- [13] Q. Yang, J. Cao, Y. Zhou, L. Sun, X. Lou, *Acta Mater.* **112**, 216-223 (2016).
- [14] M. Osada, K. Akatsuka, Y. Ebina, H. Funakubo, K. Ono, K. Takada, T. Sasaki, *ACS Nano* **4**, 5225-5232 (2010).
- [15] B.-W. Li, M. Osada, Y. Ebina, K. Akatsuka, K. Fukuda, T. Sasaki, *ACS Nano* **8**, 5449-5461 (2014).
- [16] B.-W. Li, M. Osada, Y.-H. Kim, Y. Ebina, K. Akatsuka, T. Sasaki, *J. Am. Chem. Soc.* **139**, 10868-10874 (2017).
- [17] M. S. Khan, H.-J. Kim, T. Taniguchi, Y. Ebina, T. Sasaki, M. Osada, *Appl. Phys. Express* **10**, 091501 (2017).

- [18] J.-H. Sohn, Y. Inaguma, M. Itoh, T. Nakamura, *Mater. Sci. Eng. B* **41**, 50-54 (1996).
- [19] A. A. Sirenko, C. Bernhard, A. Golnik, A. M. Clark, J. Hao, W. Si, X. X. Xi, *Nature* **404**, 373-376 (2000).
- [20] E. T. Swartz, R. O. Pohl, *Rev. Mod. Phys.* **61**, 605-668 (1989).
- [21] R. Plonka, R. Dittmann, N. A. Pertsev, E. Vasco, R. Waser, *Appl. Phys. Lett.* **86**, 202908 (2005).
- [22] J. McAneney, Ph. D. thesis, Queen's University, 2005.
- [23] A. Selmi, M. Mascot, F. Jomni, J.-C. Carru, *J. Alloys Compd.* **826**, 154048 (2020).
- [24] E. Falsetti, A. Kalaboukhov, A. Nucara, M. Ortolani, M. Corasaniti, L. Baldassarre, P. Roy, P. Calvani, *Sci. Rep.* **8**, 15217 (2018).
- [25] Gertjan Koster, Lior Klein, Wolter Siemons, Guus Rijnders, J. Steven Dodge, Chang-Beom Eom, Dave H. A. Blank, Malcolm R. Beasley, *Rev. Mod. Phys.* **84**, 253-298 (2012).

Chapter 5. Properties of SrHfO₃

5.1. Research background

As CMOS integrated circuit technology advances, the power consumption increases with the higher integration density. To decrease power consumption, the operating voltage needs to be lowered, which necessitates a thinner gate oxide. However, as the gate oxide thickness decreases to a few nm, tunneling leakage current becomes unavoidable. Consequently, high-k gate oxide needs to be developed to address this issue. Device power consumption can be classified into two types: static and dynamic power consumption [1]. When the device geometries become smaller, the static power consumption becomes more significant, and it is closely linked to the leakage current in the devices [1-4]. As device sizes decrease, the off-state leakage current becomes increasingly important for device reliability, as the on-state currents also decrease. High-k dielectrics are needed to overcome the leakage current issue with silicon oxides [5-7]. Ideal high-k materials should have a large dielectric constant, low leakage current, and a large breakdown field. In particular, for the high-k dielectric to have low leakage current, it must have a large bandgap (>5 eV), a large conduction band offset (>1 eV), and a low density of defect states within the bandgap that could create a conduction path [8,9].

Extensive research has been conducted on perovskite materials due to their intriguing properties, including superconductivity, ferroelectricity, and the 2-dimensional electron gas (2DEG) [10-17]. In particular, perovskite oxide materials like titanates and hafnates are being investigated as high-k materials [18-41]. SrTiO₃ and BaTiO₃ titanates have a significant dielectric permittivity but with the drawbacks of a small bandgap and large leakage current [18-21]. In contrast, there

is growing interest in perovskite hafnates as a material with robust dielectric properties. Despite having moderately high dielectric constants compared to titanates, hafnates like SrHfO_3 (SHO) and BaHfO_3 (BHO) have a large bandgap and robust dielectric strength [22-41].

SrHfO_3 has been studied as a high-k perovskite gate oxide, as well as a ferroelectric and piezoelectric oxide [25-41]. Over a decade ago, a 4.2 nm-thick epitaxial SHO dielectric was successfully grown on Si using molecular beam epitaxy (MBE) [26,28]. This dielectric demonstrated excellent properties, including an equivalent oxide thickness (EOT) below 1 nm and low leakage current density of $10^{-6} \text{ A cm}^{-2}$ at 2 MV cm^{-1} . Other research groups have also studied SHO as a dielectric with low leakage current and evaluated its potential as a high-k dielectric [31,32,37]. Additionally, a recent report found that the metastable $P4mm$ phase of SHO shows a piezoelectric response [39]. Recently, researchers investigated an alloy system $\text{Pb}_{1-x}\text{Sr}_x\text{HfO}_3$, which combines antiferroelectric PbHfO_3 and paraelectric SrHfO_3 to improve dielectric strength and capacitive energy storage density [40].

Unlike the cubic BHO [30], SHO is known to have five polymorphs: orthorhombic ($Pnma$), orthorhombic ($Cmcm$), tetragonal ($I4/mcm$), tetragonal ($P4mm$), and cubic ($Pm\bar{3}m$) [35,39]. The subtle variations in the rotation and tilt of the HfO_6 octahedra discriminate the polymorphs and the energy differences of them seem to be small [42], since the formation of polymorphs in epitaxial SHO thin films depends on both the epitaxial strain and the stoichiometric variations. Therefore, optimizing the growth condition of SHO is important for electronic device applications which take advantage of its strong dielectric properties.

5.2. Dielectric properties of SrHfO₃

In order to determine the dielectric characteristics of the SrHfO₃ (SHO) dielectric, a conducting layer of 4% La-doped BaSnO₃ (4% BLSO) with a thickness of 150 nm was grown epitaxially on a single crystal SrTiO₃ (001) substrate as the bottom electrode. Subsequently 50-nm-thick SHO dielectric layer was epitaxially deposited, and circular electrodes made of 4% BLSO were placed on top of the SHO layer, creating metal-insulator-metal (MIM) capacitors. The diagram of the devices is presented in the inset of Figure 5.1 (a). The top electrode's size is approximately 53,100 μm^2 , with a diameter of roughly 260 μm . Figure 5.1 (a) and (b) illustrate the capacitance-frequency and current density-electric field characteristic curves of a 50-nm-thick SHO capacitor (grown in 30 mTorr). The dielectric constants (κ) of the SHO capacitors were estimated from the measured parallel capacitance (C_p). Figure 5.2 depicts the DC field dependency of the SHO's dielectric constant, which indicates a minimal influence. The performance of the SrHfO₃ capacitor is impressive when it comes to the behavior of the leakage current density. It is particularly noteworthy that even when the electric field is near the dielectric breakdown point, the leakage density level remains below $10^{-6} \text{ A cm}^{-2}$. In order to obtain a more accurate measurement of the extremely small leakage current in the low field region, a slow and quiet mode was employed. The results showed that at 2 MV cm^{-1} , the leakage current was less than 4 pA, which corresponds to less than $10^{-8} \text{ A cm}^{-2}$, as shown in Figure 5.3. Given the size of our capacitors, which is hundreds of μm and much larger than the length scale of current semiconducting devices, the low leakage current level is even more noteworthy. If the geometry of the devices is scaled down, this level of leakage

current could be further reduced.

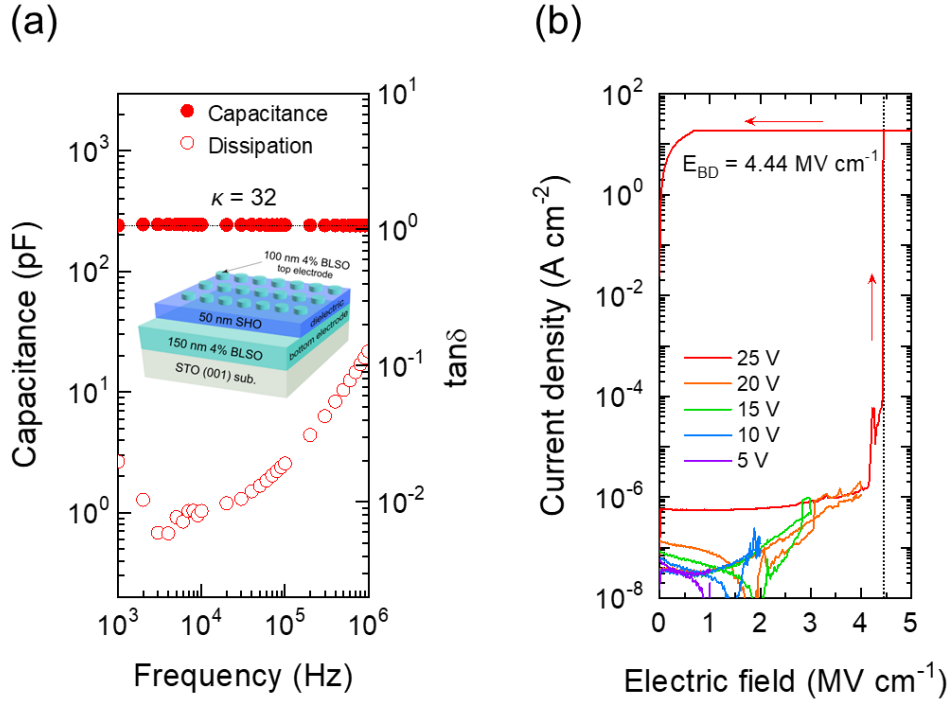


Figure 5.1 Dielectric properties of SrHfO₃. (a) Frequency-dependent capacitance curve of SHO capacitors deposited in 30 mTorr. The inset shows the structure of SrHfO₃ metal-insulator-metal (MIM) capacitors. 4% BLSO are used as bottom and top electrodes. (b) Leakage current density (J) – Electric field (E) characteristic of SHO capacitors deposited in 30 mTorr. Black dotted line represents the breakdown field.

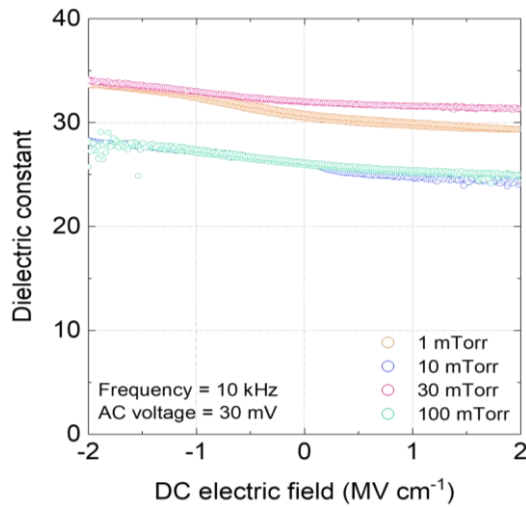


Figure 5.2 DC electric field dependence of dielectric constant for SHO dielectric deposited in various oxygen partial pressures. Significant dependence of dielectric

constant on DC electric field was not observed, implying SHO is linear dielectric material.

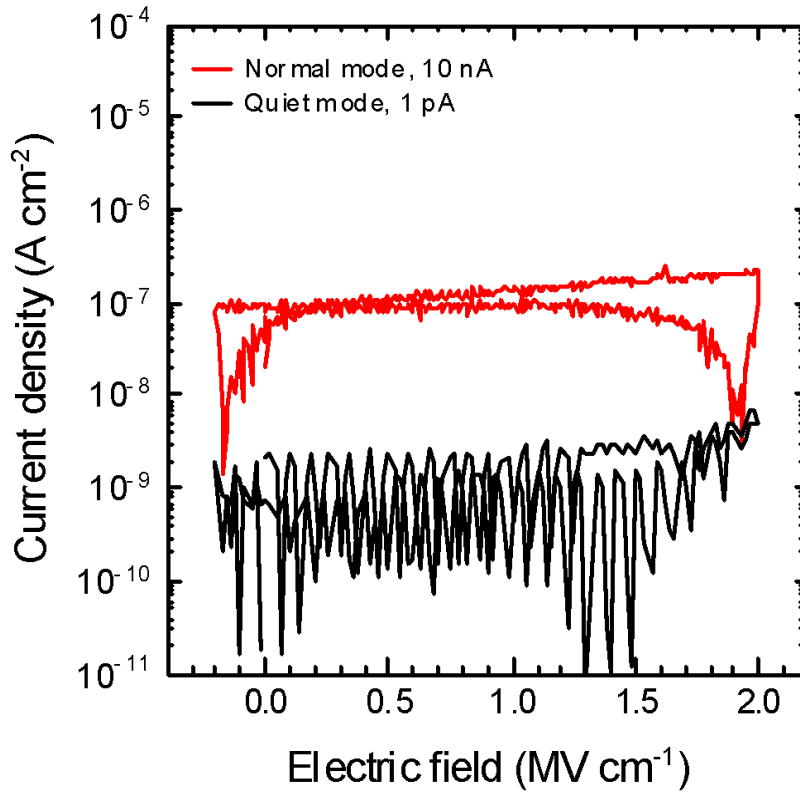


Figure 5.3 Leakage current density vs. electric field measured in two different modes. In a slow and quiet mode, the tens of pA current level dropped to a few pA.

In order to confirm how the growth conditions affect the dielectric properties of SHO capacitors, we created additional capacitors using various oxygen partial pressures. The current density-electric field characteristic curves for these devices are displayed in Figure 5.4. A comparison of the dielectric constant, breakdown field, and leakage current density at 2 MV cm⁻¹ for the SHO capacitors deposited in different oxygen partial pressures is presented in Figure 5.5

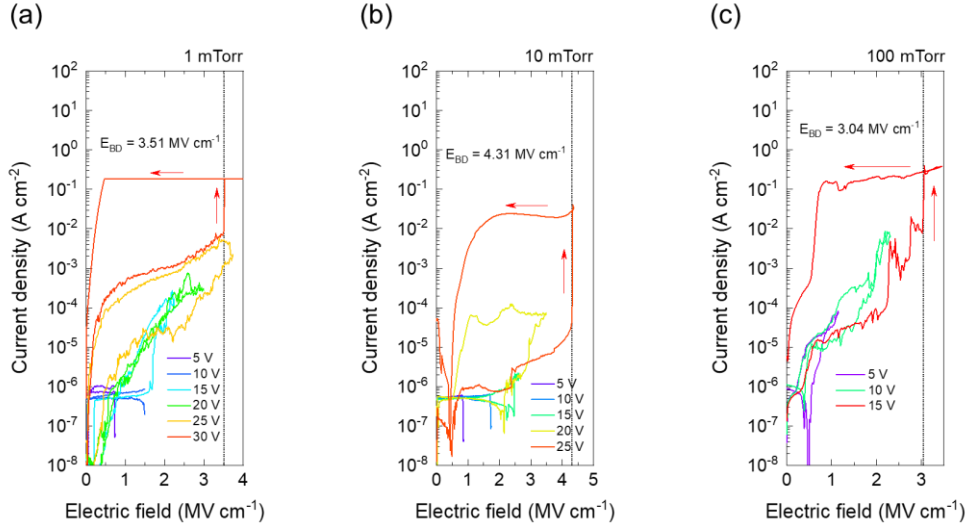


Figure 5.4 Comparison of leakage current density of SrHfO_3 capacitors. (a–c) Leakage current density vs. electric field for SrHfO_3 capacitors deposited in 1, 10, and 100 mTorr, respectively. The thicknesses of SHO are between 50 and 60 nm. Black dotted line represents the breakdown field.

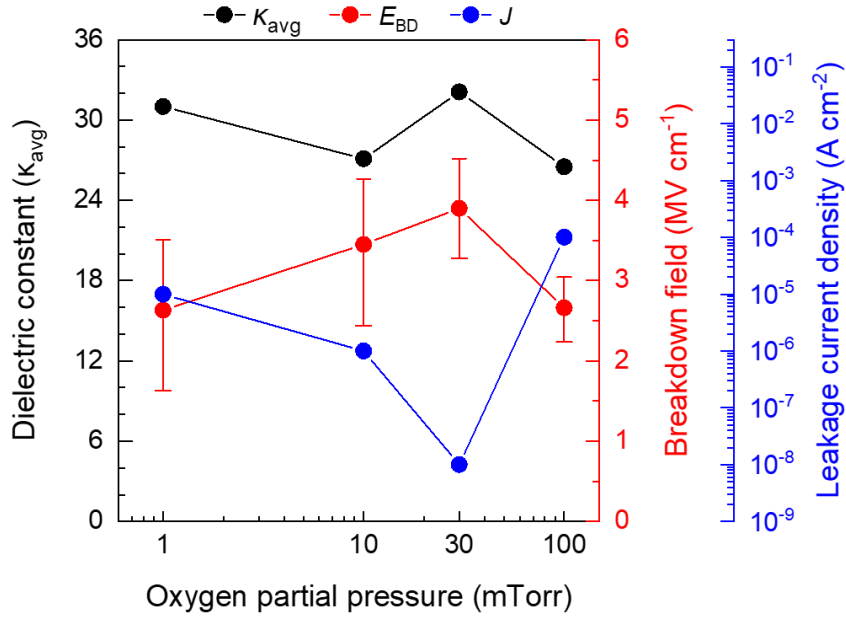


Figure 5.5 Dielectric properties of SrHfO_3 capacitors deposited at various oxygen partial pressures. The leakage current densities are measured at 2 MV cm^{-1} .

The dielectric breakdown field is influenced by external factors such as local defects, resulting in a greater variation than the dielectric constant which must be statistically considered [43]. The error bars in Figure 5.5 represent the maximum and minimum values of breakdown fields. The SHO capacitors exhibit a relatively minor dependence on the oxygen partial pressure when it comes to their dielectric constants. However, the dielectric constant of SHO grown in 30 mTorr reaches a maximum value of 32. Nonetheless, the device's leakage current density displays a distinct minimum at 30 mTorr, indicating that the density of defects within the SHO's bandgap is at a minimum during growth at this pressure. Since conduction through defect states dominates the leakage current in the field range away from the dielectric breakdown field, this suggests that the defect state's concentration is minimal at 30 mTorr.

In order to evaluate the extremely low leakage current density, the current density-electric field characteristic curve of SHO was analyzed using Fowler-Nordheim (FN) tunneling analysis in the vicinity of the breakdown field. The results were compared to other high-k perovskite dielectrics, such as BaHfO₃ (BHO) [24], LaScO₃ (LSO) [17], and LaInO₃ (LIO) [44], as displayed in Figure 5.6(a). The strong linear correlation between $\ln(J E^{-2})$ and E^{-1} for SHO in the high field range confirms that FN tunneling is the primary conduction mechanism in this region close to the breakdown field. As for the 4% BLSO which is heavily doped, its fermi level is estimated to be 0.47 eV above the conduction band minimum using the following formula:

$$E_{F,BLSO} - E_{CBM,BSO} = \frac{\hbar^2 (3\pi^2 n)^{\frac{2}{3}}}{2m_{BLSO}^*} \quad (5.1)$$

where $E_{F,BLSO}$, $E_{CBM,BSO}$, n and m_{BLSO}^* are the fermi level of 4% BLSO, the conduction band minimum energy level of BSO, the carrier concentration of $4 \times 10^{20} \text{ cm}^{-3}$, and the effective mass of 4% BLSO of $0.42m_0$ [45], respectively. Based on the FN tunneling analysis, the conduction band offset (CB offset) between SHO and BSO was found to be 3.3 eV, a significantly high value. The theoretical prediction by Bjaalie et al. also estimated the CB offset between SHO and BSO to be 3.27 eV [46], which closely agrees with our calculation. This CB offset is comparable to the value between Si and SiO₂, which is 3.2 eV according to previous studies [7]. In Figure 5.6(b), the band alignment of various materials is compared. Compared to other dielectrics, the conduction band offset between SHO and BSO is 2-3 times greater, which is considered to be the primary reason for the low leakage current density observed. In our previous publication [43], we noted that the electron affinity of Si is comparable to the work function of 4% BLSO, which is approximately 4 eV. Therefore, a large conduction band offset of about 2.8 eV is expected between silicon and SHO, resulting in very low leakage current, as reported in experiments [26-28]. To maintain a very low defect-assisted tunneling current, along with the significant conduction band offset, it is essential that there are minimal defect states present inside the bandgap that could create a conduction path. Figure 5.7 shows the optical band gap of SHO thin films grown on MgO (001) substrate. Tauc's plot was employed to estimate both the direct and indirect band gap of SHO. The low leakage current density is attributed to the broad optical band of SHO, which is approximately 6 eV. Figure 5.8 illustrates the relationship between the leakage current density and dielectric constant of various oxides, including SHO, as presented in several publications [17-19,24,44,47-54]. It highlights the exceptional potential of SHO as a dielectric material in

semiconductor devices.

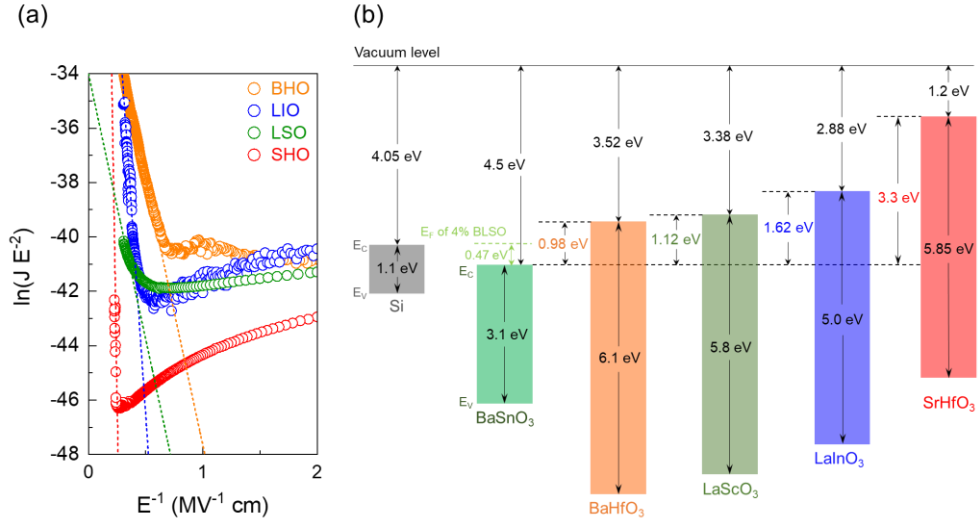


Figure 5.6 Analysis of Fowler-Nordheim tunneling and comparison of band levels. (a) $\ln(J E^{-2})$ vs. E^{-1} plot for Fowler-Nordheim analysis of BHO, LSO, LIO and SHO capacitors deposited in 30 mTorr using the following relation, $J \propto E^2 \exp\left(\frac{-4\sqrt{2m_{SHO}^*}\phi^2}{3e\hbar E}\right)$. (b) Comparison of the band levels of high-k perovskite oxides, BHO, LSO, LIO and SHO, with respect to BSO and Si.

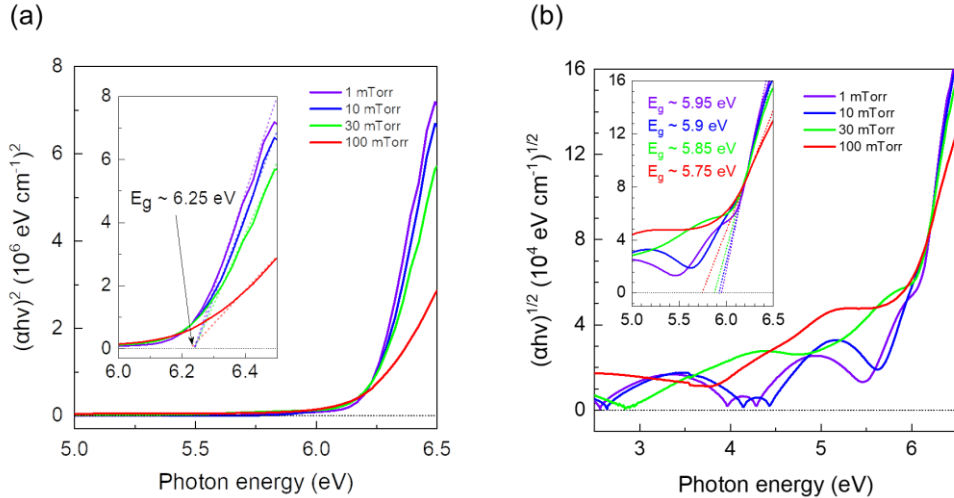


Figure 5.7 Optical band gap of SHO thin films grown on MgO (001) substrate. Tauc's plot for (a) direct band gap and (b) indirect band gap for SHO thin films grown in 1, 10, 30, and 100 mTorr. The inset in (a) and (b) show a magnified view

of the photon energy from (a) 6.0 to 6.5 eV and (b) 5.0 to 6.5 eV, respectively. The colored dotted lines in the inset show extrapolation of the linear part. In the case of SHO thin films deposited in 30 mTorr, direct band gap and indirect band gap are estimated to be 6.25 eV and 5.85 eV, respectively.

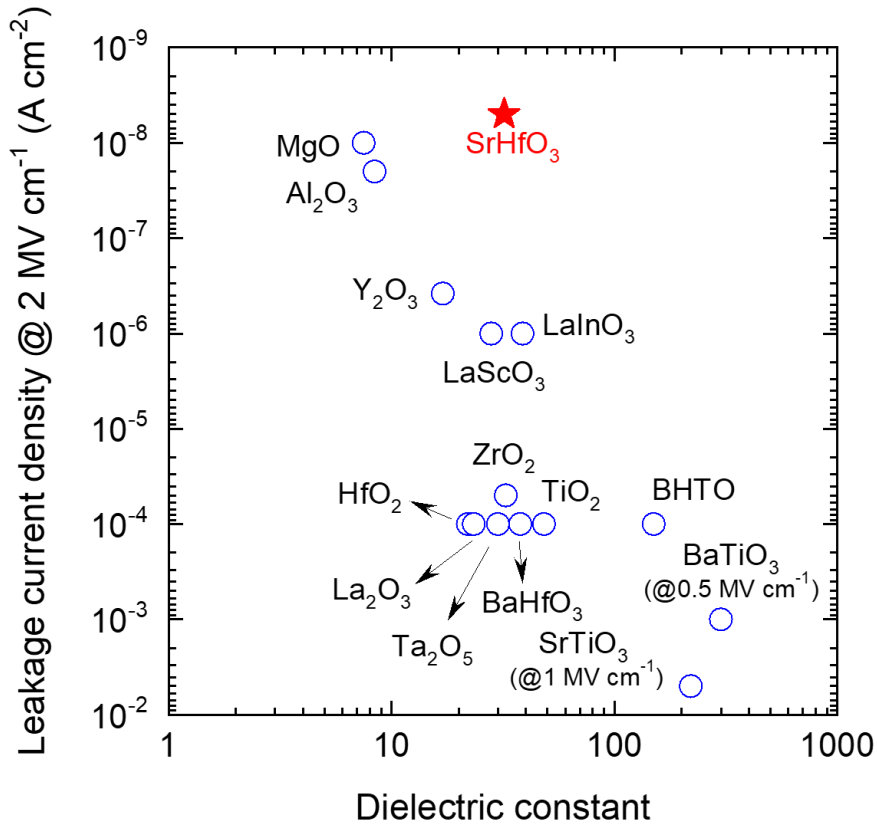


Figure 5.8 Comparison of leakage current density for binary and ternary gate oxides. High-k SrHfO₃ perovskite dielectric has ultra-low leakage current density ($< 10^{-8} \text{ A cm}^{-2}$ at 2 MV cm^{-1}) compared to other oxides.

5.3. Field-effect transistor using SrHfO₃ dielectric

In order to verify the low leakage current in a field effect device, an n-type field-effect transistor (FET) was fabricated using SHO as the gate oxide, lightly doped BSO as the channel, and degenerately doped BSO as the electrodes. A schematic of the device is shown in Figure 5.9(a). To minimize the threading dislocations

resulting from the lattice mismatch between the channel and the substrate, a 150-nm-thick BSO buffer layer was deposited before the channel deposition. A 20-nm-thick 0.3% BLSO channel layer was then grown on top of it, using a line patterned silicon stencil mask. In order to create a channel length of 60 μm , a stainless stencil mask was used to deposit 4% BLSO as the source and drain electrodes. Finally, a 100-nm-thick SHO gate oxide and 4% BLSO gate electrodes with a length of 70 μm were added. An optical microscope image of the device is shown in Figure 5.9(b). The epitaxial growth of the FET was confirmed using high-resolution X-ray diffraction, which is displayed in Figure 5.10. The device's output characteristics, which exhibit standard n-type field-effect transistor behavior, are presented in Figure 5.9(c). The V_{DS} was swept from 0 V to 15 V, while V_{GS} was applied from 0 V to 18 V with a 2 V interval. The device's transfer characteristics in the saturation region are displayed in Figure 5.9(d), which was verified by the output characteristics. The device has an on-off ratio of approximately 10^8 and a maximum mobility of around $80 \text{ cm}^2 \text{ V}^{-1} \text{ s}^{-1}$. The field-effect device exhibits a leakage current of 10^{-11} A at 2 MV cm^{-1} , which corresponds to a leakage current density of $10^{-7} \text{ A cm}^{-2}$, similar to the values measured in capacitor structures. However, it is expected that the small 10 pA leakage current measured in normal mode will decrease when measured more precisely in quiet mode. The transfer curve of the device shows a very small clockwise hysteresis, indicating that the charge trap densities that cause the hysteresis are indeed small in the SHO gate oxide. Once more, this finding aligns with the low defect density and low leakage current within the SHO gate oxide's bandgap. Figure 5.11 presents the $I_{\text{D}}^{0.5}$ vs. V_{GS} plot of the device, which is used to extrapolate the threshold voltage.

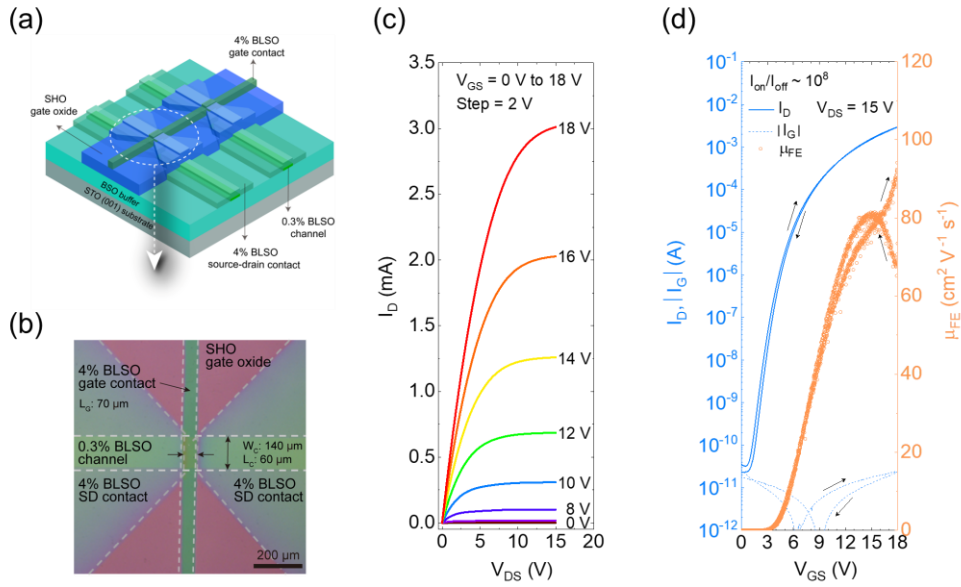


Figure 5.9 FET in an n-type accumulation mode made with 0.3% La-doped BaSnO₃ channel layer and SrHfO₃ gate oxide. (a) A schematic of the device. (b) The top view of the device pictured by an optical microscope. White dotted lines are plotted to illustrate each deposited layer. The channel length (L) of 0.3% La-doped BaSnO₃ is 60 μm , and the average channel width (W) is 140 μm . The gate length (L) is 70 μm . (c, d) The output and transfer characteristic of the device, respectively.

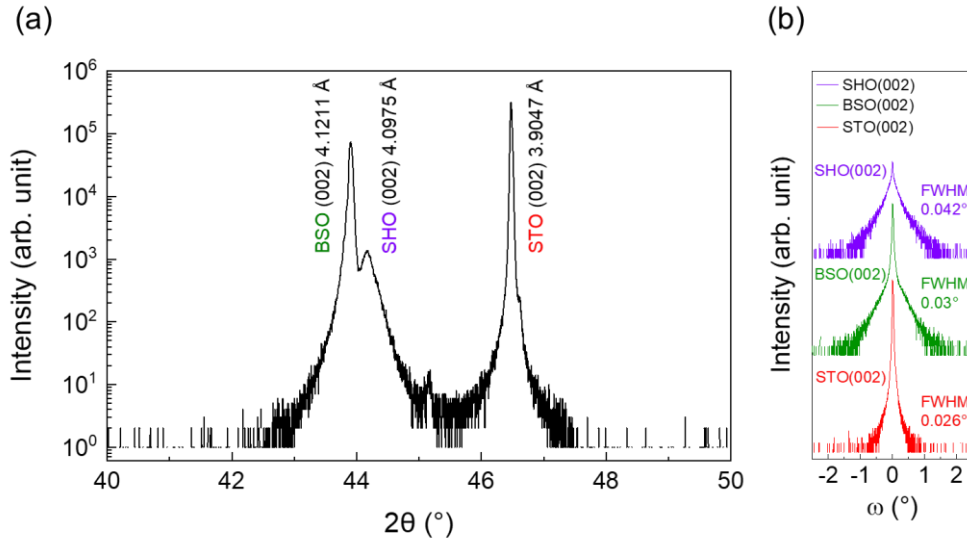


Figure 5.10 X-ray diffraction (XRD) of SHO FET. (a) θ -2 θ scan and (b) rocking curves for FET with SHO gate oxide deposited in 30 mTorr.

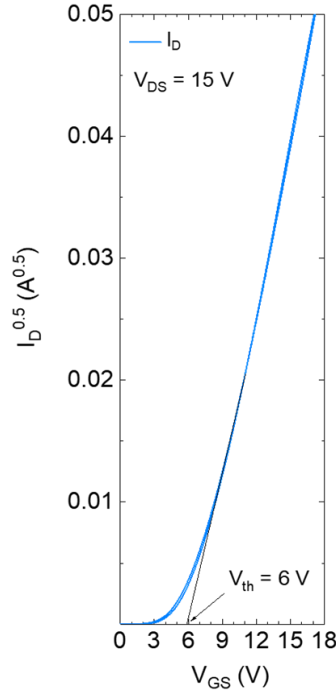


Figure 5.11 Threshold voltage (V_{th}) of the device in the saturation region. V_{th} extracted by the linear extrapolation of $\sqrt{I_D}$ vs V_{GS} plot is estimated to be 6 V.

5.4. Structural properties of SrHfO₃

To investigate the outstanding dielectric properties of SHO grown using pulsed laser deposition (PLD) at an oxygen partial pressure of 30 mTorr, we conducted reciprocal space mapping (RSM) measurements around the (013) plane on SHO capacitors deposited at 1, 10, 30, and 100 mTorr. The RSM data is presented in Figure 5.12(a), and it was observed that the values of Q_x corresponding to the diffraction peaks for SHO and 4% BLSO are nearly identical, indicating that SHO dielectrics grow coherently on 4% BLSO. The dimensions of the in-plane and out-of-plane lattice and the unit cell volume of SHO are displayed in Figure 5.12(b). As the oxygen partial pressure increases, the in-plane lattice constant becomes larger,

while the out-of-plane lattice constant becomes smaller, whereas the unit cell volume ($V_{\text{unit cell}} = (a_{\text{ip}})^2 \times a_{\text{op}}$) barely changes. The SHO dielectrics deposited under various oxygen pressures have a unit cell volume ranging from 68.6 to 69.0 \AA^3 . This value is a bit smaller than the unit cell volume of the $Pm\bar{3}m$ cubic phase ($V_{\text{unit cell, bulk}} = 69.6 \text{ \AA}^3$) [35].

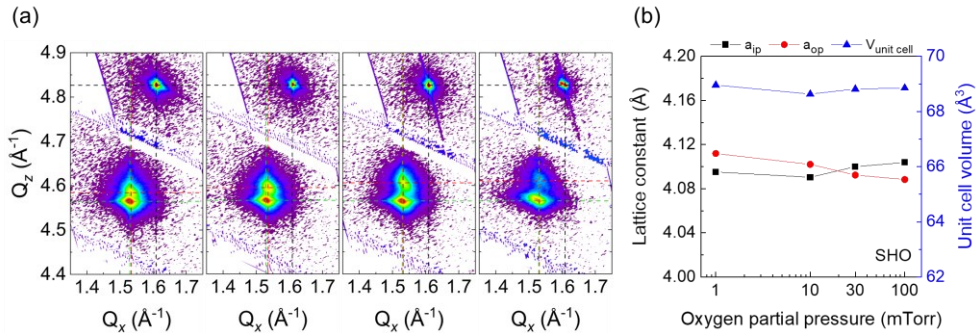


Figure 5.12 Reciprocal space mapping (RSM) measurement. (a) RSM (013) images for SHO capacitors deposited in 1, 10, 30, and 100 mTorr. The red, green, and black dotted lines represent the peak position for SHO, 4% BLSO, and STO, respectively. (b) The in-plane (a_{ip}), out-of-plane lattice constant (a_{op}), and unit cell volume ($V_{\text{unit cell}}$) for SHO calculated from the RSMs.

To gain a better understanding of the phase of SHO dielectrics grown in 30 mTorr, we conducted a reciprocal space mapping (RSM) of the (013) plane by rotating the substrate clockwise at angles of 0° , 90° , 180° , and 270° (refer to Figure 5.13). The Q_z values of the SHO peak positions in Figure 5.13(a) are consistent with each other, indicating that the in-plane symmetry of the SHO dielectric grown in 30 mTorr is fourfold. Thus, it can be deduced that the form of the SHO dielectric's polymorph grown in a 30 mTorr environment is either tetragonal or cubic under tensile strain, which leads to a marginally larger in-plane lattice constant ($a_{\text{ip}} = 4.100 \text{ \AA}$) compared to the out-of-plane lattice constant ($a_{\text{op}} = 4.092$

Å). As the peak positions of SHO and 4% BLSO were quite similar, investigating the influence of oxygen partial pressures on the structural characteristics of SHO presents a challenge. Afterward, we prepared thin films of SHO by depositing them directly on SrTiO₃ (STO) (001) substrate using various oxygen partial pressures. The thickness of the films ranged between 45 and 55 nm, and this was verified using X-ray reflectivity (XRR) measurement, which can be seen in Figure 5.14. We conducted RSM measurement around the (013) plane using SHO thin films that were deposited in 1, 10, 30, and 100 mTorr, as displayed in Figure 5.15(a). In contrast to SHO dielectrics grown on 4% BLSO, the growth of SHO thin films on the STO substrate is not coherent due to the significant mismatch in lattice (~4.5%) between SHO and the STO substrate. Despite all the films having similar thickness, the SHO film deposited in 30 mTorr exhibits a well-defined peak intensity and shape compared to other films. The changes in the in-plane, out-of-plane lattice constants, and unit cell volume with increasing oxygen partial pressure are similar to those observed in SHO grown on 4% BLSO, and these results are summarized in Figure 5.15(b).

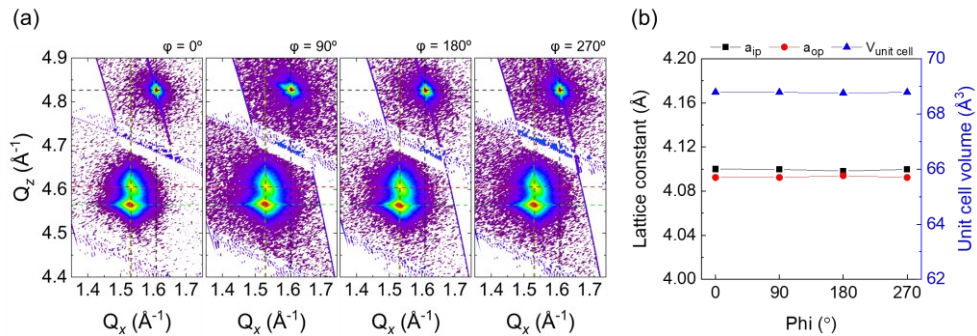


Figure 5.13 RSM (013) measurement for SHO capacitors deposited in 30 mTorr. (a) The RSM (013) images measured by rotating the devices 0° , 90° , 180° , and 270° from the left. (b) The in-plane, out-of-plane and unit cell volume of SHO calculated from the RSM (013) images.

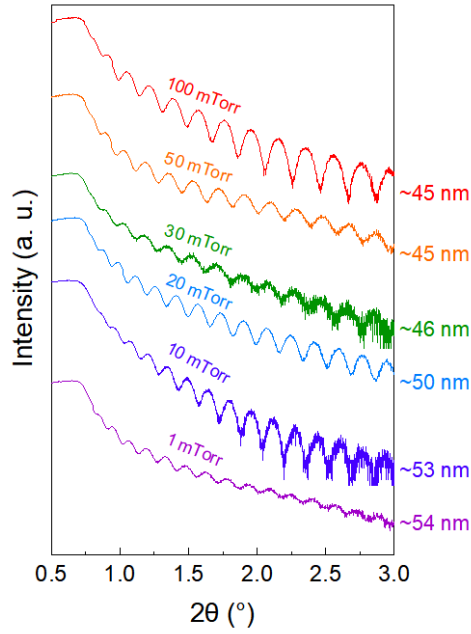


Figure 5.14 X-ray reflectivity (XRR) measurement for SHO thin films. The experimental data of SHO thin films grown at 1, 10, 20, 30, 50, and 100 mTorr. The thickness of the films is calculated from the critical angle and fringes. All films have a thickness in the range of 45–55 nm.

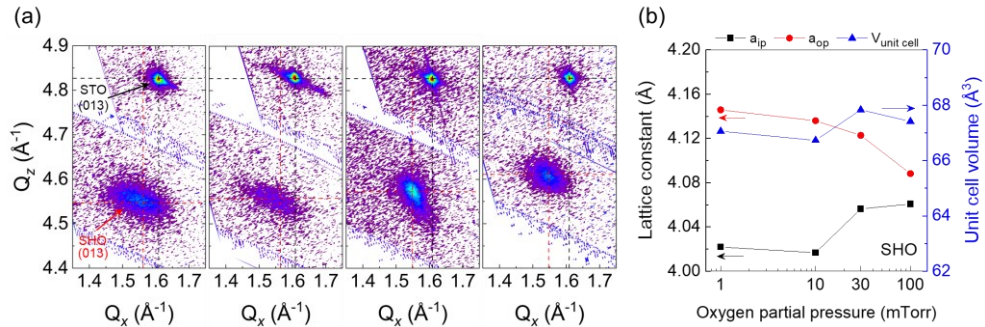


Figure 5.15 Reciprocal space mapping (RSM) measurement. (a) RSM (013) images for SHO thin films deposited in 1, 10, 30, and 100 mTorr on STO substrates. (b) The in-plane (a_{ip}), out-of-plane lattice constant (a_{op}), and unit cell volume ($V_{unit\ cell}$) for SHO calculated from the RSMs.

The θ - 2θ scans and rocking curves for SHO films fabricated under varying oxygen partial pressures are illustrated in Figure 5.16(a). The 2θ peak position of SHO shifts towards the left as the oxygen partial pressure drops. The out-of-plane lattice constants obtained from the (002) Bragg peaks of SHO films are presented in Figure 5.16(b), indicating that the out-of-plane lattice constants decrease as the oxygen partial pressure increases. The lattice constant of all films exceeds that of bulk SHO possessing the *Pnma* orthorhombic phase with an a_{pc} of approximately 4.087 Å [35]. Given the lattice mismatch between SHO and the STO substrate ($\sim 4.5\%$), the out-of-plane lattice constant of SHO films should be greater than that of bulk SHO due to the compressive in-plane strain. With an increase in oxygen partial pressure, the relatively lighter Sr ions with a molecular mass of 87.62 scatter more than the Hf ions with a molecular mass of 178.486, leading to suppressed stoichiometry of Sr in comparison to Hf. Hence, the Hf-ratio in SHO films becomes enriched as the oxygen partial pressure increases, and the lattice constant decreases due to the presence of increasing Hf^{4+} ions with an ionic radius smaller than Sr^{2+} ions.

The variation in the cation stoichiometry due to the oxygen partial pressures was validated by X-ray photoelectron spectroscopy (XPS) and inductively coupled plasma atomic emission spectroscopy (ICP-AES), as demonstrated in Figure 5.17, which encompasses the XPS spectra. Additionally, we fabricated SHO thin films by altering the growth temperature and energy fluence while maintaining a constant oxygen partial pressure of 30 mTorr. The out-of-plane lattice constant is not considerably affected by the growth temperature and energy fluence. However, the crystallinity of the films deteriorates below the growth temperature of 750 °C, as

indicated in Figure 5.18.

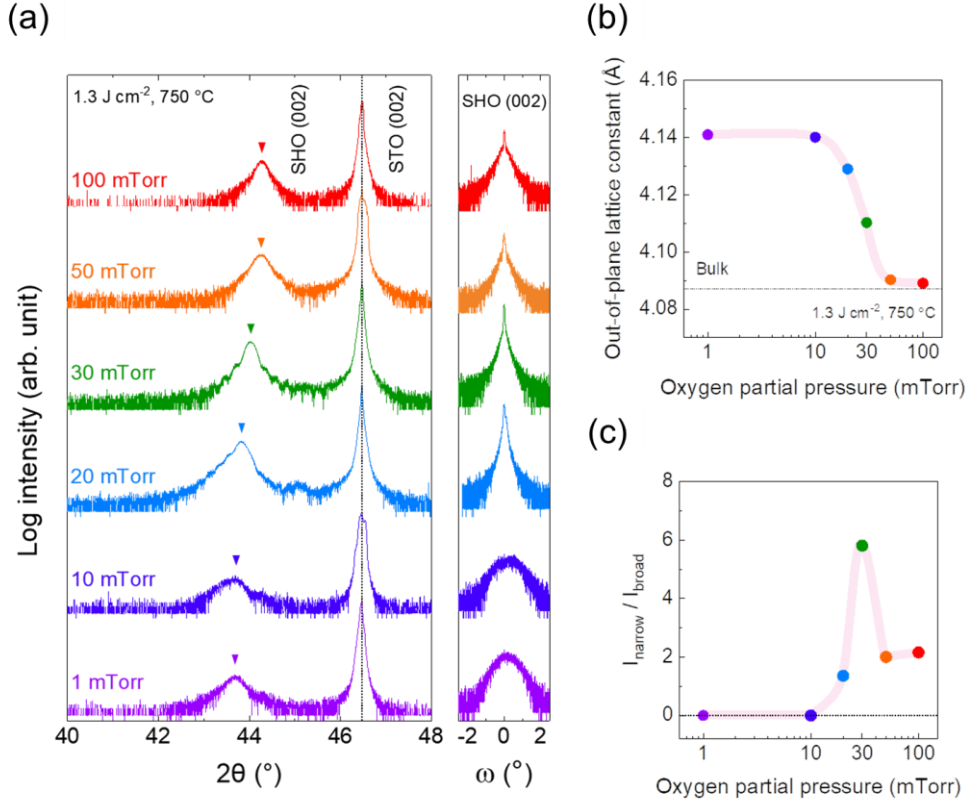


Figure 5.16 X-ray diffraction measurement. (a) θ -2 θ scan and rocking curves for SrHfO₃ thin films grown in various oxygen partial pressures. The energy fluence and growth temperature are fixed at 1.3 J cm⁻² and 750 °C, respectively. Black dotted line represents the 2 θ peak position of STO. (b) The out-of-plane lattice constant of SHO thin films vs. oxygen partial pressures. (c) The intensity ratio of the narrow component to the broad component in the rocking curves.

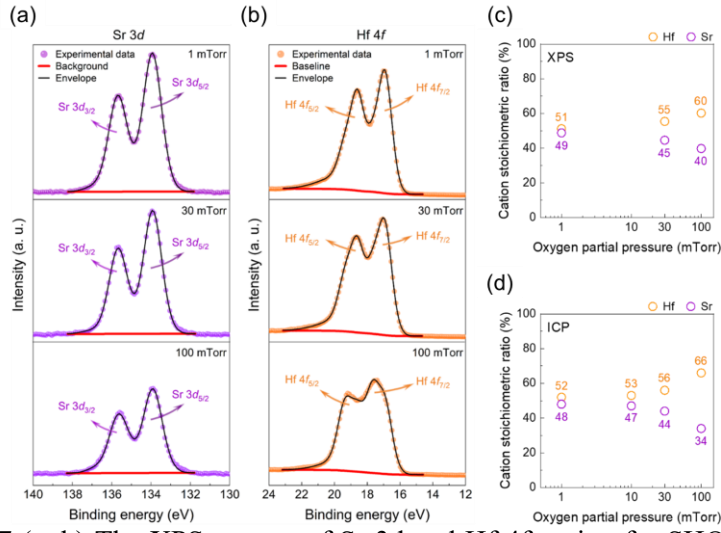


Figure 5.17 (a, b) The XPS spectra of Sr 3d and Hf 4f region for SHO thin films deposited in various oxygen partial pressures. (c) Cation stoichiometric ratio in SHO thin films grown in different oxygen partial pressures is calculated from the XPS spectra. The compositional ratios are obtained by integrating the area of Sr 3d and Hf 4f core levels and dividing the area into relative sensitivity factors (RSF) to scale the peak areas. (d) Cation stoichiometric ratio in SHO thin films grown on MgO (001) substrate is obtained through ICP-AES measurements.

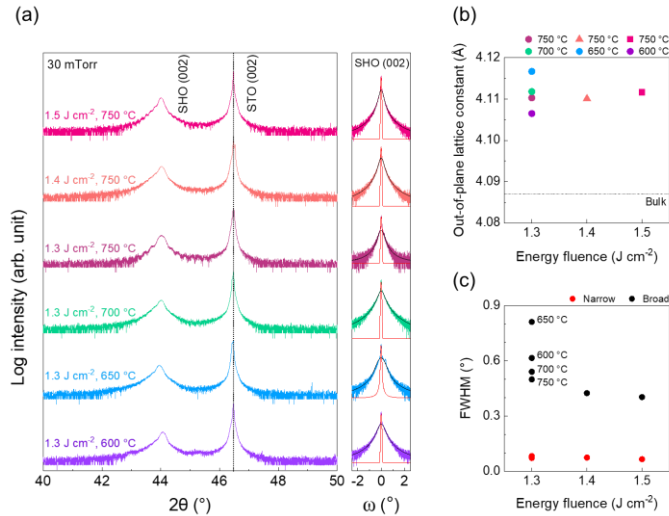


Figure 5.18 X-ray diffraction (XRD) measurement for SHO thin films. (a) θ -2 θ scan and rocking curves for SrHfO₃ thin films on SrTiO₃ (001) substrate grown at various energy fluence and growth temperature. The oxygen partial pressure is fixed at 30 mTorr. Black dotted line represents the 2 θ peak position of STO. Red and black lines represent the result of fitting rocking curves by using Voigt functions with narrow and broad linewidth, respectively. (b) The out-of-plane lattice constant of SHO thin films vs. energy fluence. (c) The value of full width at half maximum (FWHM) calculated from the rocking curves.

The rocking curves of the SHO films grown in 20, 30, 50, and 100 mTorr are made up of narrow (yellow) and broad (black) components. In contrast, other SHO films grown in lower pressure have only a broad component, as displayed in Figure 5.19. Rocking curves that consist of two components are often observed in epitaxial films [55]. Typically, the narrow components in films are related to long-range correlation and arise when the films are partially strain-relaxed or grown coherently on a substrate. In contrast, broad components are associated with defect-related short-range disorder and are present when the films are partially or fully strain-relaxed on a substrate [56,57]. In Figure 5.16(c), the ratios of the narrow component intensity to the broad component intensity (I_{narrow}/I_{broad}) are shown. The ratios decrease at oxygen partial pressures higher or lower than 30 mTorr. For SHO films deposited in 1 and 10 mTorr, there is only a broad component, indicating that there are notable short-range structural disorders. The largest intensity ratio of the narrow component is observed in the SHO film deposited in 30 mTorr, indicating that it has the least defects, which is consistent with its excellent dielectric properties. Figure 5.20 displays the result of the 2 θ peak deconvolution for SHO films grown in 1, 10, 30, and 100 mTorr. The 2 θ peak of SHO films grown in oxygen partial pressure lower than 30 mTorr becomes asymmetric and can be deconvoluted into two Voigt functions, indicating that there are disordered domains with slightly different out-of-plane lattice constant. The lattice constant and crystallinity of the SHO films are significantly affected by the oxygen partial pressure as determined by the XRD measurement. The SHO film deposited in 30 mTorr has a well-shaped, symmetric 2 θ peak, as well as Kiessig fringes on both sides of the peak, and the appropriate lattice constant. These features suggest that it has the highest crystallinity and was grown under the optimal growth conditions.

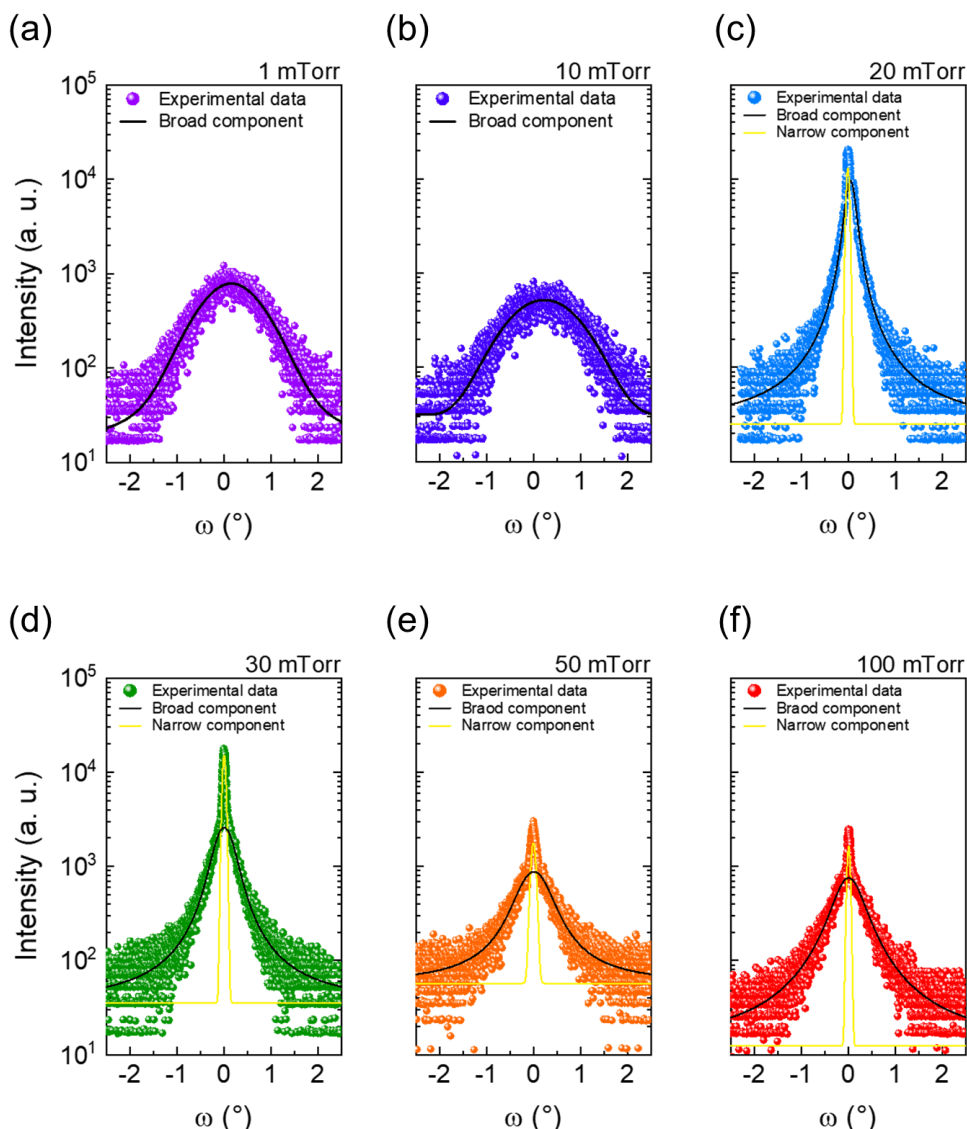


Figure 5.19 Deconvolution of rocking curves for SHO (002). (a–f) The rocking curves for SHO thin films on STO substrate grown in 1, 10, 20, 30, 50 and 100 mTorr, respectively. Black and yellow lines show the results of deconvolution of rocking curves for SHO (002) by using Voigt functions with broad and narrow linewidth, respectively.

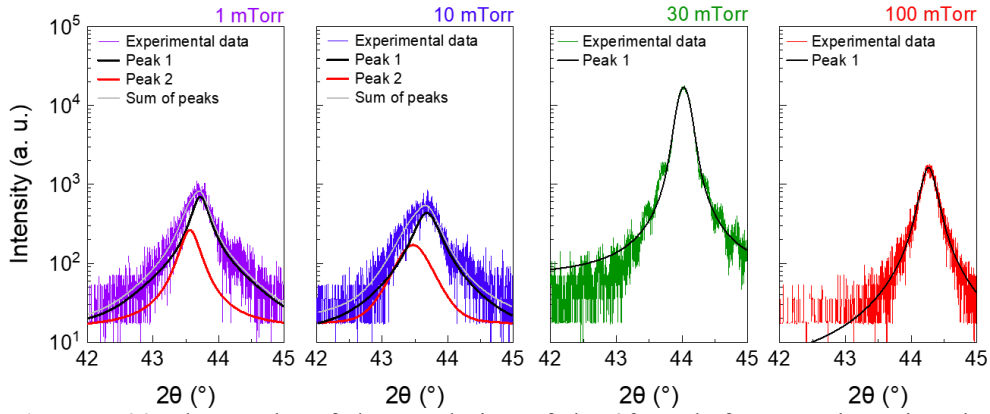


Figure 5.20 The results of deconvolution of the 2θ peak for SHO by using the Voigt functions (black and red line). Symmetric 2θ peak for SHO deposited in 30 and 100 mTorr is fitted by only one Voigt function, whereas asymmetric one is deconvoluted into two Voigt functions.

The scanning transmission electron microscopy (STEM) analysis was used to examine the microstructures of the SHO film that was produced under 30 mTorr. The STEM images of the film in cross-section demonstrate that the thickness of the SHO film is approximately 50 nm and it is uniform in the Figure 5.21(a). A high-angle annular dark-field (HAADF)-STEM image shows vertical contrasts that originate from threading dislocations and propagate from the STO-BLSO interface through the film. Threading dislocations that extend up to the SHO region are observed, and the mid-angle annular dark-field (MAADF)-STEM image of the region exhibits bright contrast at the STO-BLSO interface, as well as the threading dislocations due to the local strain fields around them. However, the BLSO-SHO interface does not exhibit any visible strain contrast. The atomic-resolution HAADF-STEM image of the BLSO-SHO interface shows the epitaxial growth of SHO on BLSO, and the interface roughness is measured to be between 1 and 2 nm.

The STEM images of the SHO region reveal non-uniform contrasts with visible

dark patches. In Figure 5.21(b), the energy dispersive X-ray (EDX) elemental maps of the SHO region indicate local non-stoichiometry, with the dark patches (indicated by yellow arrows) containing lower Sr content. These dark patches are attributed to non-stoichiometric and amorphous regions within the SHO film, as evidenced by their amorphous textures in the HAADF- and bright-field (BF)-STEM images, as shown in Figure 5.21(c). The presence of small grains with a diameter of less than 20 nm, misoriented from the matrix crystal, is also observed (indicated by yellow arrows). The presence of such defects is consistent with the non-vanishing broad component observed in the X-ray rocking curves presented in Figure 5.16(a), even under the optimal deposition condition of 30 mTorr pressure. We suspect that SHO films grown under various conditions may have different levels of disorder, such as variations in the size and density of grains, dislocations, and other factors, which could influence the material's dielectric properties and device performance. While a comparative microstructure analysis would be necessary to understand the relationship between structure and properties, the study would require a careful approach and a reliable quantification method. Therefore, we leave this task for future research.

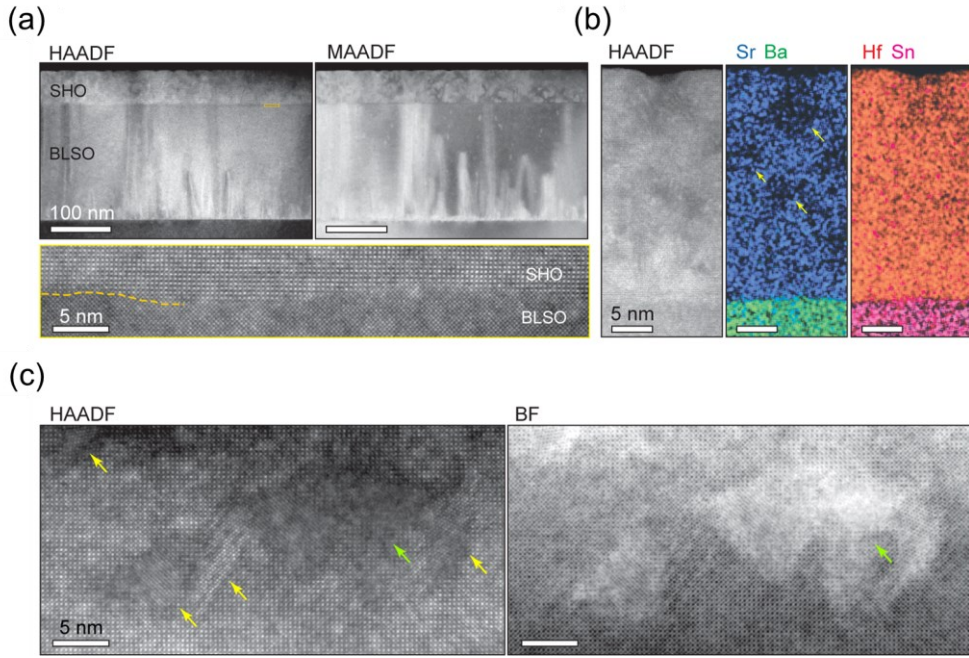


Figure 5.21 (a) Cross-sectional STEM images of the SHO capacitors grown in 30 mTorr. Magnified HAADF-STEM image of the SHO-BLSO interface (yellow box) is presented at the bottom. The interface is indicated with the dashed line. (b) EDX elemental maps (in atomic percentage) of the SHO film. Color codes: Sr-blue, Ba-green, Hf-red, and Sn-magenta. Sr-deficient regions are marked with yellow arrows. (c) HAADF- and BF-STEM images of the SHO film showing misoriented grains (yellow arrows) and amorphous regions (green arrows).

5.5. Future work

Compared to BaHfO_3 , the electron affinity of SrHfO_3 is so small that it can create large conduction barrier when in contact with electrodes. As a result, by combining SrHfO_3 and BaTiO_3 , similar to the analogy with BHTO, we can generate more optimized dielectric properties. Instead of BaTiO_3 , SrTiO_3 could also be considered as a material with a high dielectric constant. However, when compared to BaTiO_3 , the dielectric constant of SrTiO_3 is relatively smaller. Therefore, BaTiO_3 is more suitable for the development of high-k materials. Exploring the $(\text{Sr}, \text{Ba})(\text{Hf}, \text{Ti})\text{O}_3$ system holds great potential for advancing high-k

material development.

5.6. Conclusion

In summary, we conducted research on the high-k SHO dielectric with an ultra-low leakage current density. Through the analysis of optical spectra and Fowler-Nordheim tunneling, we attribute the remarkably low leakage current density of SHO dielectric to the large optical band gap of SHO and the large conduction band offset between BSO and SHO. Additionally, we investigated the structural properties of SHO deposited in various oxygen pressures using high-resolution XRD measurements to understand the origin of the superior low leakage current. The optimized SHO dielectric has few defect states within the wide band gap, which is also responsible for the superior low leakage current density. Furthermore, we demonstrated the use of the n-type accumulation mode FET with SrHfO₃ gate oxide, which exhibits high mobility ($\mu_{FE} \sim 80 \text{ cm}^2 \text{ V}^{-1} \text{ s}^{-1}$) and low leakage current density ($10^{-7} \text{ A cm}^{-2}$ at 2 MV cm^{-1}). The excellent dielectric properties of SHO, particularly its low leakage current density, suggest that it has great potential for future electronics applications. Epitaxial SHO could play an important role, similar to SiO₂ in Si-based devices, in integrating other multi-functional perovskite oxides with Si.

References

- [1] N. S. Kim, T. Austin, D. Blaauw, T. Mudge, K. Flautner, J. S. Hu, M. J. Irwin, M. Kandemir, V. Narayanan, *Computer* **36**, 68-75 (2003).
- [2] K. Roy, S. Mukhopadhyay, H. Mahmoodi-Meimand, *Proc. IEEE*. **91**, 305-327 (2003).
- [3] A. P. Jacob, R. Xie, M. G. Sung, L. Liebmann, R. T. P. Lee, B. Taylor, *Int. J. High Speed Electron. Syst.* **26**, 1740001 (2017).
- [4] M. Palinje, S. K. Sinha, *2022 10th IEEE International Conference on Emerging Trends in Engineering and Technology - Signal and Information Processing (ICETET-SIP-22)*, 1-6 (2002).
- [5] G. D. Wilk, R. M. Wallace, J. M. Anthony, *J. Appl. Phys.* **89**, 5243 (2001).
- [6] S. Salahuddin, K. Ni, S. Datta, *Nat. Electron.* **1**, 442-450 (2018).
- [7] J. Robertson, R. M. Wallace, *Mater. Sci. Eng. R* **88**, 1-41 (2015).
- [8] F. C. Chiu, *Adv. Mater. Sci. Eng.* **2014**, 1-18 (2014).
- [9] J. Robertson, *Eur. Phys. J. Appl. Phys.* **28**, 265-291 (2004).
- [10] M. B. Shalom, M. Sachs, D. Rakhmilevitch, A. Palevski, Y. Dagan, *Phys. Rev. Lett.* **104**, 126802 (2010).
- [11] K. D. Fredrickson, P. Ponath, A. B. Posadas, M. R. McCartney, T. Aoki, D. J. Smith, A. A. Demkov, *Appl. Phys. Lett.* **104**, 242908 (2014).
- [12] U. Kim, C. Park, Y. M. Kim, J. Shin, K. Char, *APL Mater.* **4**, 071102 (2016).
- [13] Y. Kim, Y. M. Kim, J. Shin, K. Char, *APL Mater.* **6**, 096104 (2018).
- [14] Y. M. Kim, T. Markurt, Y. Kim, M. Zupancic, J. Shin, M. Albrecht, K. Char, *Sci. Rep.* **9**, 16202 (2019).
- [15] J. Shin, Y. M. Kim, C. Park, K. Char, *Phys. Rev. Appl.* **13**, 064066 (2020).
- [16] A. Ohtomo, H. Y. Hwang, *Nature* **427**, 423-426 (2004).
- [17] H. Cho, D. Song, Y. Kim, B. Kim, K. Char, *ACS Appl. Electron. Mater.* **4**, 356-366 (2022).
- [18] K. Abe, S. Komatsu, *Jpn. J. Appl. Phys.* **32**, 4186-4189 (1993).
- [19] S. Cho, C. Yun, Y. S. Kim, H. Wang, J. Jian, W. Zhang, J. Huang, X. Wang, H. Wang, J. L. MacManus-Driscoll, *Nano energy* **45**, 398-406 (2018).
- [20] C. S. Hwang, *J. Appl. Phys.* **92**, 432 (2002).
- [21] D. Wu, A. Li, Z. Liu, H. Ling, C. Z. Ge, X. Liu, H. Wang, M. Wang, P. Lü, N.

- Ming, *Thin Solid Films* **336**, 172-175 (1998).
- [22] T. Maekawa, K. Kurosaki, S. Yamanaka, *J. Alloys Compd.* **407**, 44-48 (2006).
- [23] G. Lupina, G. Kozłowski, J. Dabrowski, Ch. Wenger, P. Dudek, P. Zaumseil, G. Lippert, Ch. Walczyk, H.-J. Müssig, *Appl. Phys. Lett.* **92**, 062906 (2008).
- [24] Y. M. Kim, C. Park, T. Ha, U. Kim, N. Kim, J. Shin, Y. Kim, J. Yu, J. H. Kim, K. char, *APL Mater.* **5**, 016104 (2017).
- [25] M. Sawkar-Mathur, C. Marchiori, J. Fompeyrine, M. F. Toney, J. Bargar, J. P. Chang, *Thin Solid Films* **518**, S118-S122 (2010).
- [26] C. Rossel, B. Mereu, C. Marchiori, D. Caimi, M. Sousa, A. Guiller, H. Siegwart, R. Germann, J.-P. Locquet, J. Fompeyrine, D. J. Webb, Ch. Dieker, J. W. Seo, *Appl. Phys. Lett.* **89**, 053506 (2006).
- [27] C. Rossel, M. Sousa, C. Marchiori, J. Fompeyrine, D. Webb, D. Caimi, B. Mereu, A. Ispas, J. P. Locquet, H. Siegwart, R. Germann, A. Tapponnier, K. Babich, *Microelectron. Eng.* **84**, 1869-1873 (2007).
- [28] M. Sousa, C. Rossel, C. Marchiori, H. Siegwart, D. Caimi, J.-P. Locquet, D. J. Webb, R. Germann, J. Fompeyrine, *J. Appl. Phys.* **102**, 104103 (2007).
- [29] J. McPherson, J. Kim, A. Shanware, H. Mogul, J. Rodriguez, *IEEE Dig. Int. Electron Devices Meet.* 633–636 (2002).
- [30] A. Feteira, D. C. Sinclair, K. Z. Rajab, M. T. Lanagan, *J. Am. Ceram. Soc.* **91**, 893-901 (2008).
- [31] G. Lupina, G. Kozłowski, J. Dabrowski, P. Dudek, G. Lippert, H.-J. Müssig, *Appl. Phys. Lett.* **93**, 252907 (2008).
- [32] G. Lupina, O. Seifarth, P. Dudek, G. Kozłowski, J. Dabrowski, H.-J. Thieme, G. Lippert, T. Schroeder, H.-J. Müssig, *Phys. Status Solidi B* **248**, 323-326 (2011).
- [33] K. Black, M. Werner, R. Rowlands–Jones, P. R. Chalker, M. J. Rosseinsky, *Chem. Mater.* **23**, 2518-2520 (2011).
- [34] O. Fursenko, J. Bauer, G. Lupina, P. Dudek, M. Lukosius, Ch. Wenger, P. Zaumseil, *Thin Solid Films* **520**, 4532-4535 (2012).
- [35] B. J. Kennedy, C. J. Howard, B. C. Chakoumakos, *Phys. Rev. B* **60**, 2972-2975 (1999).
- [36] M. K. Singh, G. Singh, T. H. Kim, S. Kojima, R. S. Katiyar, J. F. Scott, *EPL* **107**, 26004 (2014).
- [37] M. D. McDaniel, C. Hu, S. Lu, T. Q. Ngo, A. Posadas, A. Jiang, D. J. Smith, E.

- T. Yu, A. A. Demkov, J. G. Ekerdt, *J. Appl. Phys.* **117**, 054101 (2015).
- [38] M. Karmaoui, E. V. Ramana, D. M. Tobaldi, L. Lajaunie, M. P. Graça, R. Arenal, M. P. Seabra, J. A. Labrincha, R. C. Pullar, *RSC Adv.* **6**, 51493 (2016).
- [39] L. M. Garten, S. Dwaraknath, J. Walker, J. S. Mangum, P. F. Ndione, Y. Park, D. A. Beaton, V. Gopalan, B. P. Gorman, L. T. Schelhas, M. F. Toney, S. Trolier-McKinstry, K. A. Persson, D. S. Ginley, *Adv. Mater.* **30**, 1800559 (2018).
- [40] M. Acharya, E. Banyas, M. Ramesh, Y. Jiang, A. Fernandez, A. Dasgupta, H. Ling, B. Hanrahan, K. Persson, J. B. Neaton, L. W. Martin, *Adv. Mater.* **34**, 2105967 (2022).
- [41] S. Ahmed, W. Zulfiqar, F. Javed, H. Arshad, G. Abbas, A. Laref, S. M. Alay-e-Abbas, *J. Alloys Compd.* **892**, 162071 (2021).
- [42] H. Murata, T. Yamamoto, H. Moriwake, I. Tanaka, *Phys. Status Solidi B* **246**, 1628-1633 (2009).
- [43] D. Song, M. Jeong, J. Kim, B. Kim, J. H. Kim, J. H. Kim, K. Lee, Y. Kim, K. Char, *Sci. Adv.* **8**, eabm3962 (2022).
- [44] U. Kim, C. Park, T. Ha, Y. M. Kim, N. Kim, C. Ju, J. Park, J. Yu, J. H. Kim, K. Char, *APL Mater.* **3**, 036101 (2015).
- [45] U. Kim, C. Park, T. Ha, R. Kim, H. S. Mun, H. M. Kim, H. J. Kim, T. H. Kim, N. Kim, J. Yu, K. H. Kim, J. H. Kim, K. Char, *APL Mater.* **2**, 056107 (2014).
- [46] L. Bjaalie, B. Himmetoglu, L. Weston, A. Janotti, C. G. Van de Walle, *New J. Phys.* **16**, 025005 (2014).
- [47] K.-I. Onisawa, M. Fuyama, K. Tamura, K. Taguchi, T. Nakayama, Y. A. Ono, *J. Appl. Phys.* **68**, 719 (1990).
- [48] D. Miron, I. Krylov, M. Baskin, E. Yalon, L. Kornblum, *J. Appl. Phys.* **126**, 185301 (2019).
- [49] H.-K. Ha, M. Yoshimoto, H. Koinuma, B.-K. Moon, H. Ishiwara, *Appl. Phys. Lett.* **68**, 2965 (1996).
- [50] S. Zaima, T. Furuta, Y. Koide, Y. Yasuda, M. Lida, *J. Electrochem. Soc.* **137**, 2876 (1990).
- [51] L. Kang, B. H. Lee, W.-J. Qi, Y. Jeon, R. Nieh, S. Gopalan, K. Onishi, J. C. Lee, *IEEE Electron Device Lett.* **21**, 181 (2000).
- [52] J. Liu, J. Li, J. Wu, J. Sun, *Nanoscale Res. Lett.* **14**, 154 (2019).
- [53] J. Chen, T. Kawanago, H. Wakabayashi, K. Tsutsui, H. Iwai, D. Nohata, H.

- Nohira, K. Kakushima, *Microelectron. Reliab.* **60**, 16-19 (2016).
- [54] G. Jiang, A. Liu, G. Liu, C. Zhu, Y. Meng, B. Shin, E. Fortunato, R. Martins, F. Shan, *Appl. Phys. Lett.* **109**, 183508 (2016).
- [55] V. Srikant, J. S. Speck, D. R. Clarke, *J. Appl. Phys.* **82**, 4286 (1997).
- [56] P. F. Miceli, C. J. Palmstrom, *Phys. Rev. B* **51**, 5506 (1995).
- [57] O. Durand, A. Letoublon, D. J. Rogers, F. Hosseini Teherani, *Thin Solid Films* **519**, 6369-6373 (2011).

List of publications

1. Hyeongmin Cho, **Dowon Song**, Youjung Kim, Bongju Kim, Kookrin Char, “High-mobility field-effect transistor using 2-dimensional Electron gas at the LaScO₃/BaSnO₃ interface”, *ACS Applied Electronic Materials* **4**, 356-366 (2022)
2. **Dowon Song**, Myoungho Jeong, Juhan Kim, Bongju Kim, Jae Ha Kim, Jae Hoon Kim, Kiyoun Lee, Yongsung Kim, Kookrin Char, “High-k perovskite gate oxide for modulation beyond 10¹⁴ cm⁻²”, *Science Advances* **8**, eabm3962 (2022)
3. Juhan Kim*, **Dowon Song***, Hwanhui Yun, Jaehyeok Lee, Jae Ha Kim, Jae Hoon Kim, Bongju Kim, Kookrin Char, “Low leakage in high-k perovskite gate oxide SrHfO₃”, *Advanced Electronic Materials* **2023**, 2201341 (2023) (*equally contributed)

List of presentations

1. Hahoon Lee, **Dowon Song**, Kookrin Char, “BaHf_{1-x}Ti_xO₃, high-k perovskite dielectric”, Workshop on Oxide Electronics 25, October 2018. (Poster)
2. Hahoon Lee, **Dowon Song**, Kookrin Char, “High-k perovskite dielectric BaHf_{1-x}Ti_xO₃”, American Physical society Meeting, March 2019. (Oral)
3. **Dowon Song**, Kookrin Char, “High-k perovskite dielectric BaHf_{1-x}Ti_xO₃”, The 3rd Workshop on Functional Materials Science, December 2019. (Poster)
4. **Dowon Song**, Myoungho Jeong, Juhan Kim, Bongju Kim, Jae Ha Kim, Jae Hoon Kim, Kiyoun Lee, Yongsung Kim, and Kookrin Char, “High-k perovskite gate oxide for modulation beyond 10¹⁴ cm⁻²”, Korea Dielectric Symposium 17, February 2022. (Poster)
5. **Dowon Song**, Myoungho Jeong, Juhan Kim, Bongju Kim, Jae Ha Kim, Jae Hoon Kim, Kiyoun Lee, Yongsung Kim, and Kookrin Char, “High-k perovskite gate oxide for modulation beyond 10¹⁴ cm⁻²”, Workshop on Oxide Electronics 28, October 2022. (Poster)

국문초록

BaHfO₃와 BaTiO₃ 혼합산화물의 유전특성에 대한 연구

송도원

서울대학교 물리천문학부

실리콘을 기반으로 한 소자 기술은 발열과 전력소모를 줄이기 위한 목적으로 지난 몇 십년 동안 지속적으로 감소되어 왔다. 발열과 전력소모를 줄이기 위해서는 동작전압을 감소시켜야 하는데, 이는 정전용량을 키움으로써 얻어질 수 있다. 그러나, 이에 따라 게이트 유전막의 두께가 점점 얇아지게 되었고, 직접 터널링을 통한 누설전류가 증가하게 되어 소자의 성능을 제한하게 되었다. 이 한계를 극복하기 위하여 연구자들은 더 두꺼운 유전체에서 요구되는 정전용량을 제공할 수 있는 high-k 물질에 대해서 연구해 왔다. 실리콘 기반의 소자에서 적합한 high-k 물질은 높은 유전상수를 가져야 함과 동시에 높은 전기장에서 높은 유전강도를 가져야 한다.

이 학위논문에서는 BaHfO₃와 BaTiO₃의 혼합산화물인 BaHf_{1-x}Ti_xO₃ (BHTO) 시스템의 high-k 유전체로써 유전특성에 대해서 연구하였다. Ba_{0.96}La_{0.04}SnO₃를 전극으로 사용하여 티타늄 비율(x)을 0.2에서 0.8까지 증가시키면서 유전상수와 절연파괴 전기장, 누설전류를 측정하였다. 유전상수는 티타늄 비율이 증가함에 따라 증가하였고, 티타늄 비율이 0.4를 넘지 않을 때 까지는 절연파괴 전기장은 5 MV/cm로 유지되고 누설전류는 절연파괴가 되기 전까지 $10^{-7} \sim 10^{-3}$ A/cm²로 유지되었다. 이 결과에 따르면 BaHf_{0.6}Ti_{0.4}O₃ 유전체는 2차원 전하밀도를 최대 $n_{2D} = 2 \times 10^{14}$ cm⁻²까지 제어할 수 있다. BaHf_{0.6}Ti_{0.4}O₃ 유전체를 이용하여 모든 층이 투명한 perovskite로 이루어진 n-type 축적모드 전계효과 트랜지스터를 제작하

었다. 이 소자의 on/off 전류 비율이 10^7 보다 크고 최대 이동도를 가지는 지점에서 게이트-소스 전압이 6 V보다 작고 문턱 전압 이하 스윙은 0.2로 측정되었다.

BaHf_{0.6}Ti_{0.4}O₃(BHTO)의 경우, 바뀐 공정조건에서 향상된 유전특성이 측정되었다. 유전상수와 절연파괴 전기장, 누설전류는 각각 150, 5.0 MV/cm, 2 MV/cm에서 10^{-4} A/cm²로 측정되었다. 이 수치로부터 BHTO 유전체가 최대 제어할 수 있는 2차원 전하밀도는 10^{14} cm⁻² 이상으로 계산되고, 보통의 유전체들은 유전상수가 큰 경우 항복전기장이 반비례하여 작으므로 이 값을 얻기 쉽지 않다. 이 유전체를 유전막으로 사용하여 실제로 n-type 축적 모드 (accumulation mode) FET와 공핍 모드 (depletion mode) FET를 구현하는데 성공하여 실제로 10^{14} cm⁻²의 전하밀도를 제어함을 확인하였다. BHTO가 유전상수가 높으면서 동시에 높은 항복전기장을 가지고 낮은 누설전류를 가질 수 있는 원인은 나노미터 단위 스케일의 티타늄의 군집화 현상이고, 이 모델에 따르면 이 구조를 가지게 되면 하프늄 기반의 배경이 유전체의 누설 전류 및 항복에 영향을 주는 percolation 통로 형성을 억제하는 효과가 있다.

그러나, BHTO의 유전상수는 두께가 감소함에 따라 감소하게 되는데, 이는 high-k 유전체에서 발생한다고 잘 알려진 “사이즈 효과”이다. 이는 원하지 않게 형성되는 계면의 낮은 정전용량으로 인하여 나타나는 문제이다. 비록 사이즈 효과의 원인에 대해서는 여전히 논란이 많으나, 강한 에피택시 결합이 중요한 요인으로 생각된다. High-k 물질과 전극 사이의 계면의 강한 결합은 유전체의 유전상수와 관계있는 소프트 포논이 전극쪽으로 전파되게 만들고, 계면 근처에서의 소프트 포논과 유전상수를 떨어뜨린다. 그러한 전파를 막기 위한 경계를 형성하기 위해서 의도적으로 격자상수가 맞지 않도록 하였고, 계면의 에피택시 결합을 약하게 하기 위하여 SrRuO₃를 하부전극으로, ITO를 상부전극으로 사용하였다. 이를 통하여 계면의 정전용량이 3~5배 정도로 증가하는 효과를 검증하였다.

High-k 물질을 더 개발하기 위하여, SrHfO₃ (SHO)를 연구하였다.

SHO의 누설전류는 2 MV/cm에서 10^{-8} A/cm² 이하로 매우 작다. SHO의 누설전류가 작은 이유는 약 6 eV 정도의 큰 밴드갭과 4% BLSO와 SHO 사이의 약 3.3 eV 정도의 큰 전도띠 차이 때문이다. 이러한 큰 전도띠 차이는 Si와 SiO₂ 사이의 전도띠 차이에 필적하는 값이다. 따라서, SHO의 전자친화도는 약 1.2 eV로 충분히 낮아서 대부분의 전극과 1 eV 이상의 전도띠 차이를 만들 수 있다. 그럼에도 불구하고, SHO의 유전상수는 약 30정도로 상대적으로 보통인 값이다. 그러므로, BHTO의 경우와 유사한 접근방법으로 SHO와 SrTiO₃, BaTiO₃ 등의 high-k 물질과 결합한다면 더 우수한 유전체를 개발할 수 있는 가능성이 있다.

Keywords: BaHfO₃, BaTiO₃, 페로브스카이트 산화물, High-k, 화학양론적 변조, 사이즈 효과, 계면 포논 공학, SrHfO₃.

Student Number: 2017-23010

감사의 글

지난 6년 동안 학위과정을 진행하면서 정말 많은 분들께 도움을 받았고 신세를 졌습니다. 덕분에 이 학위논문이 나올 수 있었고, 박사 학위를 취득할 수 있게 되었습니다. 대학원 입학 당시와 비교하면, 많은 성장을 이루었다고 생각합니다. 이는 많은 분들의 도움 덕분입니다. 제일 먼저 존경하는 저의 지도교수님, 차국린 교수님께 무한한 감사의 말씀을 드립니다. 연구적인 부분으로도 많이 배웠지만, 교수님께서 저의 제2의 아버지라고 불려도 될 정도로 인생에 대해서도 정말 많은 가르침을 주셨습니다. 교수님으로부터 배운 것들과 깨달은 것들은 앞으로 험한 세상을 향해할 저에게 중요한 나침반이 될 것입니다. 또한 바쁘신 와중에 박사학위 심사를 맡아 주신 홍승훈 교수님, 유재준 교수님, 김기훈 교수님, 이기영 교수님께도 감사의 말씀을 전합니다. 길지는 않은 시간이었으나 교수님들께서 심사과정에서 해주신 말씀들은 다시 한번 저를 되돌아볼 수 있는 계기를 마련해주었고, 제가 스스로 발전할 수 있는 초석을 마련해주었습니다. 그리고 저의 논문이 출간될 수 있도록 많은 도움을 주신 김봉주 박사님께 감사의 말씀을 올립니다.

제가 연구실 생활을 잘할 수 있도록 도움을 주신 선배님들께도 감사의 인사를 전합니다. 영모형, 유정누나, 예주누나, 그리고 제가 연구실 들어와서 처음 실험을 잘할 수 있도록 가르쳐 주신 하훈이형에게 특별한 감사의 말씀을 드립니다. 또한 저의 학부 동기이자 10년이 가까운 시간동안 항상 힘들 때 도움을 주고 조언을 해주었던 형민이형에게 진심으로 감사합니다. 함께 쉽지 않은 연구생활을 버텨낼 수 있는 원동력을 제공해준 후배들에게도 감사를 표합니다. 특히, 서로 좋은 영향을 주며 함께 성장할 수 있는 계기를 마련해준 주한이형에게 감사의 말을 올립니다. 그리고 함께 서울대학교 대학원에 진학하여 힘들 때는 도와주고 축하할 일이 있을때는 함께 기뻐해준 우리 연세대학교 물리학과 13학번 동기들인 성욱, 채빈, 지훈이형에게 고맙

다는 말을 전하고 싶습니다. 대학원 생활에 지칠 때 활기가 되어준 단무지 친구들, 특히 태중이, 도홍이, 상호, 황준이형 모두에게 고맙습니다. 그리고 나의 소중한 고향 친구들, 세웅이, 상환이, 제호, 건지, 윤섭이 모두 고맙습니다. 운동에 대해서는 무지하던 저에게 운동을 가르쳐 준 건희에게 고맙습니다. 그리고 각자 다른 길에서 잘 해내고 있는 우리 해강반 친구들, 찬영이, 세웅이, 승현이, 희상이, 도영이, 지수, 예철이에게 고맙습니다. 그리고 저의 사부님과 다름없는 형님들, 섬균이형, 정우형에게 고맙습니다. 또한 대학교 재학시절부터 대학원까지 재정적으로 큰 도움을 주신 병석 외삼촌께 정말 감사드립니다.

마지막으로 항상 아들을 믿어 주시고 아들이 최고라고 응원해주시고 자랑스럽게 여겨 주신 부모님께 감사의 말씀을 올립니다. 또한 대학원 생활동안 같이 살며 외롭지 않도록 동무가 되어준 동생 도문이에게 감사함을 전합니다. 소중한 나의 가족들이 더 자랑스러운 아들이자 형이 되도록 앞으로 더 노력하겠습니다.